

EDITORIAL BOARD

Editor-in-Chief

B.E. Paton

Scientists of PWI, Kiev

S.I. Kuchuk-Yatsenko (*vice-chief ed.*),

V.N. Lipodaev (*vice-chief ed.*),

Yu.S. Borisov, G.M. Grigorenko,

A.T. Zelnichenko, V.V. Knysh,

I.V. Krivtsun, Yu.N. Lankin,

L.M. Lobanov, V.D. Poznyakov,

I.A. Ryabtsev, K.A. Yushchenko

Scientists of Ukrainian Universities

V.V. Dmitrik, NTU «KhPI», Kharkov

V.V. Kvasnitsky, NTUU «KPI», Kiev

V.D. Kuznetsov, NTUU «KPI», Kiev

Foreign Scientists

N.P. Alyoshin

N.E. Bauman MSTU, Moscow, Russia

Guan Qiao

Beijing Aeronautical Institute, China

A.S. Zubchenko

DB «Gidropress», Podolsk, Russia

M. Zinigrad

Ariel University, Israel

V.I. Lysak

Volgograd STU, Russia

Ya. Pilarczyk

Welding Institute, Gliwice, Poland

U. Reisgen

Welding and Joining Institute, Aachen, Germany

G.A. Turichin

St. Petersburg SPU, Russia

Founders

E.O. Paton Electric Welding Institute, NASU

International Association «Welding»

Publisher

International Association «Welding»

Translators

A.A. Fomin, O.S. Kurochko, I.N. Kutianova

Editor

N.A. Dmitrieva

Electron galley

D.I. Sereda, T.Yu. Snegiryova

Address

E.O. Paton Electric Welding Institute,

International Association «Welding»

11 Kazimir Malevich Str. (former Bozhenko Str.),

03680, Kiev, Ukraine

Tel.: (38044) 200 60 16, 200 82 77

Fax: (38044) 200 82 77, 200 81 45

E-mail: journal@paton.kiev.ua

www.patonpublishinghouse.com

State Registration Certificate

KV 4790 of 09.01.2001

ISSN 0957-798X

Subscriptions

\$348, 12 issues per year,

air postage and packaging included.

Back issues available.

All rights reserved.

This publication and each of the articles contained

herein are protected by copyright.

Permission to reproduce material contained in this journal must be obtained in writing from the Publisher.

CONTENTS

SCIENTIFIC AND TECHNICAL

- Ivanov V.P. and Lavrova E.V.* Controlling penetration zone formation in arc surfacing 2
- Matvienko V.N., Leshchinsky L.K. and Mazur V.A.* Effect of composition of electrode strip on base metal penetration 7
- Shchetinin S.V.* Improvement of crack resistance of banded supporting rolls at high-speed surfacing with low heat input 10
- Yushchenko K.A., Zadery B.A., Gakh I.S. and Karasevskaya O.P.* Formation of weld metal structure in electron beam welding of single crystals of high-temperature nickel alloys 15
- Elagin V.P., Lipodaev V.N. and Gordan G.N.* Peculiarities of development of structural heterogeneity in the fusion zone of pearlite steel with austenitic nitrogen-containing weld metal 23
- Bo Li, Zhihong Li, Lijing Yang and Jianhua Yao.* Microstructure and wear-resistant properties of WC/SS316L composite coatings prepared by supersonic laser deposition 29

INDUSTRIAL

- Shapovalov K.P., Belinsky V.A., Merzlyakov A.E., Kosinov S.N., Yushchenko K.A., Lychko I.I. and Kozulin S.M.* Electroslag welding of large-sized press frame 36
- Makhlin N.M.* Improvement of welding power sources in order to increase burning stability of alternating current arc 40
- Prokofiev A.S., Gubatyuk R.S., Muzhichenko A.F. and Baranovsky V.N.* Calculation of two-layer billet of spherical bottoms for high-pressure vessels 49

CONTROLLING PENETRATION ZONE FORMATION IN ARC SURFACING

V.P. IVANOV and E.V. LAVROVA

Priazovsky State Technical University

7 Universitetskaya Str., 87500, Mariupol, Ukraine. E-mail: pstu.edu.oitzv@gmail.com

Influence of surfacing mode parameters on penetration zone formation was studied, and methods of controlling and stabilizing the process of weld pool formation were determined. Models of penetration zone formation for stationary and moving electrodes were developed. Calculated dependencies were determined by statistical processing of the results of measuring penetration zone parameters in macrosections of samples produced by submerged-arc surfacing for different electrode diameters and applied feed rates (current), depending on arcing time and arc movement speed. Obtained mathematical models of penetration zone formation in submerged-arc surfacing were used to develop software and control system of surfacing equipment. 8 Ref., 1 Table, 9 Figures.

Keywords: *weld pool, penetration zone, mathematical model, control of weld pool formation process*

Modern production requires development of adequate models of processes occurring in the weld pool, and CAD-CAE-CAM tools.

Controlling weld pool formation allows ensuring the quality of (pad) weld at changing of technological process parameters. At present, technologies of welding and surfacing both with wire [1, 2], and strip electrodes [3, 4] have been developed, in which higher effectiveness is achieved not by stabilization of mode parameters, but by their variation by certain functional dependencies.

At deposition of reconditioning and protective layers attention is focused on deposited layer formation, while the main function of penetration zone is reliable adhesion of the layers for preservation of overall performance of surfaced part or tool. Increase of penetration zone leads not only to increase of surfacing cost, but also to lowering of deposited payer performance, because of its heating and increase of the proportion of base metal in the deposited metal.

Dimensions of surfacing and penetration zones are directly proportional to electrode feed rate at specified type and material of the electrode, as well as to its melting conditions [5, 6]. Control of these zones formation requires clear understanding of the mechanism and sequence of their formation and their mutual influence. Running of these processes in the liquid phase necessitates determination of time and rate characteristics of melting front propagation as the base for construction of mathematical models of weld formation.

The aim of the work is studying the process of penetration zone formation in submerged-arc surfacing, determination of effective methods of controlling this zone parameters, as well as development of tech-

nology, equipment and control systems for realization of such technology.

In keeping with the defined task, dynamics of penetration zone formation in surfacing low-carbon steel plates (350×240×30 mm) with stationary electrode using AN-60 and AN-348A fluxes on stainless steel substrate was studied. Surfacing was conducted with wire electrode Sv-08A (used wire diameters and surfacing mode parameters are given in the Table). Arcing time was recorded using a timer (from 5 to 10 samples in each studied interval). After surfacing the samples were cut with abrasive wheel so that the cut line passed along the axis of symmetry of the deposited spot. Macrosections were treated by 20 % solution of nitric acid to reveal the penetration zone. Figure 1 shows samples of transverse macrosections of welds in surfacing with 4 mm electrode. Statistical processing of the results of measuring penetration zone parameters was followed by plotting approximation polynomial dependencies of its development in surfacing with electrodes of different diameters and arcing time (Figure 2).

Processing of experimental data was performed by the method of multiple regression analysis with screening variables at significance level $\alpha = 0.03$ at the value of correlation coefficient $R = 0.96-0.97$. Resulting mean deviation values were used to select third-degree polynomials, which showed quite good agreement with research results. Differentiation of the data of functional dependencies in time yielded models of the change of penetration zone growth rate up to its solidification within the used array of initial data. Investigation of models of penetration zone growth rate in each studied time interval showed that they can be generalized by a function of the following form:

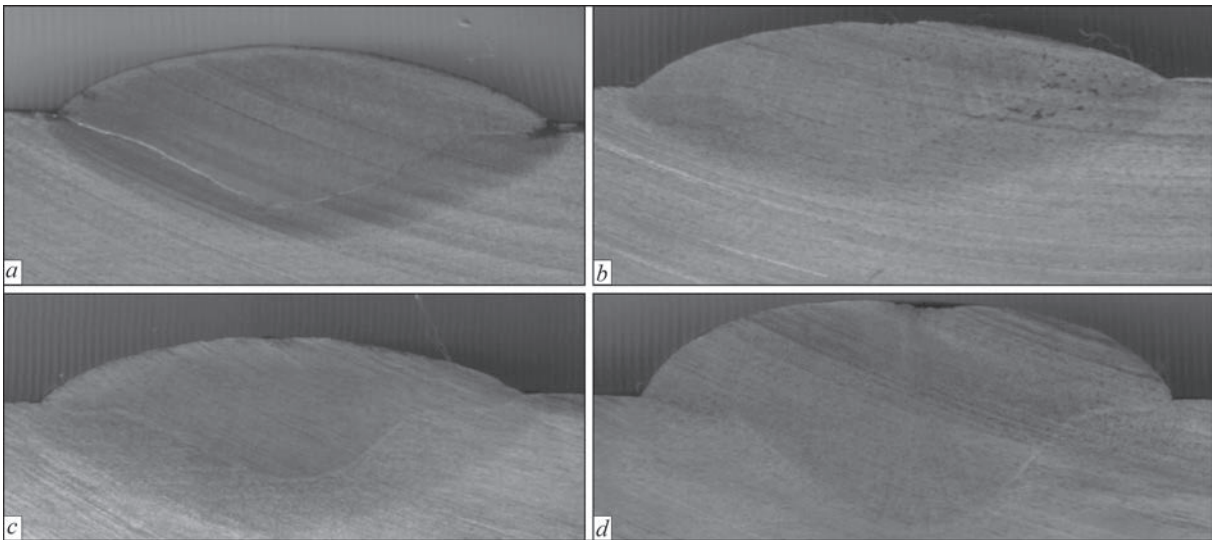


Figure 1. Cross-sections of surfaced samples at arcing time of: *a* — 2; *b* — 5; *c* — 7; *d* — 10 s for $d_{el} = 4$ mm, $I_s = 600\text{--}650$ A, $v_f = 33 \cdot 10^{-3}$ m/s, $U_a = 30\text{--}32$ V

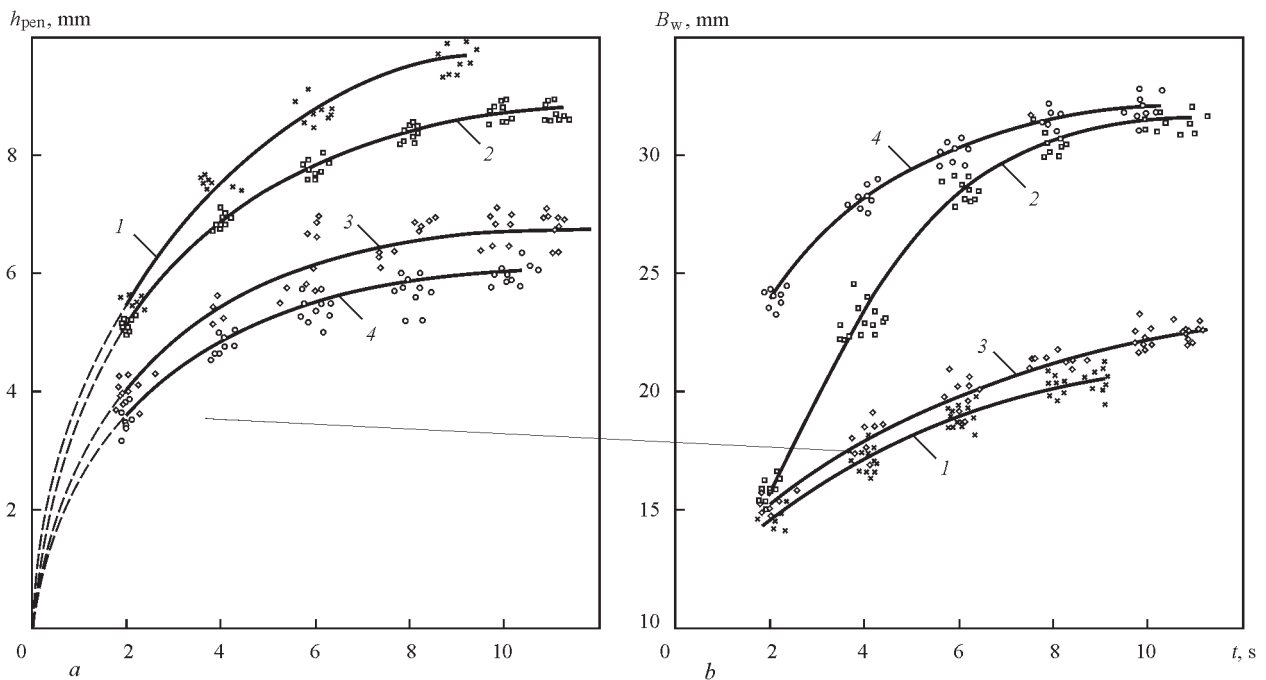


Figure 2. Dependence of penetration zone depth (*a*) and weld width (*c*) on arcing time *t*: 1 — $d_{el} = 3$ mm, $I_s = 550$ A, $U_a = 30$ V; 2 — $d_{el} = 4$ mm, $I_s = 650$ A, $U_a = 32$ V; 3 — $d_{el} = 4$ mm, $I_s = 550$ A, $U_a = 30$ V; 4 — $d_{el} = 5$ mm, $I_s = 550$ A, $U_a = 30$ V

$$\bar{V}_i(\bar{x}) = \left[\varepsilon_1 \bar{x}^2 + \varepsilon_2 \exp(\bar{x}) + \frac{\varepsilon_3}{\exp(\bar{x})} + \varepsilon_4 \bar{x} + \varepsilon_5 \right]^{-1}$$

where $\bar{V}_i(\bar{x})$ is the relative rate of penetration zone growth for *i*-th interval; \bar{x} is the relative coordinate of melting front point; ε_i are the coefficients, which are the functional dependencies on technological parameters, where electrode feed rate and its diameter are the main independent variables.

Figure 3 shows the graphs of dependencies of relative rate of melting front propagation (according to the above dependence) in its formation cycle, divided into 10 equal time intervals t_i , where *i* is the fraction of

formation cycle. Figure 4 gives a comparison of calculated contours of penetration zone with the data of macrosection measurements for fixed values of their formation time. Analysis of obtained dependencies

Ranges of surfacing mode parameters variation

d_{el} , mm	Parameters			
	I_s , A	$v_f \cdot 10^{-3}$, m/s	l_{el} , mm	U_a , V
1.6	180–300	22–50	20	26–30
2.0	210–390	22–46	25	26–30
3.0	280–550	14–40	30	28–32
3.5	300–600	15–36	30	30–34
4.0	400–700	15–32	40	30–34
5.0	500–800	15–28	45	30–36

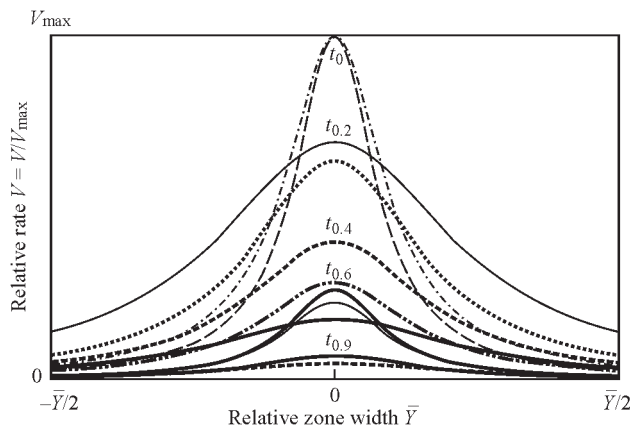


Figure 3. Dependencies of variation of relative rate of base metal melting front propagation

shows that after passing of 60–80 % of zone growth time, the profile of the rates across pool cross-section is levelled, and the limits of the penetration zone become larger uniformly in all the directions, while the absolute value of the rate drops to zero. This is also confirmed by decrease of the value of discrepancy between the calculated and experimental data in this time interval (see Figure 4). Comparison of penetration zone profiles shows quite good agreement of calculated and experimental data, except for fusion boundary, that is associated with the model not allowing for force factors prevalent in this zone [7].

Extension of calculation results for stationary electrode to cases, when its movement speed is not equal to zero, involves application of functional dependence, relating the time of action of a stationary source in point O with its movement speed. In the case of electrode movement, penetration maximum is at a certain distance from electrode axis, so that maximum penetration depth does not coincide with maximum reinforcement, the sum of which exactly makes up weld height h after its solidification. This is rarely taken into account in calculation schemes, as weld pool front wall is represented as part of circumference with a center on electrode tip not only for a stationary, but also for a moving source. Thus, the value of welding speed is the parameter, determining the degree of weld pool asymmetry, which can be the main input parameter when solving problems of analysis based on non-deterministic models.

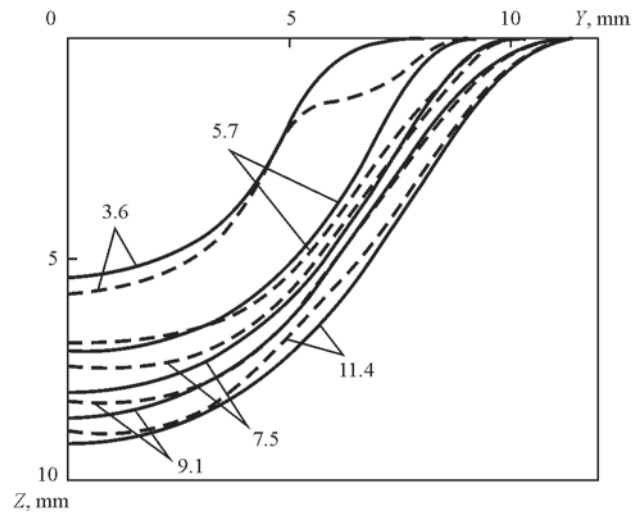


Figure 4. Calculated (solid curve) and experimental (dashed) contours of weld pool for $d_{el} = 4$ mm, $I_s = 650\text{--}700$ A, $v_f = 42 \cdot 10^{-3}$ m/s, $U_a = 30\text{--}32$ V

Used as calculation scheme for stationary electrode (Figure 5) was the scheme with movement of quasistationary penetration zone of radius R_0 , moving at speed v_w and recorded at moments of time t_i (with step Δ) [8].

Current position is determined by point O' , in which a stationary penetration zone of radius r_i forms. Step Δ_i determines time t' , which is required for melting front to reach an area limited by radius R_0 . It is assumed that after time step t' is over, solidification of weld pool of this contour, limited by isotherm T_{melt} , begins, and the source moves by step Δ . Condition $\Delta' = \Delta$ was used as process optimization condition, i.e. in this case, condition of maximum penetration zone at a given heat source power is fulfilled. In this case, minimum consumption of energy at specified weld parameters is ensured, i.e. to reduce penetration depth and proportion of base metal, optimization condition looks as $\Delta' = \beta\Delta$, where β is the coefficient, dependent on technological conditions [8].

Generalization of investigation results for the case of moving electrode leads to the conclusion that effective control of penetration zone formation in arc surfacing can be achieved by variation of two parameters: electrode feed rate and arc movement speed. So, Figure 6 gives the dependence of penetration zone depth on feed rate v_0 in automatic arc surfacing with wire electrode ($v_w = 15$ m/h). Macrosections for current

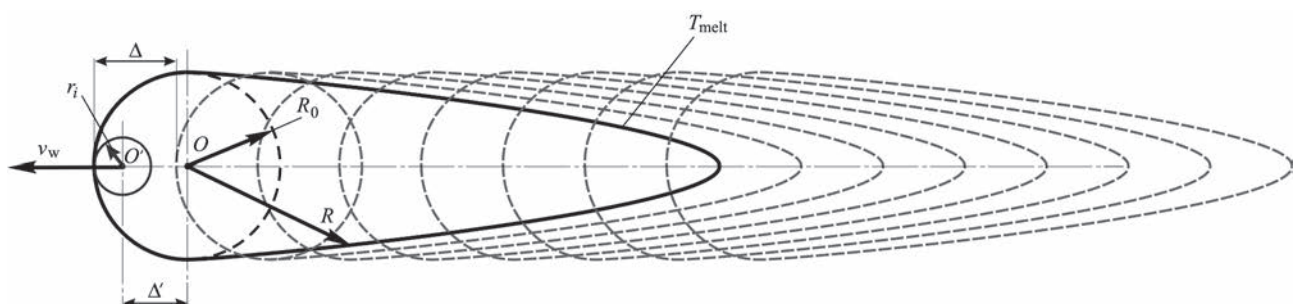


Figure 5. Calculation scheme for determination of weld pool dimensions in the case of electrode movement with welding speed

values of 550 (1), 680 (2) and 750 (3) A are given for comparison (penetration zone is marked by a dashed line). The given data lead to the conclusion that the width of penetration zone is practically independent on v_0 , and its certain reduction is, probably, related to a change of the size of effective heating zone at increase of feed rate (current) due to constriction of arc column and it penetrating deeper into base metal.

Developed models allow quantitative determination of the influence of variation of electrode feed rate by a certain law on penetration zone formation. In this case, the function of electrode speed variation is used as the argument of a system of equations for calculation of the rate of melting front propagation. This procedure was the base for creation of CAE-module for designing the surfacing technology (Figure 7), providing optimization of mode parameters, allowing for technology variant and applied welding consumables. The module includes a block for calculation of parameters of a deposited layer of a variable chemical composition in melting of two electrodes of different chemical composition in a common pool. Here, electrode feed rates are calculated, proceeding from the assigned law of variation of alloying element concen-

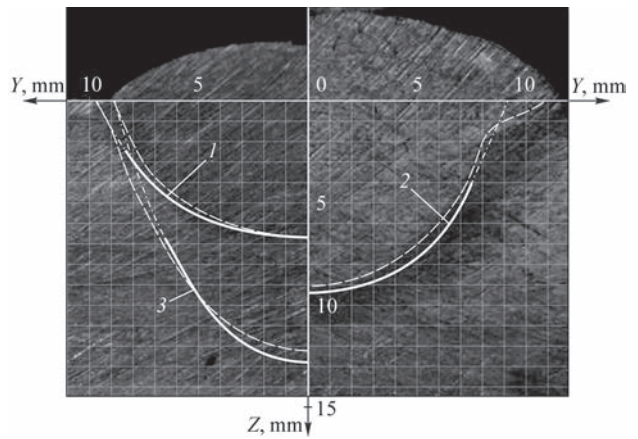


Figure 6. Dependence of penetration shape on feed rate of 4 mm wire electrode with $v \cdot 10^{-3} = 25$ (1), 33 (2) and 44 (3) mm/s

tration in the transition section in the case of the pool quasistationary state.

A control system for the surfacing process (Figure 8) was developed, which uses calculated values of parameters of electrode feed rate and movement speed to generate control signals to the drives of surfacing unit equipment (Figure 9). Control system is a software-implemented phase position control circuit of the thyristors. «More–Less buttons» allow controlling

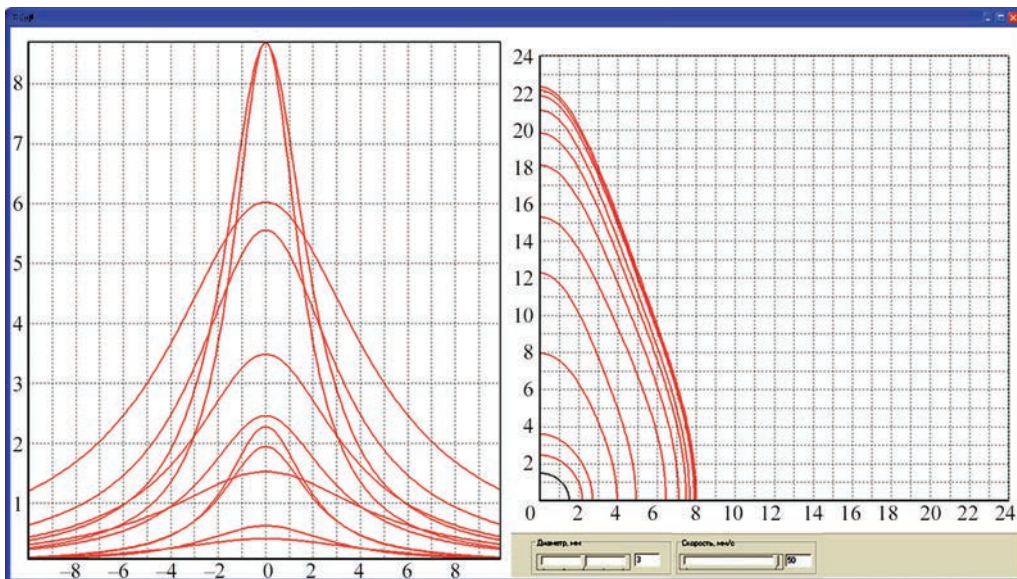


Figure 7. Module of penetration zone parameter calculation

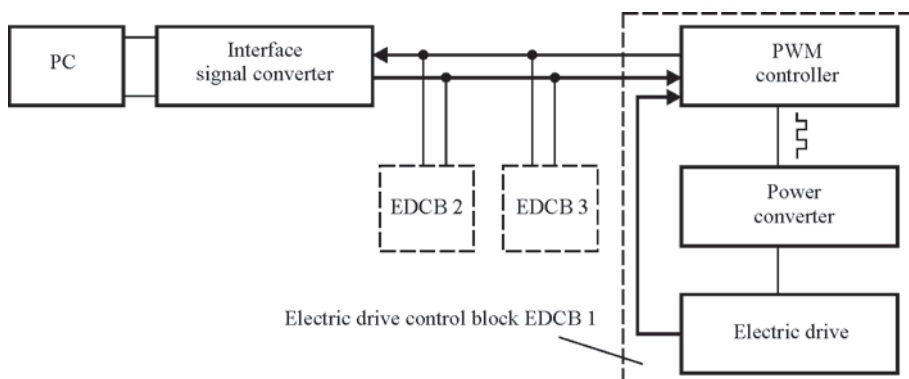


Figure 8. Block-diagram of surfacing process control system

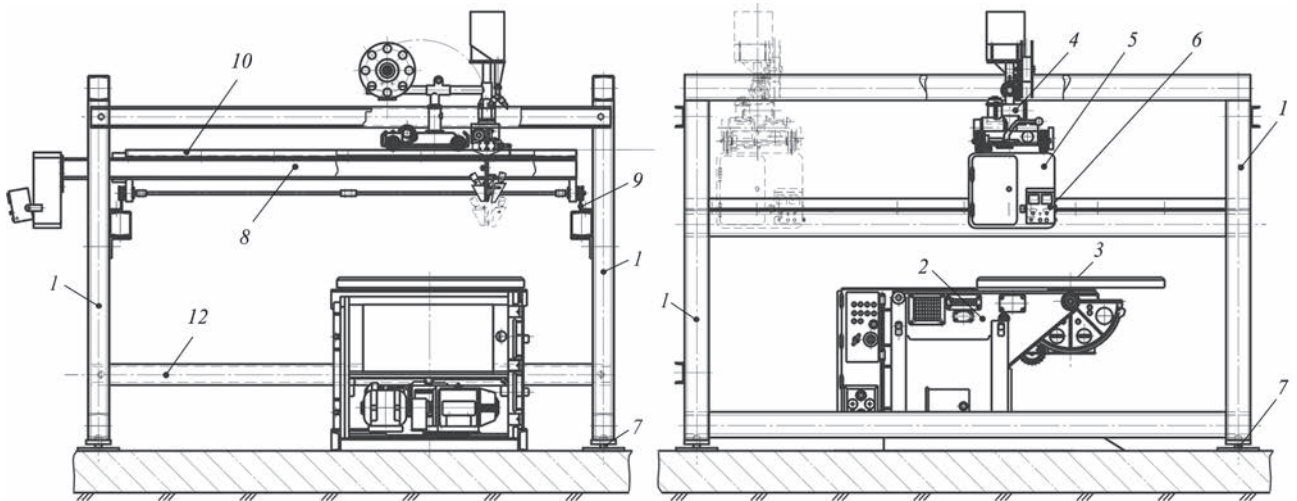


Figure 9. Schematic of surfacing unit (for designations see the text)

the moment of thyristor switching on. Control system status is saved in non-volatile processor memory, and at subsequent switching-on of the unit the last recorded status is read from the memory. Motors of feeding and movement of electrode and item are PWM-controlled, with time delay of motor switching-on being also implemented through software, and braking at switching off being performed through a relay.

Surfacing stand is of modular design (see Figure 9). Stand framework consists of four columns *1* on adjustable supports *7* and six longitudinal beams *12*. Middle beams have a detachable connection with columns (bolted joints), and can be positioned with a certain step by height relative to surfaced item. These beams carry guides *9* for displacement of frame *8* with welding tractor *4* along the stand. Frame beams go beyond the stand framework dimensions, as they carry equipment for surfacing process control: cabinet *5* and removable control panel *6*, which is connected to the cabinet and manipulator *2* and to faceplate *3* by flexible cables.

All the design elements of the framework, as well as frame beams, have the same cross-section of box-like structure, welded from two bent channel bars. Framework stability is provided by lateral braces made from channel bars.

As the lateral braces are removable, and moving frame guides are extendable, framework dimensions can be easily adjusted to suit the dimensions of the surfaced items. Transverse movement is performed by welding tractor drive. For this purpose guides *10* are mounted on frame *8*.

Conclusions

1. Influence of surfacing mode parameters on development of penetration zone in submerged-arc surfacing was studied for a stationary and moving arc. It is

found that dependencies of the change of melting rates can be expressed by a generalized model (formula) for the entire interval of zone growth. For the case of an electrode, moving at welding speed, calculation by the developed model is performed with the condition of movement of a stationary penetration zone, recorded at moments t_i with step Δ by movement coordinate.

2. Investigation results were used to develop mathematical models of penetration zone dynamics. Electrode feed rate and movement speed were taken as initial parameters. Software, equipment and control system were developed, which allow controlling deposited layer formation at the change of surfacing process parameters.

1. Paton, B.E., Lebedev, V.A. (2002) Analysis of technical and technological possibilities of electrode wire pulsed feed in arc welding and surfacing processes. *Svarochn. Proizvodstvo*, **2**, 24–31.
2. Shaferovsky, V.A., Serenko, A.N. (2007) Method of submerged-arc welding of plate metal with programming of mode parameters. In: *Proc. of 2nd Sci.-Techn. Seminar on Welding and Related Processes in Industry* (17 April 2007, Kiev, Ukraine), 8–11.
3. Ivanov, V.P., Lavrova, E.V. (2014) Improving the efficiency of strip cladding by the control of electrode metal transfer. *Appl. Mechanics and Materials*, **682**, 266–269.
4. Ivanov, V.P., Lavrova, E.V., Stepnova, Yu.A. (2015) Study of process of controlled mechanical transfer in surfacing with two strip electrode. *Visnyk DonbasDMBA*, **3**, 102–107.
5. Kiyohara, M., Yamamoto, H.Y., Harada, S. (1979) Melting characteristics of a wire electrode in the MIG-welding of aluminium. In: *Arc physics and weld pool behavior*, Paper 26, 165–175.
6. Killing, R. (1991) Guenstige Strom-spannungsreihe beim MIG-MAG-impulslichtbogenschweissen von Stahl und Aluminium unter verschiedenen Schutz Gasen. *DVS Bericht*, **131**, 15–21.
7. Lu, S., Hidetoshi, F., Sugiyama, H. et al. (2003) Marangoni convection and welding penetration in A-TIG welding. *Transact. of JWRI*, **32**(2), 79–82.
8. Ivanov, V.P. (2013) Increase in efficiency of arc surfacing process by control of welding pool hydrodynamics. *Visnyk PryazovDTU*, **26**, 150–160.

Received 10.06.2016

EFFECT OF COMPOSITION OF ELECTRODE STRIP ON BASE METAL PENETRATION

V.N. MATVIENKO, L.K. LESHCHINSKY and V.A. MAZUR

Priazovsky State Technical University

7 Universitetskaya Str., 87500, Mariupol, Ukraine. E-mail: matviyenkovn@mail.ru

The paper gives the results of investigation of effect of composition and thermophysical properties of weld pool molten metal on penetration efficiency in submerged arc surfacing using strip electrode. The results of processing and analysis of received experimental and calculation data show that under conditions of formation of composition of weld pool close to strip electrode composition, reduction of penetration area is correlated with reduction of melt enthalpy at replacement of Sv-08kp strip by Sv-12Kh18N10. 8 Ref., 1 Table, 4 Figures.

Keywords: metal melting, weld pool, thermophysical properties, enthalpy, melting temperature, surfacing, strip electrode, penetration area

Solving the problem of increase of efficiency and improvement of technical-economical characteristics of arc welding and surfacing, as one of the directions, provides for study of the process of metal heating and formation of weld pool taking into account thermophysical properties of welding consumables.

In strip electrode surfacing the composition and properties of weld pool molten metal are determined by considerably larger portion of electrode metal and significantly lower portion of base one [1, 2]. At the same time, if section of strip electrode is preserved invariable and current density is linear (relatively to strip width), the portion of electrode metal in the pool melt is determined by the level of heat source dis-

tribution and, as follows from the experimental data (Figure 1), depends on strip geometry.

It agrees with the investigations of macrosections of cross-section of deposited beads (Figure 2) as well as calculated shape and size of penetration zone at strip width from 30 to 60 mm (Figure 3). The calculation data were acquired using mathematical model of the process of base metal heating, based on solving a non-linear differential equation of heat conductance

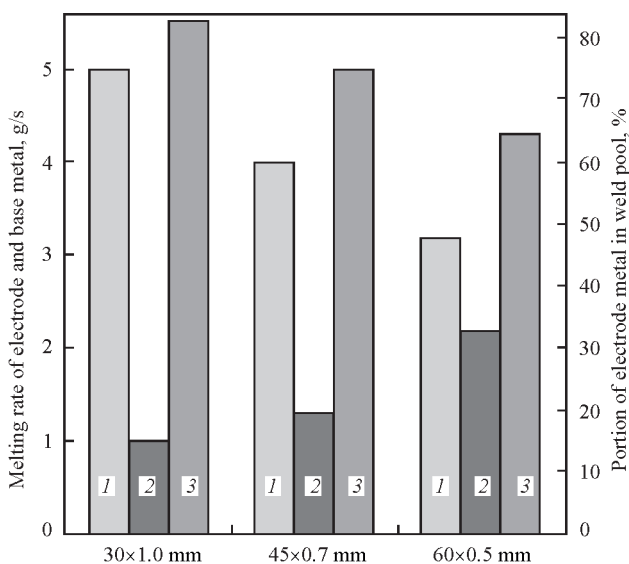


Figure 1. Weight melting rate of electrode (1) and base (2) metal, and portion of electrode metal in composition of weld pool (3) in strip electrode surfacing of different sections

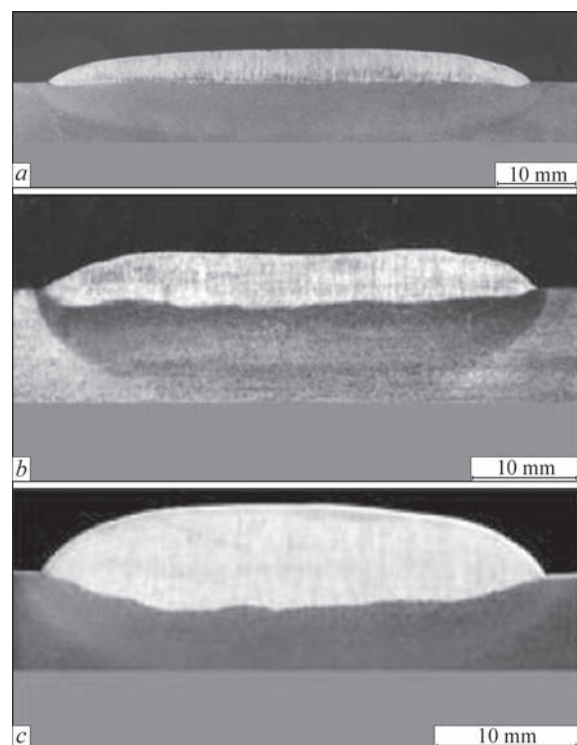


Figure 2. Macrostructure of cross-section of beads in surfacing with strip electrodes of 60×0.5 (a), 45×0.7 (b) and 30×1.0 (c) mm section from 12Kh18N10 steel

Effect of composition and thermophysical properties of weld pool melt on relative value of penetration area

Strip surfacing	$T_{melt}, ^\circ C$	$T_{melt}^i / T_{melt}^{st}$	$\Delta H, J/g$	$\Delta H / \Delta H^{st}$	$\Delta H, J/g$	$\Delta H / \Delta H^{st}$	Change of penetration area
			Calculation data		Experimental		
Sv-08kp	1530	1	1130	1	1450	1	1
Sv-12Kh18N10	1420	0.93	930	0.82	1200	0.82	0.80/0.82
70Cu-30Ni	1240	0.81	710	0.62	—	—	-/0.60

Note. $T_{melt}^i / T_{melt}^{st}$, $\Delta H / \Delta H^{st}$ — relation of melting temperature and enthalpy of melt of this material to penetration temperature and enthalpy of steel 08kp. Before the slash — determination of penetration area on macrosections (see Figure 4), after — results of processing of data of work [7].

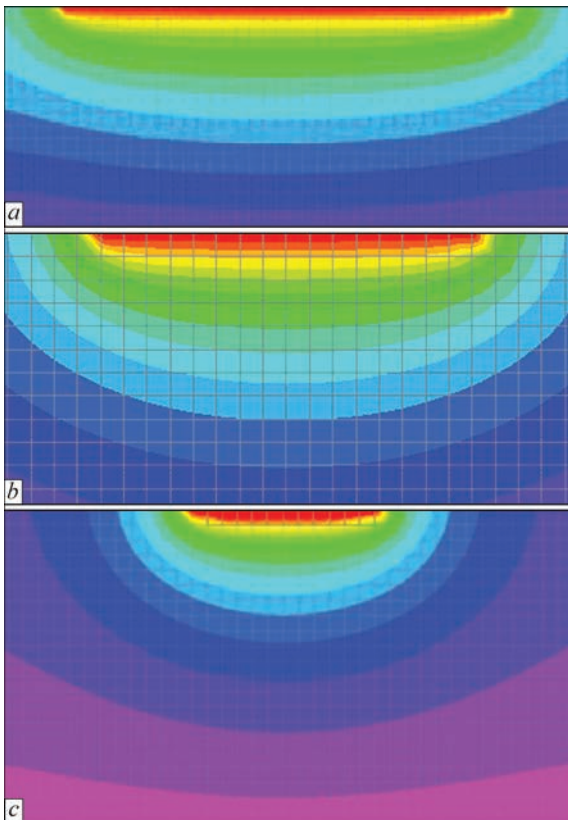


Figure 3. Models of thermal field in plane normal to deposited surface for strip electrodes same as in a-c — the Figure 2

taking into account temperature dependence of thermophysical properties of the material [3].

Portion of electrode metal in the pool achieves 83–85 % (see Figure 1) in surfacing of St.3 steel with Sv-12Kh18N10 strip electrode of 60×0.5 mm section. Such a high portion of electrode metal allows assum-

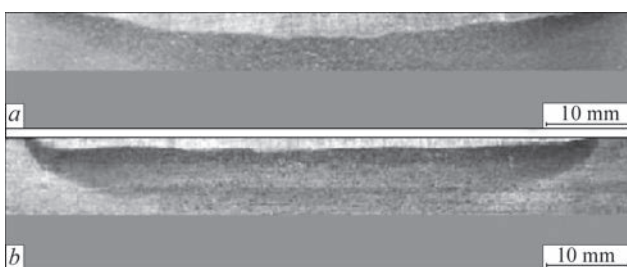


Figure 4. Macrosections of cross-section of penetration zone in surfacing by strip electrodes of 60×0.5 mm section from steel 08kp (a) and 12Kh18N10 (b)

ing that the composition of weld pool is close to the composition of strip electrode.

At the same time, carried investigations showed that the penetration area at constant surfacing mode using strip electrode Sv-12Kh18N10 reduces in comparison with surfacing with strip electrode Sv-08kp. Such effect of the composition of weld pool on geometry of penetration zone is related with heat transfer by convection [4]. Mathematical modelling and experimental investigations allow evaluating the effect of convection currents of molten metal in the pool on shape and size of the penetration zone. At that metal properties [5] are considered as a variable factor. Quantitative evaluation of the portion of heat transfer by convection in the total heat input balance verifies its significance [6].

The heat transfer by convection depends on thermophysical properties of the weld pool molten metal and first of all on enthalpy ΔH as well as on temperature determining melt flow of the pool. Evaluation of effect of melt enthalpy on efficiency of the base metal penetration in strip electrode surfacing was carried out by analysis of ΔH values (received experimentally [4] as well as by calculations [7, 8]). They characterize properties of the molten metal in a wide range, i.e. from weld pool temperature (1550–1750 °C) to drop metal transfer temperature (1900–2300 °C).

Carried analysis showed (the Table) that, regardless the difference of absolute values, the relationship of enthalpy of steels 12Kh18N10 and 08kp changes in small ranges. At the same time, determination of the penetration area using macrosections (Figure 4) as well as results of processing of data acquired in work [7] showed that the level of decrease of penetration area is correlated with reduction of enthalpy ΔH in the case of application of Sv-12Kh18N10 strip electrode instead of Sv-08kp.

If 70Cu-30Ni strip electrode is used (as shown by data processing), then the portion of electrode metal in the pool reaches 92–94 % and enthalpy of the metal

melt is significantly lower than for steel 12Kh18N10, particularly in comparison with steel 08kp. At that, the level of reduction of enthalpy of alloy 70Cu–30Ni in comparison with its value for steel 08kp $\Delta H^i/\Delta H^{st}$ is also correlated with decrease of penetration area.

Conclusion

Development of the technology of strip electrode surfacing, when the composition of weld pool is mainly determined by the composition of applied strip, requires consideration of effect of thermophysical properties of molten metal of the pool on penetration efficiency.

1. Ryabtsev, I.A. (2005) High-efficiency wide-layer surfacing using electrode wires and strips (Review). *The Paton Welding J.*, **6**, 31–35.
2. Kalensky, V.K. (1999) Specifics and some technological characteristics of electroslag cladding with one electrode strip. *Avtomatich. Svarka*, **3**, 16–21.
3. Matvienko, V.N., Mazur, V.A., Leshchinsky, L.K. (2015) Evaluation of shape and sizes of weld pool in surfacing using combined strip electrode. *The Paton Welding J.*, **9**, 28–31.
4. Lavrik, V.P., Leshchinsky, L.K., Pirch, I.I. (1985) Influence of thermophysical properties of strip electrode melt on nature of metal penetration in wide-layer surfacing. *Svarochn. Proizvodstvo*, **3**, 34–35.
5. Bahrami, A., Aidun, D.K. (2012) Modeling of transport phenomena in dissimilar welding of 2205 duplex stainless steel to 1018 carbon steel. In: *Proc. of 9th Int. Conf. on Trends in Welding Research*, 916–921.
6. Dmitrik, V.V., Shevchenko, V.V. (2001) Effectiveness in use of molten pool heat. *The Paton Welding J.*, **4**, 24–26.
7. Oh, Y.K., Davletian, J.H., Chen, S.J. (1990) Low-dilution electroslag cladding for shipbuilding. *Welding J.*, **8**, 37–44.
8. Soderstrom, E.J., Scott, K.M., Mendez, P.F. (2011) Calorimetric measurement of droplet temperature in GMAW. *Ibid.*, **4**, 77–84.

Received 28.04.2016

IMPROVEMENT OF CRACK RESISTANCE OF BANDED SUPPORTING ROLLS AT HIGH-SPEED SURFACING WITH LOW HEAT INPUT

S.V. SHCHETININ

Priazovsky State Technical University

7 Universitetskaya Str., 87500, Mariupol, Ukraine. E-mail: schetininSergey2012@yandex.ua

Improvement of crack resistance of banded supporting rolls is an urgent problem. The work is a study of the mechanism of improvement of deposited metal crack resistance with the aim of development of the process of high-speed surfacing of supporting rolls with low heat input. The method of X-ray structural analysis in diffractometer DRON-3 revealed that the electrode shape and heat input at surfacing have a considerable influence on microdistortions of crystalline lattice, which are responsible for microstresses. The latter lead to intensive formation and propagation of cracks, their initiation mechanism being associated with dislocations. Established regularities were confirmed at measurement of dislocation density by broadening of X-ray lines. Minimum crystalline lattice microdistortions, microstresses and dislocation density are achieved in surfacing with wire and composite electrode at a high speed and with minimum heat input. At increase of surfacing speed and lowering of heat input the rate of heating, cooling and solidification of liquid metal in the weld pool becomes higher, that provides microstructure refinement and increase of deposited metal crack resistance. A process of high-speed surfacing of banded supporting rolls with low heat input was proposed, providing an increase of crack resistance and preventing band failure. 13 Ref., 1 Table, 6 Figures.

Keywords: *high-speed surfacing with low heat input, crystalline lattice microdistortions, microstresses, dislocation density, welding stresses, crack resistance, banded supporting rolls*

Supporting rolls, which prevent sagging and breaking of working rolls, operate under the conditions of high specific stresses, therefore, surfacing of supporting rolls was not performed, particularly, of banded supporting rolls, which are manufactured by placing the band on the axle with interference fit. This results in stresses developing in the band, which may lead to failure. Therefore, improvement of crack resistance of banded supporting rolls is an important scientific-technical problem.

High-speed surfacing with a low heat input is an effective technique to improve crack resistance. However, its impact on deposited metal structure and properties has not been studied well enough [1–8].

The aim of this research is studying the mechanism of improvement of deposited metal crack resistance and development of the process of high-speed surfacing of banded supporting rolls with low heat input.

Electrode shape is one of surfacing process parameters, as the arc moving over the electrode tip, is concentrated in surfacing with wire, and is deconcentrated in surfacing ribbon electrode, depending on the position of which the arc moves along the longitudinal axis, or across the weld pool. Arc movement determines the heat input into the pool, and in constant surfacing mode also the rate of heating and cooling of liquid metal and HAZ. This changes the pool solidification conditions, diffusion processes, structural and phase transformations [5, 6], and deposited metal quality. However, the influence of electrode shape on deposited metal quality has not been sufficiently studied [7, 8].

Moreover, it is common knowledge that at heat input lowering the probability of cold cracking becomes higher, as a result of cooling rate increase.

However, Prokhorov [5] notes that a considerable lowering of heat input in welding and the respective increase of cooling rate may lead to lowering of cold cracking probability.

Electrode shape and heat input were found to have a considerable influence on arc movement, thermal cycles and solidification rate, which becomes higher with increase of welding speed as follows: $v_{sol} = \cos \Delta v_w$ (Figure 1). At surfacing with the same heat input by a perpendicular ribbon electrode, the rates of heating, cooling, and solidification are maximum. At surfacing by a longitudinal ribbon electrode, the arc movement along the weld pool results in increase of heat input into the side edges of the pool, and the rate of metal heating, cooling and solidification decreases. At surfacing with wire electrode, the rate of heating, cooling and solidification decreases even more, as a result of concentration and increase of heat input effectiveness. Minimum rate of heating, cooling and solidification is achieved in surfacing with a composite electrode, as a result of arc movement along rectilinear sections of ribbon electrode in the area of pool side edges. At a constant heat input, cooling rate decreases from 300 deg/s at surfacing with a perpendicular ribbon electrode to 60 deg/s at surfacing by a composite electrode.

With increase of welding speed and lowering of heat input, the rates of heating and cooling rise (Figure 2). Here, the heating rate rises much more – from 157 up to 500 deg/s. Cooling rate rises from 53 up to 120 deg/s.

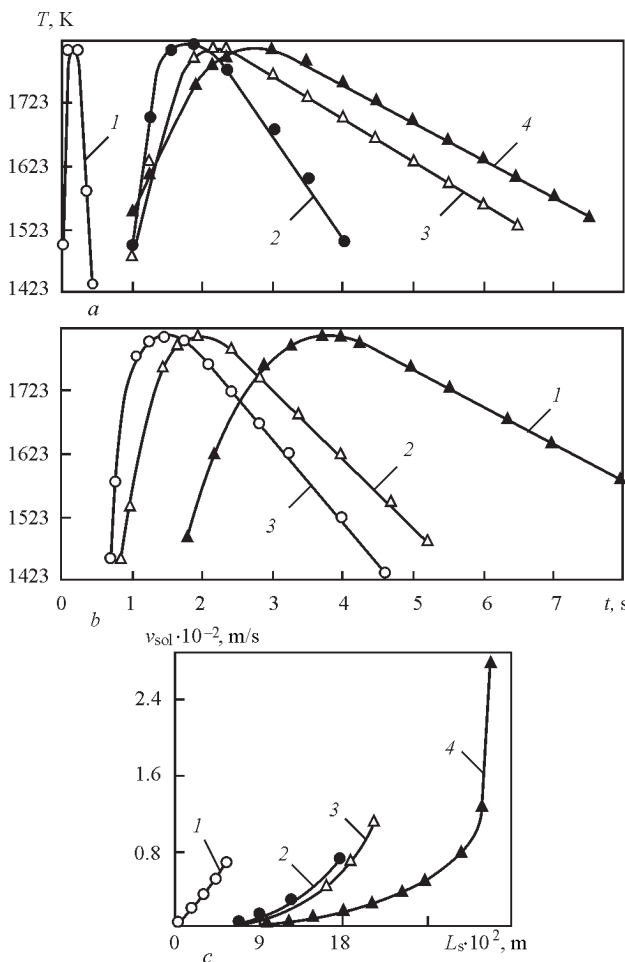


Figure 1. Regularity of impact of electrode shape on thermal cycle (a) and solidification rate of weld pool liquid metal (c) (1 — perpendicular ribbon electrode; 2 — longitudinal ribbon electrode; 3 — wire; 4 — composite electrode), and of heat input (1 — 3.6; 2 — 2.7; 3 — 1.8 MJ/m) on thermal cycle with composite electrode (b)

At high-speed surfacing the microstructure of deposited metal and HAZ is refined, that is the consequence of increase of heating and cooling rate, and greater number of solidification centers, which, being located ahead of the front of growing columnar crystallites, inhibit their further growth. At heating pearlite and ferrite transform into austenite. As a result of greater heating rate, austenite grains do not have enough time to grow, and austenite stability decreases. At cooling decomposition of unstable fine-grained austenite proceeds in the upper subcritical temperature range with formation of sorbite and pearlite, that prevents cracking.

At increase of welding speed and lowering of heat input, increase of heating and cooling rate results in increase of solidification rate (Figure 3), microstructure refinement and increase of deposited metal crack resistance.

Refinement of microstructure at high-speed surfacing with low heat input is accompanied by simultaneous lowering of welding stresses, the nature of formation of which is not fully understood.

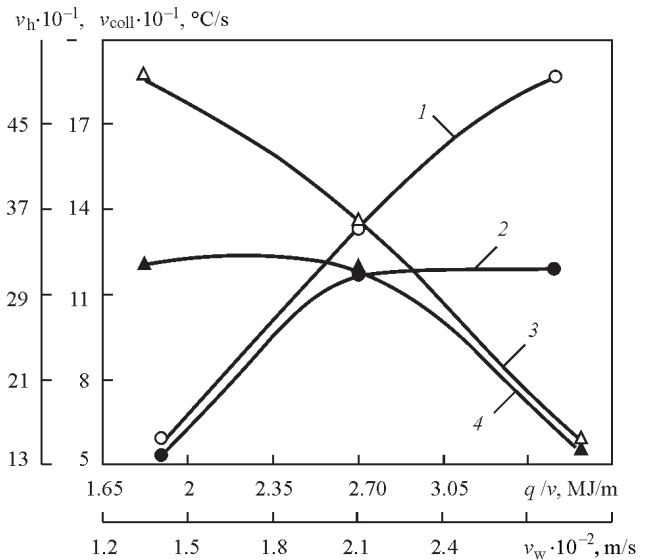


Figure 2. Dependence of the rate of heating (1, 3) and cooling (2, 4) of metal on welding speed (1, 2) and heat input (3, 4)

As a result of heat input during surfacing the metal is exposed to thermodeformational cycle, which is responsible for crystalline lattice microdistortions and microstresses. Thermodeformational cycle leads to development of inherent deformations and microstresses in the deposited metal, which determine crystalline lattice microdistortions [9]:

$$\sigma = E \frac{\Delta a}{a}, \text{ MPa}, \quad (1)$$

where $E = 19.68 \cdot 10^4$ MPa is the modulus of elasticity; $\Delta a/a$ are the crystalline lattice microdistortions.

Crystalline lattice microdistortions were determined at five-layer surfacing on plates of $(30 \times 300 \times 400) \cdot 10^{-3}$ m size with Sv08A wire of $4 \cdot 10^{-3}$ m diameter, with 08kp ribbon electrode of $(0.5 \times 45) \cdot 10^{-3}$ m size, positioned in the longitudinal or perpendicular directions, and composite electrode. Chemical composition of material used is given in the Table. Surfacing was performed using ceramic flux ZhSN-

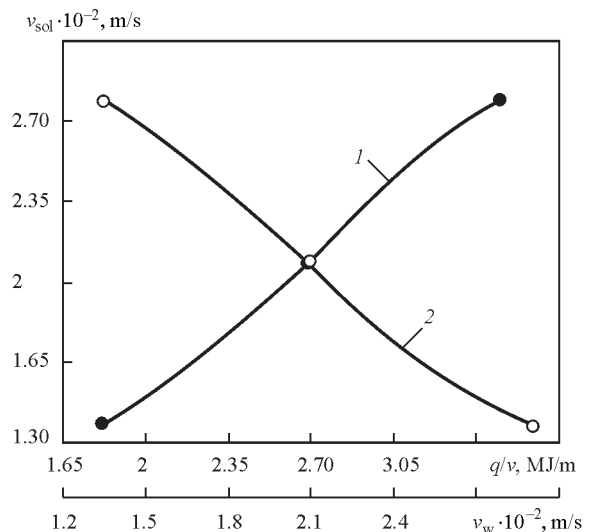


Figure 3. Dependence of solidification rate of weld pool liquid metal on welding speed (1) and heat input (2)

Composition of surfacing consumables, wt.%, acc. to GOST 2246–80, GOST 503–81, GOST 1050–88

Material	C	Mn	Si	Cr	S	P
Sv08A wire	≤ 0.1	0.35–0.60	≤ 0.03	≤ 0.12	0.025	0.030
08kp ribbon electrode	0.05–0.12	0.25–0.50	≤ 0.03	≤ 0.10		

5 in optimum modes characteristic for each process: for wire electrode — at $I = 650–750$ A, $U_a = 31–33$ V and $v_s = (0.56, 0.83, 1.1) \cdot 10^{-2}$ m/s; for longitudinal and perpendicular ribbon electrode — $I = 450–550$ A, $U_a = 29–31$ V and $v_s = (0.33, 0.5, 0.67) \cdot 10^{-2}$ m/s; for composite electrode — $I = 1950–2050$ A, $U_a = 29–31$ V and $v_s = (1.4, 2.1, 2.8) \cdot 10^{-2}$ m/s. Heat input for each surfacing process changed within $q/v = 1.8, 2.7$ and 3.6 MJ/m.

In order to control deposited metal quality, investigations of the influence of electrode shape and heat input on structural and phase transformations were conducted by measurement of crystalline lattice microdistortions, dislocation density, microstructure, microhardness of deposited metal and HAZ. Investigations of the value of crystalline lattice microdistortions were performed by the method of X-ray structural analysis in diffractometer DRON-3.

In arc surfacing vacancies form in the deposited metal under the impact of thermal excitation [5], as the energy of activation of vacancy generation is smaller than that of formation of interstitial atoms. In the zone of vacancy generation, static equilibrium of interatomic interaction forces is disturbed, that leads to displacement of adjacent atoms from their equilibrium positions and crystalline lattice microdistortions.

As was established, electrode shape and heat input have a significant influence on crystalline lattice microdistortions (Figure 4, a). At surfacing with perpendicular ribbon electrode at a low speed, high heat input results in metal oversaturation with excess vacancies [5], and crystalline lattice microdistortions are maximum. At surfacing with a longitudinal ribbon electrode, low-

ering of heat input leads to reduction of crystalline lattice microdistortions. Crystalline lattice microdistortions are even smaller at surfacing with wire at a higher speed. Minimum microdistortions of the crystalline lattice are achieved in surfacing with a composite electrode at a high speed and minimum heat input.

Change of heat input at surfacing with ribbon electrode, positioned perpendicular to and along the surfacing direction, does not influence crystalline lattice microdistortions, as a result of metal oversaturation with vacancies. Increase of the speed of surfacing with wire and composite electrode influences crystalline lattice microdistortions, which decrease with increase of surfacing speed and lowering of heat input. Minimum microdistortions of crystalline lattice are provided in surfacing with a composite electrode at speed of $2.1 \cdot 10^{-2}$ m/s, due to lowering of heat input and generation of Schottky vacancies.

In keeping with the influence of electrode shape and heat input on crystalline lattice microdistortions, maximum microstresses arise in the deposited metal in surfacing with a perpendicular ribbon electrode (Figure 4, b). In surfacing with a longitudinal ribbon electrode microstresses become smaller. In surfacing with wire electrode microstresses become even smaller. Microstresses decrease the most significantly in surfacing with a composite electrode with low heat inputs, as the level of plastic deformation decreases at lowering of heat input and accelerated cooling [10], that prevents failure.

Microstresses lead to intensive formation and propagation of cracks [5, 6], the mechanism of initiation of which is associated with dislocations [11].

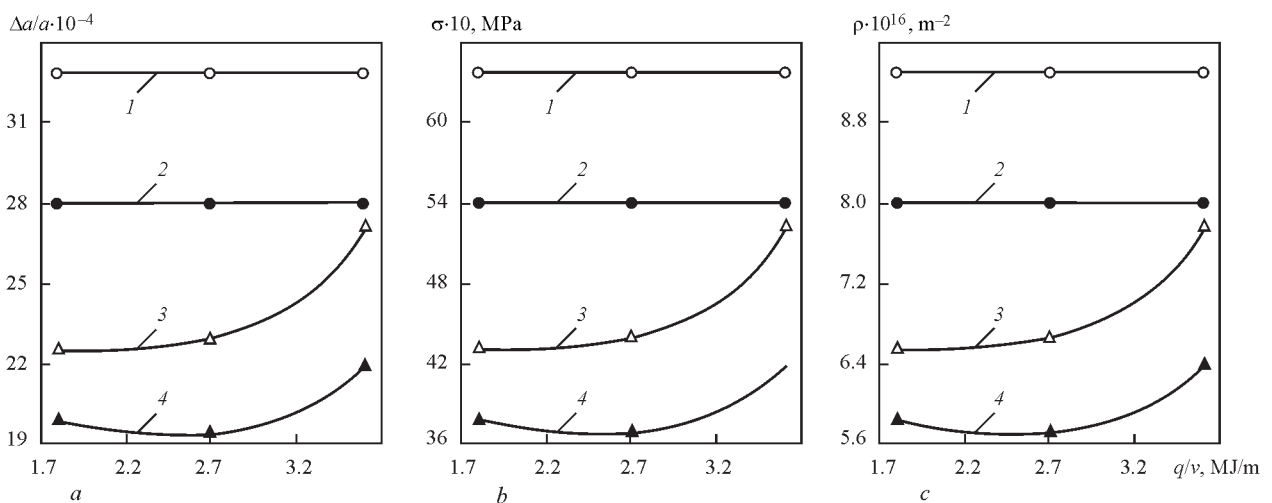


Figure 4. Regularities of impact of electrode shape and heat input on crystalline lattice microdistortions (a), microstresses (b) and dislocation density (c) in deposited metal: 1 — perpendicular ribbon electrode; 2 — longitudinal ribbon electrode; 3 — wire; 4 — composite electrode

Studying the influence of electrode shape and heat input on dislocation density was performed by broadening of X-ray lines [12]:

$$\rho = 3.46 \cdot 10^{19} \beta_{211}^2, \text{ rad} \cdot \text{m}^{-2}. \quad (2)$$

As a result it was established that maximum dislocation density is characteristic for surfacing with a perpendicular ribbon electrode, and decreases in surfacing with a longitudinal ribbon electrode (Figure 4, *c*). Dislocation density decreases in surfacing at wire and, particularly, with composite electrode with low heat input. This is in keeping with the influence of electrode shape and heat input on crystalline lattice microdistortions, as the totality of vacancies and nonmetallic inclusions (NMI) is the source of dislocations.

Assessment of the degree of deposited metal contamination by NMI and determination of their chemical composition were performed to clarify the established change of dislocation density.

Evaluation of the degree of deposited metal contamination by NMI was performed in optical microscope «Vertivol» at $\times 500$ magnification by a linear method. Contamination index was calculated as a ratio of total length of inclusions to total counted length, and chemical composition of NMI was determined by the method of X-ray spectral analysis in SEM-100U microscope and by the method of laser microspectral analysis in laser microspectroanalyzer LMA-10.

Examination in optical microscope at $\times 400$, $\times 500$ magnification and in SEM at $\times 1000$ magnification revealed that the deposited metal has NMI, which can be subdivided into two kinds: single spherical luminescent of more than $3 \mu\text{m}$ size (Figure 5, *a*) and a large number of spherical nontransparent ones of less than $1 \mu\text{m}$ size (Figure 5, *b*).

Degree of deposited metal contamination decreases with increase of surfacing speed, as a result of intensive convective flows and speed of liquid metal motion. The main NMI are manganese and silicon. Established influence of electrode shape and heat input on the degree of deposited metal contamination by NMI is in good agreement with their impact on dislocation density.

Established regularity of the impact of electrode shape and heat input on dislocation density leads to the conclusion that electrode shape and heat input affect deposited metal crack resistance, as a result of their influence on arc movement, thermal cycles and solidification rate.

It was found that microstructure dispersion (Figure 6) and deposited metal crack resistance are increased at increase of heating and cooling rate.

At surfacing with a longitudinal ribbon electrode, deposited metal microstructure is coarse-grained and non-uniform (Figure 6, *a*). In surfacing by a perpendicular ribbon electrode the microstructure is slightly refined, while remaining coarse-grained (Figure 6, *b*). Surfacing with wire and composite electrode leads to refinement of

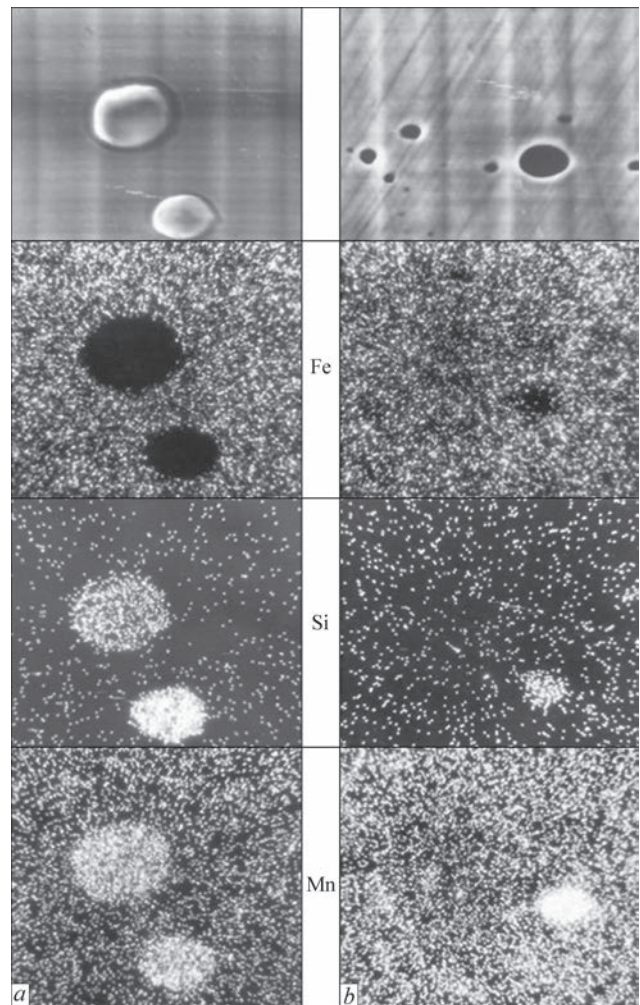


Figure 5. Nonmetallic inclusions of the size of more than $3 \mu\text{m}$ (*a* — $\times 1500$ with $1/2$ red) and less than $1 \mu\text{m}$ (*b* — $\times 4000$ with $1/2$ red) in X-ray spectrograms of distribution

microstructure (Figure 6, *c*, *d*), which is a ferrite-cementite mixture and is fine-grained and uniform.

Microstructure of deposited metal and HAZ is refined in a similar way in high-speed surfacing, that is the consequence of higher heating and cooling rate and greater number of solidification centers, which, being located ahead of the front of growing columnar crystallites, inhibit their further growth.

As a result of higher heating rate, austenite grains do not have enough time to grow, and austenite stability decreases. At cooling, decomposition of unstable fine-grained austenite occurs in the upper subcritical temperature range with formation of sorbite and pearlite, that prevents cracking. Minimum crystalline lattice microdistortions, microstresses, dislocation density and fine-grained uniform structure, result in increase of crack resistance.

In electric arc surfacing of banded supporting rolls of mill 3000 with higher heat input the band broke up.

To increase crack resistance and wear resistance of banded supporting rolls, an energy-saving technique of high-speed surfacing with a low heat input was developed [13]. High-speed surfacing of band-

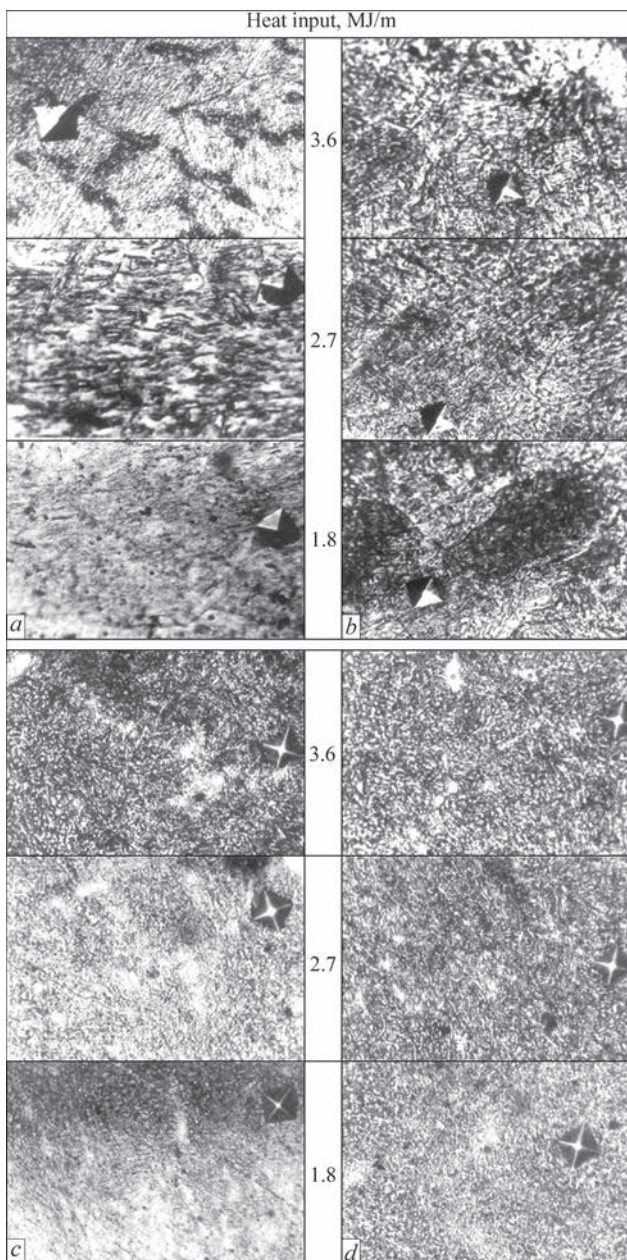


Figure 6. Microstructure ($\times 300$) of metal deposited with longitudinal (a), perpendicular (b) ribbon electrode, wire (c) and composite electrode (d) with different heat input

ed supporting rolls of mill 3000, which consist of an axle and band from steel 90KhF, was performed with preheating and concurrent heating up to 300–350 °C. First a buffer layer was deposited with low-carbon wire Sv-08G2S of 5 mm diameter using AN-60 flux, followed by a wear-resistant layer, deposited with flux-cored wire PP-Np-25Kh5FMS of 3.6 mm diameter using AN-26P flux with heat input of 1.1 MJ/m at $I = 750\text{--}800$ A, $U_a = 30\text{--}32$ V, $v_s = 75$ m/h. Surfacing was followed by heat treatment and delayed cooling. In high-speed surfacing of banded supporting rolls with low heat input the band did not break, that confirms the effectiveness of the process.

Developed energy-saving process of high-speed surfacing of banded supporting rolls with low heat input ensures minimum crystalline lattice microdistortions, microstresses, dislocation density and welding stresses, fine-grained uniform structure, high crack resistance and prevention of band failures.

Conclusions

1. Mechanism of improvement of deposited metal crack resistance in high-speed surfacing with low heat input due to lowering crystalline lattice microdistortions, microstresses, dislocation density and welding stresses was established. Minimum crystalline lattice microdistortions, microstresses and dislocation density are achieved in high-speed surfacing with low heat input with wire and composite electrode.

2. At increase of surfacing speed and lowering of heat input, the rate of heating, cooling and solidification of weld pool liquid metal decreases, that ensures refinement of the microstructure and higher of crack resistance.

3. A process of high-speed surfacing of banded supporting rolls with low heat input was developed, which provides lowering of welding stresses, refinement of microstructure, increase crack resistance and absence of band failures.

1. Frumin, I.I. (1961) *Automatic electric arc surfacing*. Moscow: Metallurgiya.
2. Frumin, I.I., Reznitsky, A.M. (1975) Application of dispersion-hardened steel for surfacing of primary mill rollers. *Avtomatich. Svarka*, **9**, 55–57.
3. Ryabtsev, I.A. (2004) *Surfacing of machine parts and mechanisms*. Kiev: Ekotekhnologiya.
4. Tylkin, M.A. (1975) *Improvement of life of metallurgical equipment parts*. Moscow: Metallurgiya.
5. Prokhorov, N.N. (1976) *Physical processes in metals during welding*. Moscow: Metallurgiya.
6. Shorshorov, M.Kh., Belov, V.V. (1972) *Phase transformations and changes of steel properties in welding*. Moscow: Nauka.
7. Savitsky, A.M., Savitsky, M.M., Novikova, D.P. (2004) Influence of welding speed and duration of periodical cooling on structure formation in welded joints of hardening steels in arc welding with thermal cycling. *The Paton Welding J.*, **8**, 39–43.
8. Musiyachenko, V.F., Mikhoduj, L.I., Pozdnyakov, V.D. (1990) Resistance to cold cracking of T-joints of high-strength steel in shielded-gas single-pass welding. *Svarochn. Proizvodstvo*, **2**, 13–15.
9. Gorelik, S.S., Rastorguev, L.N., Skakov, Yu.A. (1970) *X-ray structural and electrooptical analysis*. Moscow: Metallurgiya.
10. Myalin, M.I., Sagalevich, V.M., Turygin, V.N. et al. (1988) Influence of thermodeformation cycle on technological strength in surfacing of gray cast iron with bronze. *Svarochn. Proizvodstvo*, **3**, 10–11.
11. Finkel, V.M. (1970) *Physics of fracture*. Moscow: Metallurgiya.
12. Ivanov, A.N., Mezheny, Yu.O., Ostrov, A.E. (1987) Comparative determination of dislocations density in semicrystals by width of X-ray lines and electron microscopic analysis. *Zavod. Laboratoriya*, **2**, 43–48.
13. Bojko, V.S., Shchetynin, S.V., Klimanchuk, V.V. *Method of restoration and strengthening of cylindrical parts*. Pat. 65092 Ukraine. Int. Cl. B 23 K 9/04. Publ. 15.03.2004.

Received 26.10.2016

FORMATION OF WELD METAL STRUCTURE IN ELECTRON BEAM WELDING OF SINGLE CRYSTALS OF HIGH-TEMPERATURE NICKEL ALLOYS

K.A. YUSHCHENKO¹, B.A. ZADERY¹, I.S. GAKH¹ and O.P. KARASEVSKAYA²

¹E.O. Paton Electric Welding Institute, NASU

11 Kazimir Malevich Str., 03680, Kiev, Ukraine. E-mail: office@paton.kiev.ua

²G.V. Kurdyumov Institute for Metal Physics, NASU

35 Acad. Vernadsky Ave., 03680, Kiev, Ukraine. E-mail: Karas@imp.kiev.ua

Investigations of the features of temperature-rate parameters of weld pool metal solidification in EBW of single crystals of high-temperature nickel alloys were the basis for establishing the peculiarities of their influence on ensuring the single-crystal structure. Investigations were performed on single-crystal samples of commercial high-temperature nickel alloy JS26 with application of methods of thermometry of liquid pool melt during weld metal solidification at cooling. The structures were studied with application of methods of microprobe analysis, optical and electron metallography and XRD. A computational-experimental procedure for determination of temperature-rate parameters of weld metal solidification is proposed, the nature of their variation across weld pool solidification front is shown, and the interrelation with the welding modes is established. The range of parameter values was determined, in which grains with random crystallographic orientation form in the weld. The possibility of controlling the structural perfection of weld metal through optimization of temperature-rate parameters of solidification is shown. 23 Ref., 4 Tables, 10 Figures.

Keywords: *single crystal, high-temperature nickel alloy, temperature-rate conditions, temperature gradient, crystallographic orientation, weld, orientation of predominant crystal growth, direction of maximum temperature gradient, randomly oriented grains*

The degree of structure perfection is one of the main factors, determining service characteristics of single crystals of such high-temperature nickel alloys (HTNA) as heat resistance, ductility, fatigue resistance, etc. [1–10]. Quality of single-crystal structure is determined by the following crystallographic and structural features: crystallographic orientation and degree of disorientation of structural elements, parameters of structural components, and absence of grains differing from base metal by their crystallographic orientation.

In work [11–14] it is shown that the following features are the indications of structure perfection in welded joints of HTNA single crystals:

- structural alignment of weld metal, HAZ and base metal (with not more than 5° deviation);
- absence of randomly oriented grains in weld metal, which are considered to be the main defect of single crystals.

Producing such welds (Figures 1 and 2) is possible, when the following conditions are fulfilled:

- fusion surface and welding direction should not deviate from crystallographic orientation (001) by more than 3°;
- deviation of the direction of maximum temperature gradient from crystallographic orientation of pre-

dominant growth <100> on weld pool solidification front should be not more than 15°.

Technological support for fulfilling the first condition is provided by crystallographically oriented preparation of welded joint elements; and for the second condition it is ensured through control of weld pool shape at the stage of its solidification. The most favourable initial orientational conditions for producing welds with perfect single-crystal structure are provided at coincidence of butt edges with crystallographic plane {001} (see Figure 1) — symmetrical structure of the joint. In practice such initial conditions cannot always be ensured, for instance, in re-

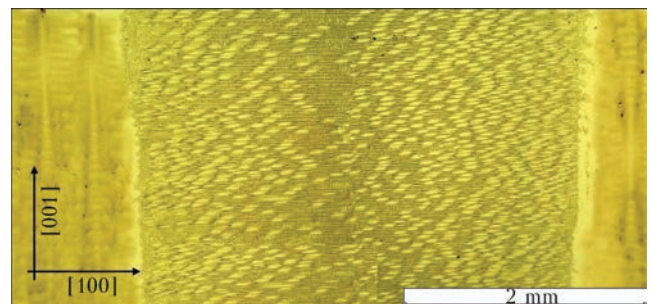


Figure 1. Microstructure of single-crystal welded joint of JS32 alloy produced when controlling orientational parameters of weld metal solidification

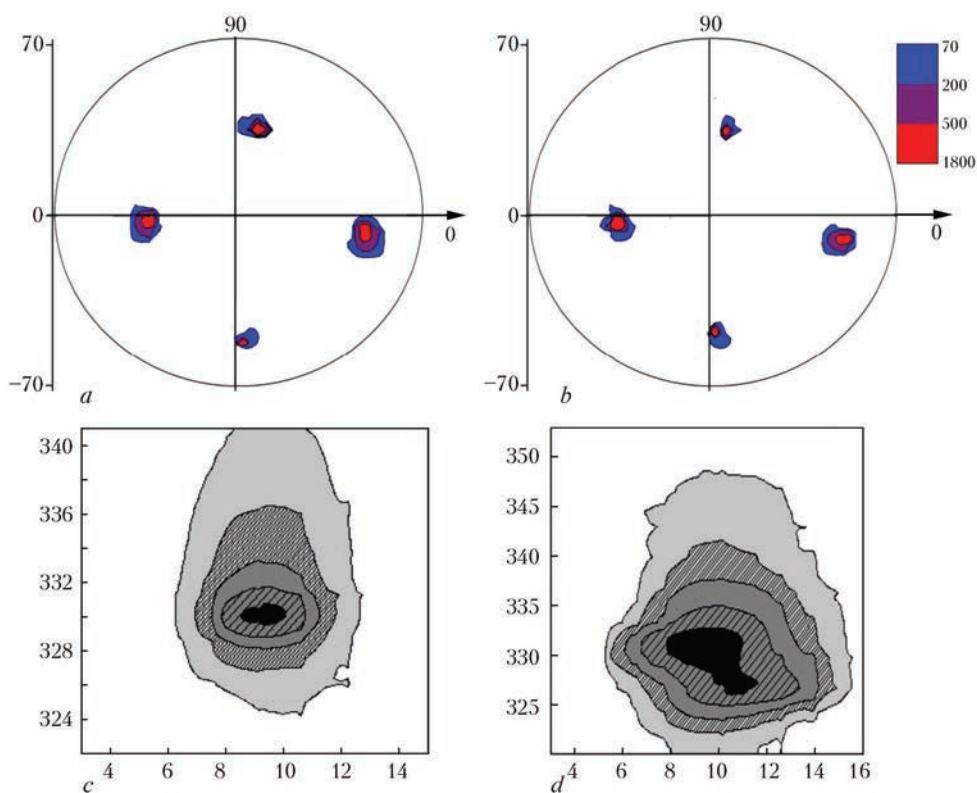


Figure 2. Pole figures $\{220\}$ (*a, b*) and Iq_L distribution of (200) reflection (*c, d*) in different zones of welded joint produced when controlling orientational parameters of weld metal solidification: *a, b* — BM, *c, d* — weld metal (numerical values along the axes are given in degrees)

pair operations, or in welding structures of a complex shape, as well as at performance of multipass welds.

In the joints with fusion surface initial orientation close to $\{111\}$, up to 80 % of randomly oriented grains can form in the weld metal. At unfavourable weld pool geometry in joints with symmetrical crystallographic structure, grain percentage can be equal to 4–10 %. Therefore, producing welds meeting the above quality criteria on single crystals of asymmetrical crystallographic orientation is a problem. Its solution was addressed, using the known postulate of the theory of crystallization, namely, the quality of single crystal growth is determined chiefly by crystallography of initial blank (seed) and temperature-rate conditions of solidification. It is known [6, 8–10] that optimum parameters of structure in casting HTNA single crystal growth are achieved, when temperature-rate and orientational conditions of directional solidification are provided. The main of them are evaluated by magnitude and direction of maximum temperature gradient G across the solidification front, solidification rate R , their ratio G/R , and crystallographic orientation of the starting seed.

When growing single crystals, these parameters determine solidification kinetics across the solidification front and have a dominant influence on formation of structural and crystallographic parameters of single-crystal casting (degree of perfection of sin-

gle-crystal structure, dendritic structure dispersion, morphology and size of secondary phases). G/R ratio determines the type and perfection of the structure and susceptibility to formation of randomly-oriented grains (ROG), and GR product determines the dispersity of structural components. When growing HTNA single crystals, optimum values of the above factors have been established and are achieved due to design features of equipment and technological parameters of liquid-metal cooler, heater and the process proper.

In welding such optimization is possible due to selection of distribution of heat source power, as well as rate and schematic of welded joint formation process. However, while the regularities of technological parameters influence on the extent of the change of the above temperature-rate conditions of formation have been well studied when growing single crystals [6, 8–10], such data for welding are quite limited in published sources, particularly, for substantiation of recommendations on controlling weld metal structure formation. Such a situation is attributable, mainly, to procedural difficulties, related to transient and non-equilibrium nature of the process of pool solidification, small volume and short time of its existence, high level and gradient of temperatures, variable rate and direction of crystallite growth across the weld pool front. The scarce publications give only the integral values of temperature gradient level and average

solidification rate [15–18]. These results were obtained predominantly by computational method, and the connection of thermophysical factors (G , R) of solidification with crystallographic and structural parameters of weld metal and technological conditions of joint formation is not revealed.

The objective of this work was studying the influence of temperature-rate and orientational conditions of solidification of weld pool metal on perfection of single-crystal structure, susceptibility to ROG formation, weld metal structure parameters, determination of the range of temperature-rate conditions of ROG formation in EBW of commercial HTNA with single-crystal structure.

In order to study the kinetics of temperature-rate parameters of solidification process at formation of weld metal structure, a special procedure was developed with application of local thermometry of liquid pool melt and weld metal in EBW. Proposed sample geometry and experimental schematic (Figures 3 and 4) allow evaluation of temperature parameters in a particular selected region of weld pool, in order to establish the interrelation with the characteristics of weld metal structure for this region.

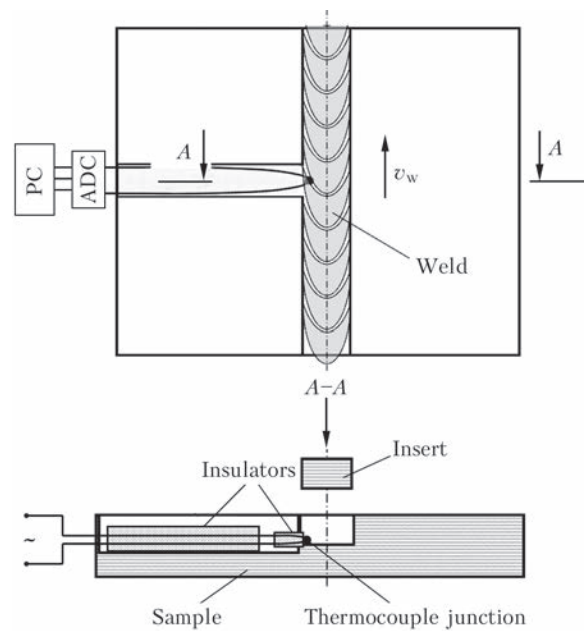


Figure 3. Schematic of thermometry of the process of weld metal solidification and sample geometry

Investigations were conducted on samples of commercial JS26 and JS32 HTNA with single-crystal structure (Table 1), 2.5 mm thick. Welding experiments were performed in the range of speeds of

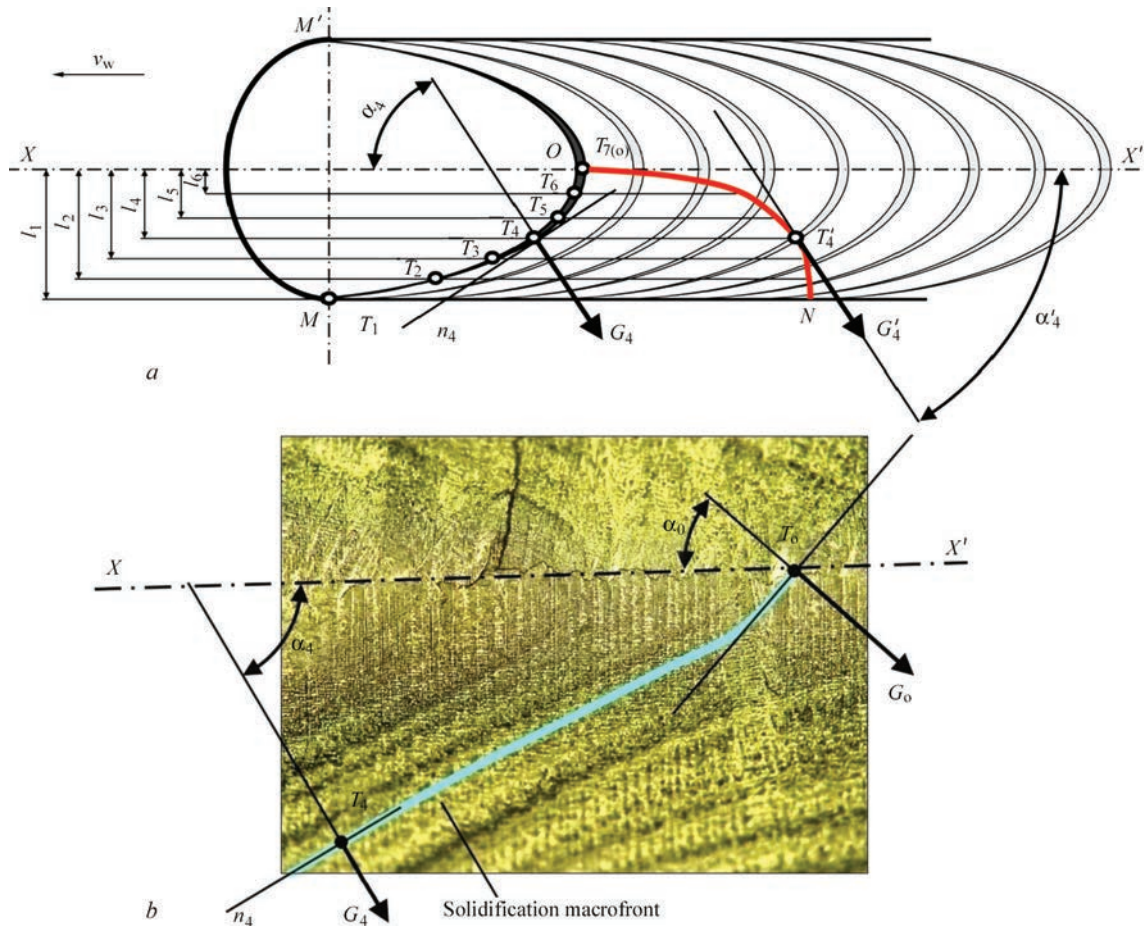


Figure 4. Schematic of weld pool (a) for evaluation of angle α of deviation of the direction of maxim temperature gradient G across weld pool solidification macrofront MOM' (b): ON — curve of the change of maximum temperature gradient over solidification macrofront across weld section; XX'' — weld axis

Table 1. Composition of the studied HTNA [10]

Alloy	Average values, wt. %											
	C	Cr	Co	W	Mo	Ti	Al	Nb	V	Re	Ta	B
JS26	0.15	5.0	9.0	5–15	0.5–5.0	0.2–4.0	4.5–8.0	1.6	1.0	–	–	0.01–0.30
JS32	0.15	5.0	9.3	2–10	0.5–5.0	–	4.5–8.0	1.5–5.0	–	4.0	4.0	0.01–0.30

12–90 m/h. Other parameter values were selected proceeding from the conditions of complete penetration and formation of welds with parallel fusion surfaces.

W-Re_s–W-Re₂₀ thermocouples of 0.2 mm diameter were used. Thermocouple junction of up to 0.8 mm diameter, made by EBW, was covered by powder of aluminium oxide with a binder. This provided a thin dielectric layer, preventing signal shunting, and not affecting measurement accuracy or thermocouple inertia. A set of equipment, including analog-digital converter EP-90118R, respective software and computer, was used for recording experimental data. Thermocouple readings were registered with the frequency of 10 Hz.

Results of processing the derived thermo-kinetic curves were used to assess the main parameters of thermal cycle of welding: maximum temperature, time of existence of weld pool melt and of weld metal staying in a certain temperature interval, its heating and cooling rate. Structural changes, depending on temperature-rate conditions of weld formation, were studied on welded joint macrosections, using the methods of microprobe analysis, metallography and X-ray diffractometry.

The following characteristics of weld structure were assessed: dendrite spacing λ ; dispersion and morphology of γ' -phase, eutectic components of γ - γ' -phases and carbide precipitates; dislocation density and distribution; ROG presence and nature.

Solidification rate \mathbf{R} and nature of its variation across weld pool front MO , according to schematic given in Figure 3, was assessed with 0.2–0.3 mm step with application of the known dependence [17]:

$$\mathbf{R} = v_w \cos \alpha, \quad (1)$$

where \mathbf{R} is the solidification rate; v_w is the welding speed; α is the angle between the direction of maximum temperature gradient and weld axis (see Figure 4).

Temperature gradient \mathbf{G} across the solidification front was determined, proceeding from Brody–Flemings relationship:

$$\lambda = A\mathbf{G}^m\mathbf{R}^n, \quad (2)$$

where λ is the value of dendrite spacing, coefficient A is proportional to solidification range ΔT , while the exponents at $m = n = 0.32$ express the distance between the axes of dendrites of the first order for HTNA [5, 10]. This relationship at preliminary determination of solidification rate and coefficient A al-

lows evaluation of temperature gradient \mathbf{G} across the solidification front and correlation of temperature-rate conditions and structural perfection of forming weld metal, on the one hand, and process parameters of welding mode, on the other.

Value of coefficient A for the studied EBW parameter range was determined by computation-experimental method in keeping with dependence (2). Here, cooling rate \mathbf{GR} was determined through tangent of the angle of inclination of linear section of thermogram near inflection point T_{L-S} , while dendrite spacing λ was measured on macrosections in the point of thermocouple location.

Microstructure of the metal of welds produced on single crystal samples at complete penetration with fusion surface orientation far from high symmetry {110}, {115} and {111}, is characterized by dendrite form of phase components in all the cases. Presence of both material volumes with inherited orientation of initial single crystal, and of randomly oriented grains is noted (Figure 5). Analysis of parameters of dispersion of weld metal dendritic structure in the range of welding speeds of 12–90 m/h showed that at EBW a high rate of heat removal from solidification front is ensured (Figure 6) and conditions for formation of fine cellular-dendritic structure are created. Minimum values $\lambda = 3\text{--}12 \mu\text{m}$, depending on the welding mode, are observed in the fusion zone, where maximum temperature gradient is in place. When getting closer to weld axis, value λ increases up to values of 25–55 μm , that corresponds to lowering of cooling rate \mathbf{GR} (Table 2). A feature of weld metal structure is the presence of a narrow zone at the fusion line (FL), which is characterized by clear inheritance of crystallographic orientation of base metal that is confirmed by the results of X-ray (see Figure 5) and metallographic (Figure 7) studies. This zone is a region of epitaxial growth 0.1–0.5 mm wide without any ROG (see Figure 5, *c*, *d*). Distribution of the intensity of X-ray reflection $I_{\mathbf{q}_\perp}$ is relatively smooth, close to that of the initial metal. Isointensive lines have the form of ellipsoidal curves (see Figure 5, *d*), that corresponds to single-crystal state of metal with uniform distribution of edge dislocations [19–23].

Presence of such a zone with clear inheritance of initial crystallographic orientation points to the possibility of formation of a single-crystal weld under any orientational conditions.

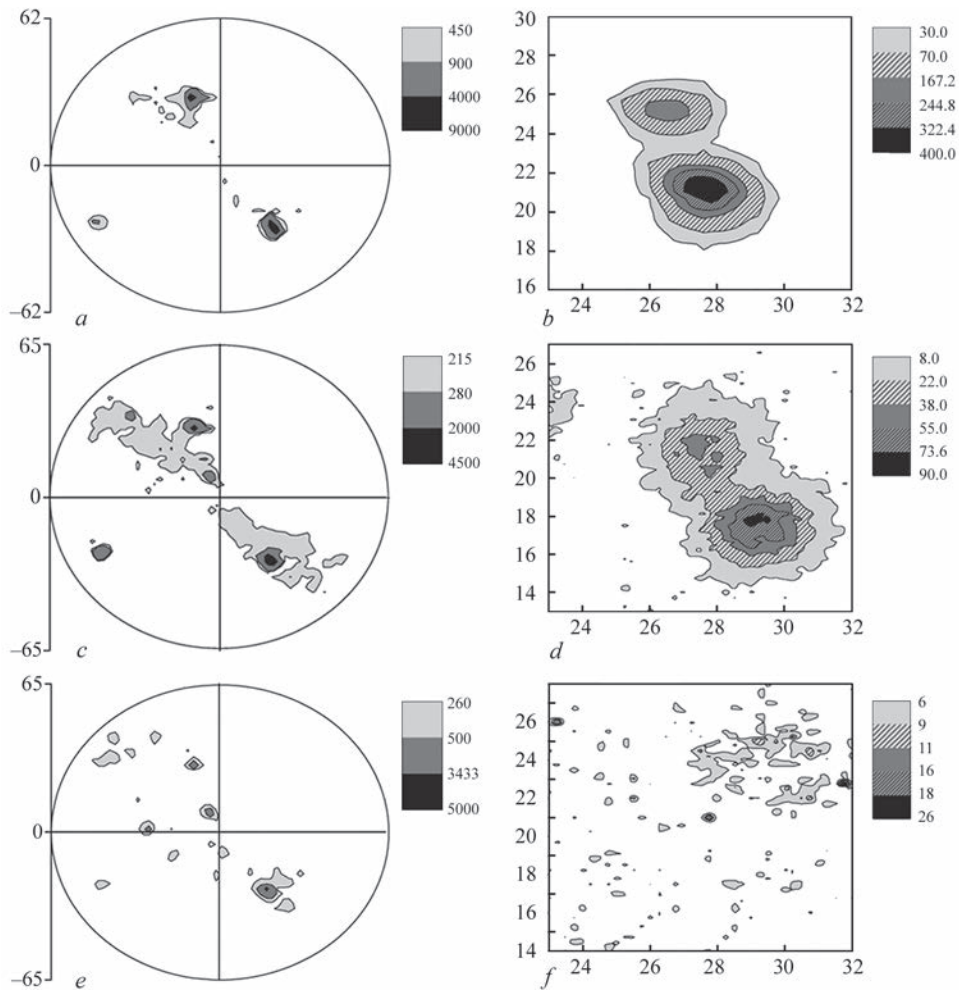


Figure 5. Pole figures $\{220\}$ and Iq_L distribution of (022) reflection in different zones of welded joint of asymmetrical crystallographic orientation: *a, b* — BM; *c, d* — weld at the FL; *e, f* — weld axis

Derived experimental results (Figure 8) confirm the known theoretical postulate [17] that thermal conditions across the solidification front change as the dendrites grow from the fusion line towards weld axis. Temperature gradient G has maximum values at the FL and decreases towards weld axis, while solidification rate R here changes from minimal value at the FL to maximum one at weld axis. Under such thermal conditions of weld metal solidification, a high stability of directional growth of dendrites and maximum refinement of the dendritic structure — up to $\lambda \sim 3 \mu\text{m}$, are ensured in the narrow zone at the FL.

Refinement of structural components of single crystals at optimization of EBW parameters results in a significant reduction of structural and segrega-

tional inhomogeneity [10], the main point being improvement of the stability of directional solidification across the front of crystal growth. Analysis of the results of studying the structure and temperature-time and orientational parameters of solidification in different regions of solidification front (Table 3) leads to the conclusion that violation of the perfection of single-crystal structure, that is most often manifested in formation of ROG, occurs in the regions where the value of G/R ratio is below the admissible level, which depends on the magnitude of angular deviation

Table 2. Dependence of dendrite structure parameters of JS26 alloy on EBW speed

v_w , m/h	Weld metal λ at FL, μm	Weld metal λ on its axis, μm
90	3.4	33.3
53	3.3	25.0
17	12.5	56.3

Note. BM $\lambda = 200\text{--}230 \mu\text{m}$.

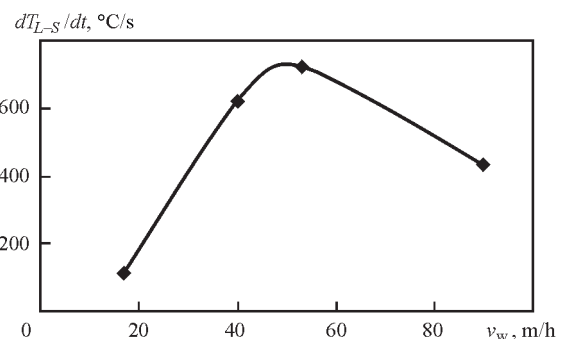


Figure 6. Dependence of cooling rate across solidification front on speed of EBW of JS26 alloy 2.5 mm thick

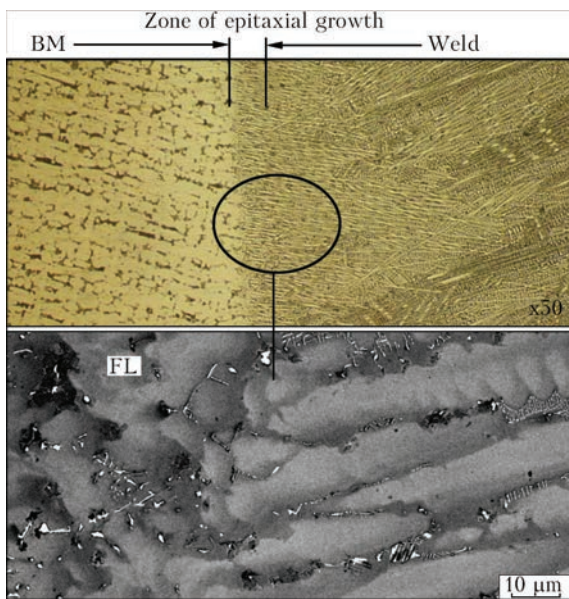


Figure 7. Microstructure of metal of the JS26 joint alloy of asymmetrical crystallographic orientation

of the direction of maximum temperature gradient from predominant growth orientation $\langle 100 \rangle$ across the solidification front (Table 4).

In the considered range of welding modes and thicknesses, 40–50 m/h can be regarded as the optimum speed, at which sound formation of the weld with through-thickness penetration and fusion surfaces close to parallel ones is provided. Some discrepancy with the generally accepted concepts of the influence of welding speed on weld formation and its structure is attributable to the nature of distribution of heat input, which is in place at such penetration between weld pool melt, HAZ and energy removed from penetration channel. When temperature-rate parameters of solidification of the order of $G/R = 65 \cdot 10^3 \text{ s} \cdot \text{°C}/\text{mm}^2$ are reached, the admissible orientation range is expanded considerably, and conditions

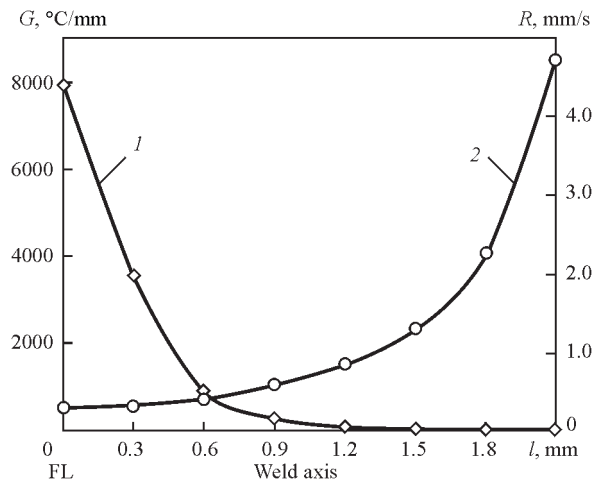


Figure 8. Change of temperature-rate conditions of directional solidification across weld pool solidification front at welding speed of 17 m/h: 1 — value of maximum temperature gradient G ; 2 — crystallite growth rate R

are in place for directional solidification of weld metal at large angles of deviation $\varphi \geq 45^\circ$ of maximum temperature gradient direction from predominant growth orientation $\langle 001 \rangle$ across the pool solidification front.

It is obvious that at such temperature-rate conditions the zone of concentrational overcooling ahead of solidification front is narrowed to the level, at which thermomechanical fluctuations cannot lead to nucleation of new solidification centers [5]. It should be noted that the results shown in Figure 8 and Table 3 are given as an illustration of realization of the proposed procedural approach. In this study, investigations were performed on samples with different crystallographic orientations, welding modes and conditions, the results of which led to certain conclusions. Figures 9 and 10 show one of the results of such an approach. In welding of crystallographically asymmetrical samples (Figure 10, a) a weld with perfect single crystal structure was formed (Figures 9

Table 3. Temperature-rate parameters of weld metal solidification across weld pool solidification front at welding speed of 53 m/h obtained by computation-experimental method

Point number	$l, \text{ mm}$	$R, \text{ mm/s}$	$G, \text{ °C/mm}$	$GR, \text{ °C/s}$	$G/R, \text{ s} \cdot \text{°C}/\text{mm}^2$
1	FL	1.28	139074	178015	108652
2	FL + 0.3	2.0	48828	97656	24414
3	FL + 0.6	2.6	591	1537	227
4	FL + 0.9	3.3	219	722	66
5	FL + 1.2	3.8	161	612	42
6	FL + 1.5	4.5	97	437	22
7	FL + 1.8 (weld axis)	11.09	29	321	2.6

Note. l — distance from the fusion line.

Table 4. Admissible deviations φ of the direction of maximum temperature gradient G from predominant crystal growth orientation $\langle 001 \rangle$ across weld pool solidification front depending on G/R value

$\varphi, \text{ deg}, \leq$	0–5	10–15	20	25	30	35	40–45
$G/R, \text{ s} \cdot \text{°C}/\text{mm}^2$	0.2–0.23	1.2–1.5	230	1500	$19 \cdot 10^3$	$25 \cdot 10^3$	$(62–68) \cdot 10^3$

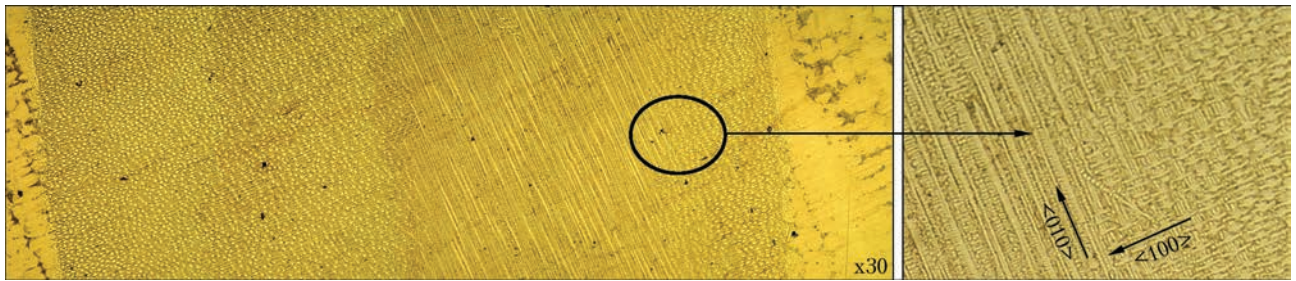


Figure 9. Weld metal microstructure with initial asymmetrical crystallographic orientation of welded joint produced with control of temperature-rate parameters of weld pool solidification

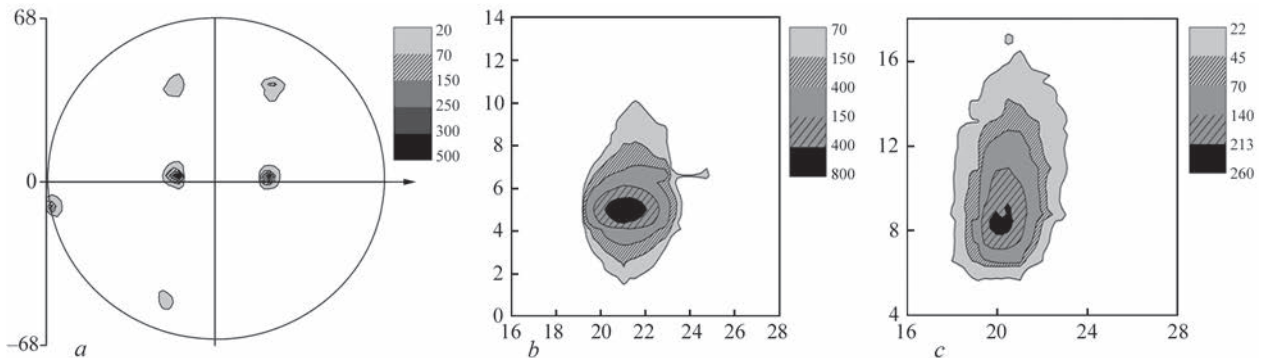


Figure 10. Pole figures $\{311\}$ of metal being welded (a) and $I_{q\perp}$ distribution of reflection (311) (b, c) in different zones of welded joint with asymmetrical crystallographic orientation produced with control of temperature-rate parameters of weld pool solidification: b — BM; c — weld metal (numerical values along the axes are given in degrees)

and 10, c). Just a change of crystallographic index of weld metal orientation from $\langle 100 \rangle$ to $\langle 010 \rangle$ is found in high-gradient zone of epitaxial growth. Here, no grains formed, and, on the whole, a weld with single-crystal structure was produced.

Thus, it is shown that optimization of temperature-rate parameters of solidification of weld pool metal through selection of welding modes enables producing welded joints with perfect single-crystal structure at a large ($\varphi \sim 45^\circ$) deviation of the direction of maximum temperature gradient from predominant growth orientation $\langle 100 \rangle$. Such an approach will allow development and introduction into production of a technology of welding and repair of single-crystal items of a complex shape.

Conclusions

1. A computational-experimental procedure is proposed for evaluation of temperature-rate parameters of solidification across the front of weld pool solidification in EBW.

2. The range of temperature-rate parameters of the process of solidification of weld pool of JS26 alloy was determined, in which a high perfection of single-crystal structure of weld metal and absence of randomly oriented grains are ensured. So, at deviation of maximum temperature gradient direction from predominant growth orientation $\langle 100 \rangle$ of the order of $\varphi = 5^\circ$, directional solidification of weld met-

al is preserved at $G/R \geq 0.20\text{--}0.23 \text{ s}\cdot^\circ\text{C}/\text{mm}$, and at $\varphi \sim 45^\circ$ — $G/R \geq (62\text{--}68) \cdot 10^3 \text{ s}\cdot^\circ\text{C}/\text{mm}$.

3. Shown is the possibility of controlling formation of weld metal structure in EBW of single crystals of high-temperature nickel alloys through optimization of temperature-rate parameters of the process of weld pool metal solidification, that allows producing joints with perfect single-crystal structure in weldments with crystallographically asymmetrical structure of the joint.

- (1995) *Superalloys II: Heat-resistant materials for aerospace systems and industrial power plants*. Book 1. Moscow: Metallurgiya.
- Erickson, G.L., Harris, K. (1994) DS and SX superalloys for industrial gas turbines. In: *Proc. of Conf. on Materials for Advanced Power Engineering* (Belgium, 3–6 Oct. 1994), Pt 2, 1055–1074. Kluwer Acad. Publ.
- Erickson, G.L. (1995) A new third generation single crystal, casting superalloy. *J. of Metals*, 47(4), 36–39.
- (2006) *Cast heat-resistant alloys. S.T. Kishkin effect*. Sci-techn. coll. Moscow: Nauka.
- Shalin, R.E., Svetlov, I.L., Kachanov, E.B. et al. (1997) *Single crystals of nickel heat-resistant alloys*. Moscow: Mashinostroenie.
- Stroganov, G.B., Chepkin, V.M. (2000) *Cast heat-resistant alloys for gas turbines*, 63–65. Moscow: ONTI MATI.
- Shah, D.M., Duhl, D.N. (1984) Effect of orientation, temperature and gamma prime size on the yield strength of a single crystal nickel base superalloy. In: *Superalloys*, 105–114. Metallur. Soc. of AIME.
- Kishkin, S.T., Stroganov, G.B., Logunov, A.V. (2001) *Nickel-based cast heat-resistant alloys*. Moscow: MISIS.

9. Dong, H.B., Yang, X.L., Lee, P.D. (2004) Simulation of equiaxed growth ahead of an advancing columnar front in directionally solidified Ni-base superalloys. *J. Materials Sci.*, **39**, 7207–7212.
10. Kablov, E.N. (2001) *Cast blades of gas-turbine engines (alloys, technology, coatings)*. Moscow: MISIS.
11. Yushchenko, K.A., Gakh, I.S., Zadery, B.A. et al. (2013) Influence of weld pool geometry on structure of metal of welds on high-temperature nickel alloy single crystals. *The Paton Welding J.*, **5**, 45–50.
12. Yushchenko, K.A., Zadery, B.A., Gakh, I.S. et al. (2013) On nature of grains of random orientation in welds of single crystals of heat-resistant nickel alloys. *Metallofizika i Nov. Tekhnologii*, **35(10)**, 1347–1357.
13. Yushchenko, K.A., Zadery, B.A., Zvyagintseva, A.V. et al. (2008) Sensitivity to cracking and structural changes in EBW of single crystals of heat-resistant nickel alloys. *The Paton Welding J.*, **2**, 6–13.
14. Gakh, I.S. (2011) *Physical-technological peculiarities of electron beam welding of high-nickel heat-resistant alloys with single-crystal structure*: Syn. of Thesis for Cand. of Techn. Sci. Degree. Kiev: PWI.
15. Rabkin, D.M., Ignatiev, V.G., Dovbishchenko, I.V. (1982) *Arc welding of aluminium and its alloys*. Moscow: Mashinostroenie.
16. Rykalin, N.N. (1951) *Calculations of thermal processes in welding*. Moscow: Mashgiz.
17. Frolov, V.V., Vinokurov, V.A., Volchenko, V.N. et al. (1988) *Theoretical principles of welding*. Moscow: Vysshaya Shkola.
18. Solomatova, E.S., Trushnikov, D.N., Belenky, V.Ya. et al. (2014) Evaluation of temperature in vapor gas channel in EBW of dissimilar metals. *Sovr. Problemy Nauki i Obrazov.*, **2**, 21–26.
19. Panin, V.E., Likhachev, V.A., Grinyaev, Yu.V. (1985) *Structural levels of deformation of solids*. Novosibirsk: Nauka.
20. Likhachev, V.A., Panin, V.E., Zasimchuk, E.E. et al. (1989) *Cooperative deformation processes and localization of deformations*. Kiev: Naukova Dumka.
21. Malygin, G.A. (1995) Self-organizing of dislocations and localization of slipping in plastically deformed crystals. *Fizika Tv. Tela*, **37**(Issue 1), 3–42.
22. Sarafanov, G.F. (1998) To theory of formation of heterogeneous dislocation structures. *Fizika Metallov i Metallovedenie*, **85**(Issue 3), 46–53.
23. Koneva, N.A., Kozlov, E.V. (1990) Physical nature of staging of plastic deformation. *Izvestiya Vuzov, Fizika*, **2**, 89–106.

Received 17.05.2016

PECULIARITIES OF DEVELOPMENT OF STRUCTURAL HETEROGENEITY IN THE FUSION ZONE OF PEARLITE STEEL WITH AUSTENITIC NITROGEN-CONTAINING WELD METAL*

V.P. ELAGIN, V.N. LIPODAEV and G.N. GORDAN

E.O. Paton Electric Welding Institute, NASU

11 Kazimir Malevich Str., 03680, Kiev, Ukraine. E-mail: office@paton.kiev.ua

The peculiar features of development of structural heterogeneity at high-temperature heating in the unstable fusion zone of the austenitic weld with the pearlite steel were considered. It was shown that one of the factors influencing the high nickel content in the weld and low heat input of welding on reduction of width of ferrite interlayer is the decrease in overheating and degradation of carbides in the HAZ metal. However, these changes do not prevent the film precipitation of carbides and embrittlement of metal between the fusion zone and the HAZ. The alloying of austenitic weld metal with nitrogen, formation of nitride particles being more stable than the carbides, and refining the grains facilitate the increase in stability of structure, inhibition of carbide reactions and more uniform distribution of carbides in the fusion zone with pearlite steel, which improves the properties of welded joints of dissimilar steels. 14 Ref., 7 Figures.

Keywords: arc welding, welded joints of dissimilar steels, fusion zone, structural heterogeneity, diffusion of carbon, austenitic weld, nickel, nitrogen, decarburized zone, carburized zone, heat affected zone

During manufacture and repair of petrochemical, oil refining, power and other technological equipment the welded joints of dissimilar austenitic and pearlitic steels are applied, which operate at the high (above 350 °C) temperatures. To the joints of dissimilar steels the joints of heat-resistant alloyed steels with austenitic weld are also referred produced in case when the postweld heat treatment is impossible. The welding of such steels is carried out with the use of austenitic materials with a high (more than 13 %) nickel content. At the same time, the compliance of nickel content in the weld metal with the level of alloying of the pearlite steel and operating temperature is provided. The non-compliance of this condition results in development of structural heterogeneity in the fusion zone of the pearlite steel and the austenitic weld as a result of redistribution in carbon diffusion. Such a fusion zone is considered to be unstable [1].

The characteristic features of structural heterogeneity in the unstable fusion zone is the presence of interlayers, i.e. the carburized one with a high hardness in the transition layer of austenitic weld and the ferrite one with a low hardness in the HAZ of pearlite steel. The diffusion of carbon is facilitated by the gradient of its thermodynamic potential between the

austenitic weld and the pearlite steel [1–3]. In the austenitic weld it has lower values due to the presence of strong carbide-forming elements such as chromium, molybdenum, vanadium, etc. which bind carbon into carbides. In the pearlite steel a higher value of potential is caused by the presence of unstable carbides and free carbon in the solid solution.

The transportation of carbon in the unstable fusion zone occurs according to the mechanism of both atomic and reactive diffusion [2]. During the atomic diffusion free carbon in the solid solution of metal is moved towards a stronger carbide-forming element. The reactive diffusion occurs as a result of carbide reactions which proceed with the dissociation of less stable carbides, diffusion of carbon to the fusion zone and the formation of more alloyed carbides. The decomposition of carbides in the HAZ is facilitated by the reduction in carbon content in the solid solution and a high temperature of heating during welding [4] or during service [3]. There is no unanimous opinion about the nature of welding heat input affecting the width of ferrite interlayer. In work [1] it was shown that the reduction in welding heat input contributes to its increase, and in work [5], on the contrary, it caus-

*According to the materials of the paper presented at the International Conference «Arc welding. Materials and quality» (Volgograd, RF, May 31–June 3, 2016).

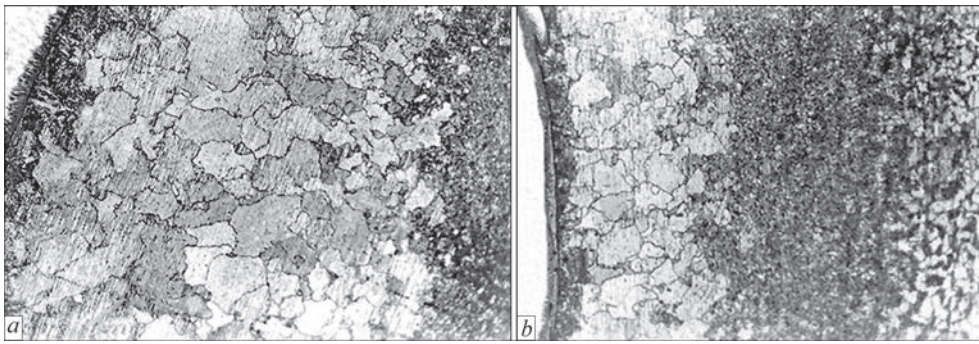


Figure 1. Microstructure (x100) of HAZ metal with ferrite interlayer of steel 20 in single-layer metal of type 08Kh25N40M7 deposited in $\text{CO}_2 + 5\% \text{N}_2$ at heat input of 7.9 (a) and 4.1 (b) kJ/cm and heating at 550 °C for 3000 h

es its decreases at the reduced power density of laser treatment.

The application of high-nickel welding consumables is the most effective way to reduce the structural heterogeneity [1–3]. The effect of nickel is explained by increase in thermodynamic activity and reduction in the solubility of carbon in austenite [1].

However, at the unstable fusion zone a high nickel content in the weld, even in the amount characteristic for nickel alloys, does not fully prevent the carbon diffusion and the formation of structural heterogeneity. It was established in the fusion zone with low-carbon steel [6], where the carbon is in the composition of unstable cementite, or with heat-resistant alloyed steel with the structure of martensite in the HAZ metal [4]. The presented review demonstrates that until the present time the mechanism of structural heterogeneity formation in the unstable fusion zone of heterogeneous steels and the influence of nickel on it was not fully disclosed.

The positive effect of the austenitic weld alloying with nitrogen on reduction of carbon diffusion at the zone of its fusion with pearlite steel is known [7]. Nitrogen, the same as nickel, contributes to thermodynamic activity of carbon [8]. Moreover, nitrogen can be included into the composition of carbides, changing their composition and stability as well as forming nitrides with such elements as titanium, niobium, chromium, etc., which are more stable than carbides [9, 10]. This fact, apparently, will influence the reactive diffusion of carbon. Earlier, the investigations of influence of the austenitic weld alloying with nitrogen on development of the decarburized interlayer in pearlite steel were not carried out. Taking into account the positive effect of nitrogen on properties of the austenitic weld metal [11] and that of welded joints of dissimilar steels [12], such investigations represent a scientific and practical interest.

The aim of this work is the comparison of effectiveness of influence of the austenitic weld alloying with nitrogen and nickel on development of structur-

al heterogeneity in the unstable zone of fusion with pearlite steel.

To conduct investigations the single layer beads were deposited on the plate of steel 20 of 22 mm thickness using mechanized welding in shielding gas using austenitic wires of 1.2 mm diameter with the alloying of type 08Kh20N9G7T, 08Kh20N25M8G8 and 08Kh25N40M7. These wires are recommended for welding of dissimilar steels in the structures operating at different temperatures [1]. As a shielding gas Ar, CO_2 , N_2 and their mixtures $\text{CO}_2 + 5\text{--}80\% \text{N}_2$ were used, which allowed obtaining the nitrogen content in the amount of 0.04–0.06 and 0.12–0.39 wt.%, respectively, in the metal of austenitic deposit. The surfacing was performed at heat input of 4.1 and 7.9 kJ/cm at the following mode parameters: $I_w = 240\text{--}260 \text{ A}$, $U_a = 24\text{--}26 \text{ V}$, $v_w = 16$ and 25 m/h. In order to develop the structural heterogeneity, the welded joints were subjected to furnace heating at 550 °C for 1000, 1500 and 3000 h.

The choice of heating temperature equal to 550 °C and carbon steel 20 as the base metal, containing no active carbide-forming elements, allowed obtaining a structural and phase instability which resulted in the development of structural and mechanical heterogeneities in the fusion zone. To reveal the structure of metal the metallographic etching of microsections was applied in 5% alcoholic solution of nitric acid. The hardness of metal was measured using PMT-3A device at load of 0.2 N, and the distribution of carbon was determined using «Cameca» microanalyzer SX-50.

The investigations showed that after the long heating a ferrite interlayer is formed in the HAZ of pearlite steel of all the variants of surfacing. It represents a clearly expressed interlayer with a ferrite structure, the grain size in which increases as it approaches the fusion zone (Figure 1). The width of the interlayer becomes larger at the longer heating and decreases at the reduction of welding heat input and at the increase in the content of nickel in the electrode and the content of nitrogen in the composition of shielding gas. The effectiveness of influence of these indicators on the

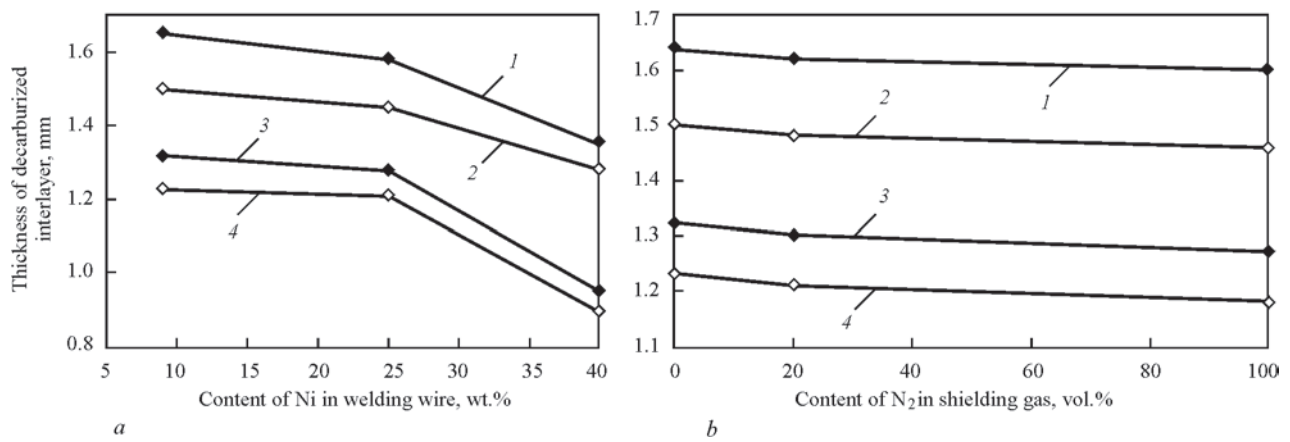


Figure 2. Dependence of ferrite interlayer width in the steel 20 HAZ with single-layer austenitic deposit on content of nickel in welding wire (*a*) and nitrogen in shielding gas mixture (*b*) at heat input of 7.9 (1, 2) and 4.1 (3, 4) kJ/cm and heating at 550 °C for 3000 (1, 3) and 1000 (2, 4) h

width of ferrite interlayer was evaluated by comparing the values of the curve points shown in Figure 2.

The reduction in welding heat input from 7.9 to 4.1 kJ/cm during welding using the wire with 9 and 25 wt.% Ni leads to reduction in the width of a ferrite interlayer approximately by 18 and 20 % after 1000 and 3000 h heating, respectively. During welding using the wire with 40 wt.% Ni the influence of heat input becomes more efficient, i.e. the width of an interlayer is reduced by approximately 28 and 30 % after 1000 and 3000 h heating duration, respectively.

During welding with heat input of 7.9 kJ/cm the application of welding wire with nickel content of 25 and 40 % reduces the width of the decarburized interlayer approximately by 3 and 15 %, respectively, at heating duration of 1000 h, and nearly by 4 and 18 %, respectively, at 3000 h heating. At the reduction of heat input to 4.1 kJ/cm, the effect of increasing the nickel content up to 25 and 40 wt.% becomes more effective, i.e. approximately 4 and 18 %, respectively, at the heating duration of 1000 h and by nearly 26 and 28 %, respectively, at 3000 h holding. These relations are observed at any composition of shielding gas.

The alloying with nitrogen reduces the width of ferrite interlayer approximately by 5 % during surfacing of metal of type 08Kh20N9G7T and 08Kh20N-25M8G8 and the metal of type 08Kh25N40M7 by 3 % at any welding heat input. Such a change of decarburization is approximately equal both at mass fraction of nitrogen in the weld of 0.12 % and also at 0.22 %, i.e. the dependence of its width in the joints of steel 20 on the amount of nitrogen in the austenitic metal in the investigated ranges was not detected.

Thus, the decrease in heat input of welding has a stronger influence on reduction of a ferrite interlayer width than an increase in nickel content up to 40 wt.%. The influence of the weld metal alloying with nitrogen has the same effect on reduction in the

width of a ferrite interlayer as an increase in nickel content up to 25 %.

The width of a ferrite interlayer for all the investigated variants of surfacing is within the range of the HAZ and is proportional to its width. The reduction of the HAZ width is facilitated not only by decrease in the heat input, but also by increase in the nickel content in the welding wire. At increase in mass fraction of nickel from 9 to 25 % the HAZ width is 3–5 % decreased, and if to increase the nickel to 40 % it decreases by 10–15 %. Along with that the metal structure is changed (Figure 3). The area of overheating in the near-weld zone during welding using the austenitic wire with 9 % Ni has a Widmanstatten ferrite without carbide precipitates, which is located inside

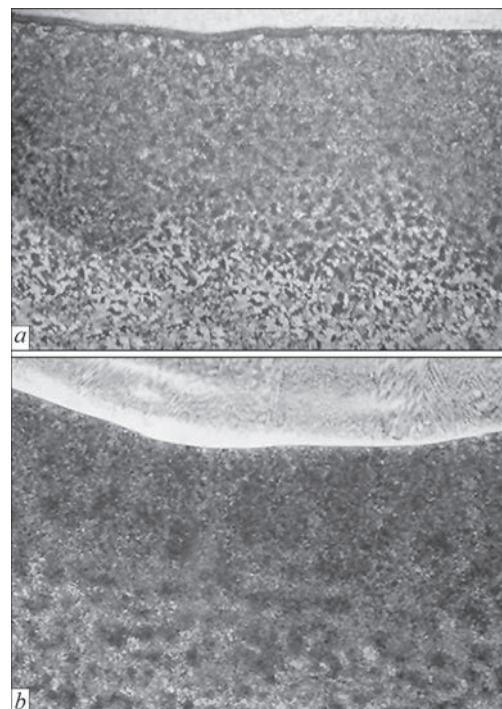


Figure 3. Microstructure ($\times 50$) of HAZ metal of steel 20 with the austenitic deposited metal of type 08Kh20N9G7T (*a*) and 08Kh25N40M7 (*b*) in as-welded state

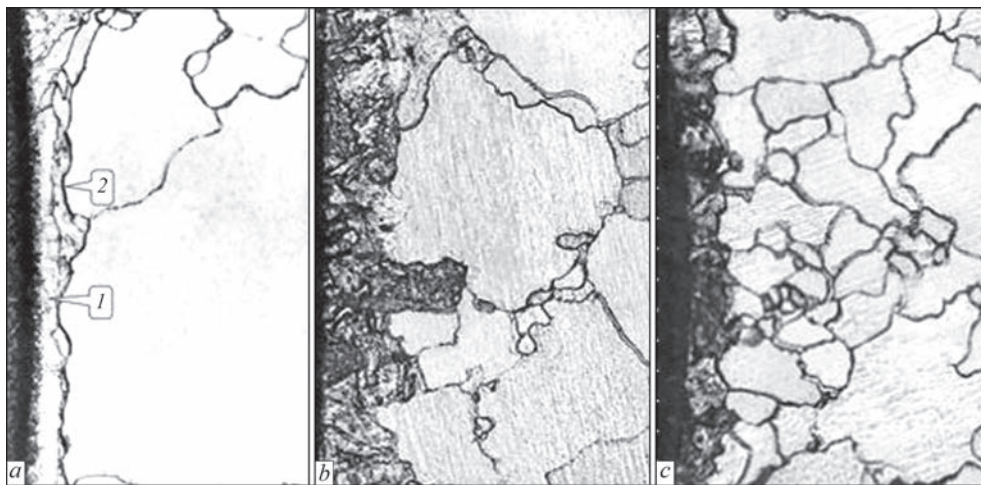


Figure 4. Microstructure ($\times 200$) of metal of the submelted area and ferritic interlayer in the HAZ of steel 20 with austenitic metal of type 08Kh20N9G7T deposited in Ar (*a*) and $\text{CO}_2 + \text{N}_2$ (*b, c*) at 7.9 (*a, b*) and 4.1 (*c*) kJ/cm heat input, 550 °C heating for 3000 h: 1 — submelted area; 2 — boundaries of ferrite grains adjacent to the submelting area

the austenite grains (Figure 3, *a*). During welding using the wire with 40 % Ni the overheating area has a bainite structure with the pearlite regions (Figure 3, *b*). It indicates the lesser degree of homogenization of austenite and the presence of carbides. To confirm this fact, the additional size of austenite grain was revealed at this region by metallographic etching in the water solution of picric acid with the addition of washing powder. It was found that the grain size is reduced from 3–4 to 5–6. To such a change in the value of grain size the change in the size of ferrite grains of a ferrite interlayer corresponds (Figure 4). The influence of increase in the nickel content on the change in the width of HAZ is explained [13] by decrease in the solidification temperature of the weld pool metal as well as the temperature and duration of heating the metal at the area of overheating.

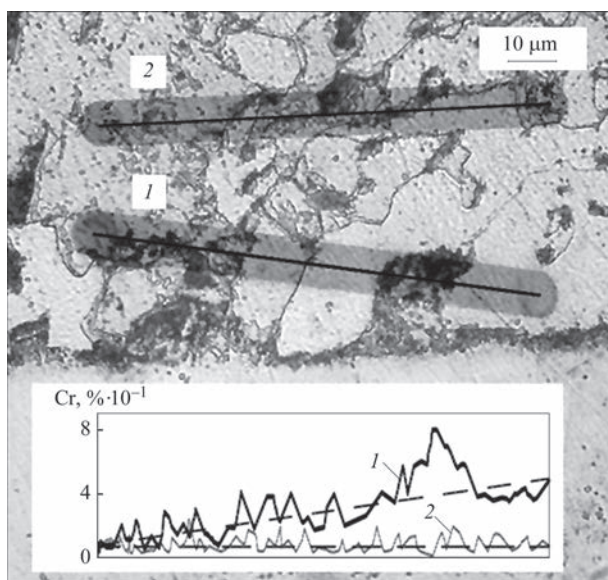


Figure 5. Distribution of chromium by traces 1 and 2 of microanalyzer probe in the near-weld zone of steel 20 with the austenitic deposited metal of 08Kh20N25M8G8 type

The alloying with nitrogen has a significant effect on the structure of submelting area of the near-weld zone, the sizes and shape of ferrite grains, especially those of the first series of the decarburized zone (see Figure 4).

The submelting area is revealed in the near-weld zone of all the investigated variants of surfacing in the form of an intermediate interlayer between the decarburized and carburized zones. The submelting of metal in that area is evidenced by the presence of alloying elements of a weld metal there, the content of which increases towards the fusion zone (Figure 5). The submelted area is contoured on the side of the decarburized zone by the boundaries of ferrite grains of the first series conjugated with it. Its thickness during surfacing at heat input of 7.9 kJ/cm in Ar equals to 0.02–0.1·10, in CO_2 — 0.07–0.10, in mixture of $\text{CO}_2 + \text{N}_2$ — 0.1·10–0.15 mm. The decrease in the heat input to 4.1 kJ/cm leads to reduction of its thickness to 0.05–0.1·10 mm.

The structure of the submelted area in the near-weld zone of deposit, performed in Ar, is ferrite, with narrow, fine grains elongated mainly along the fusion zone (see Figure 4, *b*). The linear X-ray spectral microanalysis shows a significant reduction of carbon in that area (highlighted by dash line in Figure 6, *a*), that evidences of its decarburization.

The ferrite grains of the first series are very large (2–3 according to GOST 5639–82). They were formed, apparently, due to collective recrystallization as a result of grains fusion at dissolution of low-resistant carbides in the conditions of decarbonization. The boundaries between these grains and the submelted area are mostly oriented along the fusion zone. These boundaries are intensively etched over the entire length during the metallographic etching and have a high carbon content (1.1–1.8 wt.%). Apparently, it

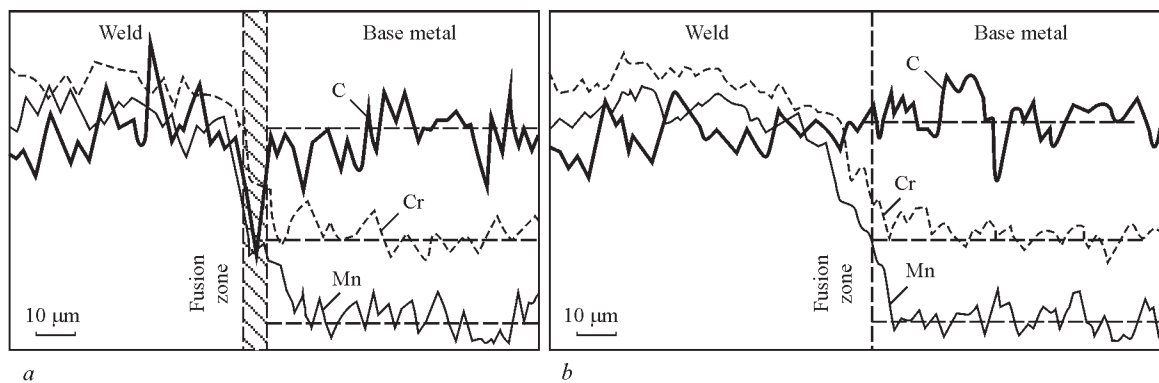


Figure 6. Distribution of carbon in fusion zone of welded joints of steel 15Kh5M with austenitic metal of 08Kh20N9G7T type deposited in Ar (a) and $\text{CO}_2 + \text{N}_2$ (b) at 550 °C heating for 3000 h

evidences of the film precipitation of the more alloyed carbides there. The hardness of metal of the submelted area near the ferrite grains is equal to $HV0.2-118$ and near the dark etched carburized zone it grows to $HV0.2-146$. At the carburized zone the hardness of metal is equal to $HV0.2-360-667$.

At the submelting area of the deposits performed in Ni_2 -containing shielding gas, as compared to those performed in Ar, the structure of tempering sorbite (the main field) with nitride particles and fine grains is formed instead of ferrite structure (see Figure 4, b). The hardness of metal with such a structure is higher, i.e. $HV0.2-160-180$, and that of ferrite grains adjacent to it is $HV0.2-120-146$. In the carburized zone the hardness of metal is decreased to $HV0.2-280-445$. At the distribution curve of carbon (see Figure 6, b), obtained by X-ray microanalysis, the carbon reduction in the submelting area is absent, at the same time, numerous small peaks were revealed there, formed, apparently, by carbonitrides. At the area of the transition layer of this curve the carbide peaks have a smaller height and width, which indicates a reduction in carbon content in the carbide particles and their more uniform distribution. In the decarburized interlayer the value of the first series ferrite grains, which are mated with the submelted area, decreased more than twice. Their boundaries are more disoriented relative-

ly to the fusion zone (see Figure 4, b) and are less etched. It indicates the fact that the process of decarburization and collective recrystallization gained lower propagation and the film carbide precipitates are absent at the boundaries. The disorientation of boundaries of the first series ferrite grains is also caused by their adjacency with the fine grains of the submelted area. The decrease in the density of carbides clustering at the boundaries is apparently caused by increase in the area of surfaces, where the carbon is concentrated, formed by dispersed grains and nitride particles.

When decreasing the welding heat input from 7.9 to 4.1 kJ/cm the structure of metal in the submelted area of the near-weld zone of all the investigated variants of surfacing remains unchanged, but the value of grains both in the submelted area as well as that of the first series ferrite grains of the decarburized interlayer becomes even smaller (see Figure 4, c).

The resistance of welded joints of dissimilar steels against thermal embrittlement was evaluated according to the procedure of work [14] by testing on static bending of specimens with artificial lack of penetration, which plays the role of a concentrator in the fusion zone. The welded joints of steel 20 with the weld metal of type 08Kh20N9G7T were tested produced in $\text{CO}_2 + 2\% \text{N}_2$ and with the weld metal of type 08Kh25N40M7 produced in Ar, in the state after

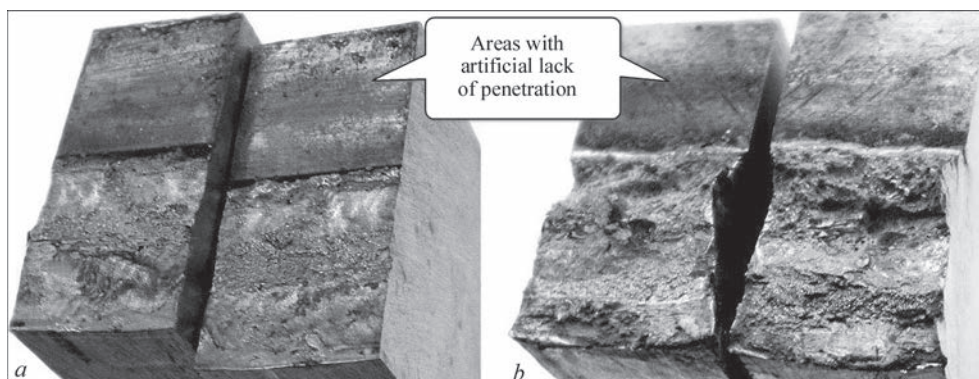


Figure 7. Fracture surfaces of specimens with artificial lack of penetration in the fusion zone of steel 20 joints with austenitic weld metal of 08Kh25N40M7 (a) and 08Kh20N9G7T (b) type produced in Ar and $\text{CO}_2 + 2\% \text{N}_2$, respectively, after testing on static bending

heating at 550 °C for 3000 h. The application of specimens with artificial lack of penetration allowed localizing the deformation during bending in the fusion zone. The specimens of welded joints, produced in Ni₂-containing gas withstand 1.5–2 times higher fracture load and have a greater bending angle (50–80°) than the specimens of welded joints, produced in Ar (5–15°). In the first variant of welded joint the fracture of specimens is tough and deviates from the fusion zone to the base metal, and in the second variant it is brittle (see Figure 7) over the carburized zone and the boundaries of ferrite grains of the first series, coupled with the submelted area of the fusion zone.

Conclusions

1. At a long high-temperature heating of joints of dissimilar steels with the austenitic weld, not alloyed with nitrogen, the film carbide precipitates are formed in the conditions of structural and phase instability between the fusion zone and the HAZ, which is one of the causes of brittle fracture.

2. The increase in nickel content in the austenitic weld and the reduction in welding heat input contribute to the decrease in the width of a ferrite interlayer in the HAZ of pearlite steel at high-temperature heating, but it does not prevent the formation of film carbide precipitation and metal embrittlement.

3. The decisive factor, influencing the reduction in the width of a ferrite interlayer of the increased nickel content in the austenitic weld and low welding heat input, is the reduction in metal overheating and degree of degradation of carbides in the HAZ.

4. During long high-temperature heating the austenitic weld metal alloying with nitrogen, the formation of nitride particles and grains refinement contribute to increase in the structure stability, inhibition of devel-

opment of carbide reactions and reduction in structural heterogeneity, as well as a more uniform distribution of carbides in the fusion zone with pearlite steel, that reduces the thermal embrittlement of welded joints of dissimilar steels.

1. Gotalsky, Yu.N. (1981) *Welding of dissimilar steels*. Kiev: Tekhnika.
2. Zemzin, V.N. (1966) *Welded joints of dissimilar steels*. Moscow: Mashinostroenie.
3. Livshits, L.S., Khakimov, A.N. (1989) *Metals science of welding and heat treatment of welded joints*. 2nd ed. Moscow: Mashinostroenie.
4. Kirilichev, N.V., Gotalsky, Yu.N. (1980) Peculiarity of structural heterogeneity in fusion zone of multilayer austenitic weld with pearlitic steel. *Avtomatich. Svarka*, **9**, 28–32.
5. Safonov, A.N., Radchenko, R.D., Chobanyan, V.A. (1993) Investigation of structural transformations in surface layers of low-alloy steel welded joints after laser treatment and subsequent heating. *Svarochn. Proizvodstvo*, **1**, 4–7.
6. Lipodaev, V.N., Snisar, V.V., Belchuk, M.V. et al. (1991) Specifics of brittle fracture of dissimilar welded joint with high-nickel weld metal. *Avtomatich. Svarka*, **10**, 6–9.
7. Snisar, V.V., Lipodaev, V.N., Elagin, V.P. et al. (1991) Effect of nitrogen alloying of austenitic weld on development of structural heterogeneity in fusion zone with pearlitic steel. *Ibid.*, **2**, 10–14.
8. Krishtal, M.A. (1972) *Diffusion mechanism in iron alloys*. Moscow: Metallurgiya.
9. Minkevich, A.K. (1968) *Chemical heat treatment*. Moscow: Mashinostroenie.
10. Lakhtin, Yu.M., Arzamasov, B.N. (1985) *Chemical heat treatment of metals: Manual for institutes of higher education*. Moscow: Metallurgiya.
11. Zhitnikov, N.P., Zaks, I.A. (1971) Effect of nitrogen on structure of austenitic weld metal. *Svarochn. Proizvodstvo*, **8**, 5–9.
12. Elagin, V.P., Snisar, V.V., Lipodaev, V.N. et al. (1995) Mechanized welding of 15Kh5M steel without heating and heat treatment. *Avtomatich. Svarka*, **8**, 19–23.
13. Makarov, E.L. (1981) *Cold cracks in welding of alloy steels*. Moscow: Mashinostroenie.
14. Bojkova, K.I., Chizhik, A.I., Zemzin, V.N. (1975) Method of evaluation of susceptibility to brittle fracture of welded joints on criteria of fracture mechanics. *Avtomatich. Svarka*, **2**, 14.

Received 15.05.2016

MICROSTRUCTURE AND WEAR-RESISTANT PROPERTIES OF WC/SS316L COMPOSITE COATINGS PREPARED BY SUPERSONIC LASER DEPOSITION

BO LI^{1,2}, ZHIHONG LI^{1,2}, LIJING YANG^{1,2} and JIANHUA YAO^{1,2}

¹Research Center of Laser Processing Technology and Engineering, Zhejiang University of Technology
18 Chaowang Str., 310014, Hangzhou, PRC. E-mail: libo1011@zjut.edu.cn

²Zhejiang Provincial Collaborative Innovation Center of High-end Laser Manufacturing Equipment
18 Chaowang Str., 310014, Hangzhou, PRC. E-mail: laser@zjut.edu.cn

Supersonic laser deposition (SLD) is a newly developed coating method which combines the supersonic powder jet found in cold spray (CS) with synchronous laser heating of the deposition zone. The addition of laser heat energy into CS enables a change in the thermodynamic state of impacting particles and substrate, thereby significantly lowering the critical deposition velocities required for effective coating formation and allowing the range of materials deposited to expand to higher strength materials which are of considerable engineering interest. This paper presents the ability of SLD technique to deposit hard metal matrix composite (MMC) coatings, such as WC/SS316L. The focus of this research is on the comparison between composite coatings produced with conventional CS and those produced with SLD. The microstructure evolution, mechanical deformation mechanisms, correlation between functional properties and process parameters were elaborated in detail. The experimental results show that with the assistance of laser irradiation, WC/SS316L composite coatings can be successfully deposited using SLD. The obtained coatings are superior to that processed with CS, because SLD can improve the deposition efficiency, coating density, interface bonding as compared to CS due to the softening of particle and substrate by laser irradiation. It can be found that SLD is capable of depositing high strength MMC coatings with good quality, thus exhibiting great potential in the field of metal 3D printing. 13 Ref., 1 Table, 8 Figures.

Keywords: *supersonic laser deposition, metal matrix composite coating, microstructure, composition, wear-resistant property*

Cold spray (CS) is a rapidly emerging coating technology, in which small powder particles in a solid state are deposited on a substrate via high-velocity impact at temperatures lower than the melting point of the powder material [1–3]. In the CS process, small powder particles (5–50 μm) are accelerated to a high velocity in a supersonic gas jet and then imping onto the substrate or already deposited coating to build up a coating. The main advantage of CS is the lower heat input as compared to traditional high-temperature coating methods such as thermal spray and laser cladding. Only thermal input in CS is optional gas heating, which can be used to increase the local speed of sound of the process gas, and its positive drag force on particles. As a consequence, the deleterious effects of high-temperature oxidation, evaporation, melting, crystallization, residual stress, debonding, gas release, and other common problems for traditional thermal spray and laser cladding methods are minimized or eliminated.

Eliminating the adverse effects of high-temperature on coatings and substrates offers significant advantages and new possibilities, and makes CS promising for many industrial applications. However, to achieve the high particle velocities that CS requires for successful deposition, helium is often used as the process gas, which is an expensive, limited resource. Moreover, a gas heater is often employed to heat the process gas as high as 900 °C to increase gas and particle velocity. The need for hot helium gas results in high operating costs arising from the power consumption for heating the gas and the high price of the gas itself. Additionally, it is challenging to deposit hard material coatings with high bonding strength and coating density solely using CS.

It has become clear that there would be distinct advantages in developing a process that could retain the non-melting deposition mechanism of CS, but reduce deposition costs and improve coating functionality. Such a process, known as supersonic laser deposition

¹Based on materials presented at Seventh International Conference «Laser technologies in welding and materials processing», September 14–18, 2015, Odessa, Ukraine.

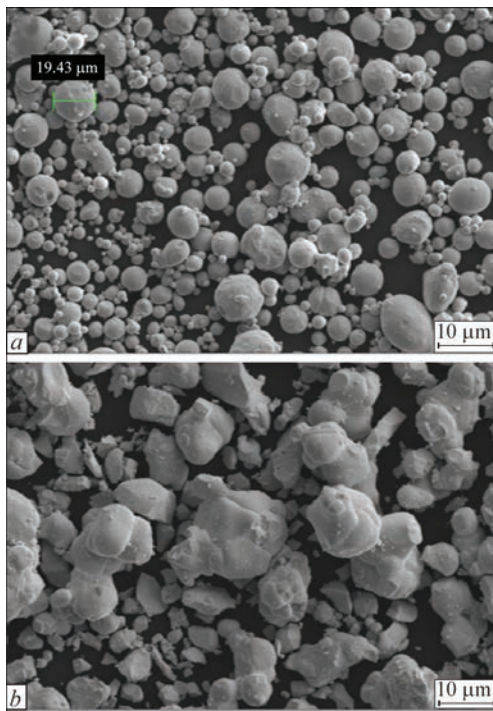


Figure 1. Microscopic images of feedstock materials: *a* — SS316L; *b* — WC

(SLD), has been proposed by O'Neill et al. which combine CS with laser heating [4–6]. In SLD, a laser is employed to heat the deposition zone of CS in order to soften both substrate and powder particles, allowing the particles to deform and build up a coating at impact velocities around half of that in CS. Eliminating the need for high impacting velocities permits cold or slightly heated nitrogen to be used instead of high-temperature helium as the process gas, thus reducing operating costs by over an order of magnitude. Furthermore, the SLD technique greatly expands the material range of particle and substrate which can be processed due to the reduction of critical deposition velocity. SLD has been applied to fabricate a variety of material coatings such as copper, titanium, Stellite 6, Ni60, Al–Cu, Al–Si alloys and so on [7–12].

Metal matrix composites (MMCs), which are generally composed of a hard reinforcing non-metallic material and a metallic matrix, are a useful class of materials for surface coating that enable physical properties such as density and thermal/electrical conductivity to be tailored, along with mechanical properties such as strength and wear resistance. Currently, laser cladding, thermal spray and CS are the most widely used methods for preparing MMC coatings. The high-temperature involved in laser cladding and thermal spray would lead to porosity, microcrack formation, dilution, phase transformation, high thermal stress, etc. The main problem for cold-sprayed MMC coatings is the bonding strength, because the metallic matrix is often soft materials such as Al, Cu, Ni,

which results in weak holding force between the metallic matrixes and reinforcing particles. As a result, the reinforcing particles are prone to spall off from the coating in the subsequent real applications, which would degrade the coating's performance.

Based on the characteristics of SLD, it is expected to deposit hard material coatings by this process at a lower impact velocity with high coating density and strong interfacial bonding. Meanwhile, the deleterious effects of high-temperature coating methods could be effectively avoided due to the relatively low-temperature deposition feature of SLD. Currently, most of the research reported in literature about SLD technique focused on single material coatings and seldom involved MMC coatings. Therefore, in this study, the SLD process was adopted to deposit tungsten carbide reinforced stainless steel (WC/SS316L) composite coatings onto carbon steel substrate in order to demonstrate the feasibility of SLD technique to prepare hard metallic matrix composite coatings. For comparison, the cold-sprayed composite coatings were also produced under the same conditions except that laser heating was not involved. The microstructure, composition, interface bonding, coating density and wear-resistant properties of the as-deposited composite coatings were investigated using scanning electron microscopy (SEM), optical microscopy (OM), X-ray diffraction (XRD) and pin-on-disc wear tester.

Experimental section. *Feedstock materials.* Commercially available stainless steel (SS316L) powder and tungsten carbide (WC) powder were used in the as-received conditions as feedstock materials. The particles' shapes of SS316L and WC powder are spherical and irregular (Figure 1). The composite powder consisting of 30 vol.% WC and 70 vol.% SS316L was mechanically milled in a cylinder rotating at speed of 200 rpm for 2 h. The ball milling process was used to obtain evenly mixed composite powder, which would be beneficial for depositing composite coatings with uniformly distributed reinforcing particles. The substrate material was carbon steel and the substrate specimens had dimension of 100×60×10 mm. Before the coating process, the substrate surface was grit-blasted using 24 mesh alumina and ultrasonic cleaned in alcohol.

SLD system and coating process. The schematic diagram of the SLD system used in this study is illustrated in Figure 2, *a*. High-pressure gas was supplied to a converging-diverging nozzle in two different imports: one was through the gas heater; the other was via a powder feeder where feedstock powders were held. The feedstock powder stream and high-pressure gas were mixed and passed through the nozzle

where the particles were accelerated to supersonic speed. The high-velocity particles impacted a region of the substrate which was synchronously heated by diode laser (Laserline LDF 400-1000, Germany) with 960–980 nm wavelengths and 4 kW maximum power. Combined lenses were used to focus the laser beam onto the substrate surface, and the diameter of the laser spot was 5 mm. A high-speed infrared pyrometer was used to obtain real-time temperature measurements and control the temperature of the deposition zone (referring to as «deposition temperature» hereafter) during the SLD process. Data from the pyrometer was fed through a closed-loop feedback system which altered laser power as necessary to maintain the desired temperature. The nozzle, laser head and pyrometer were assembled on robot (STAÜBLI TX 90, Switzerland). The spraying nozzle was perpendicular to the substrate surface. The laser beam was at angle of 30° to the surface normal. The laser energy and powder distribution are schematically illustrated in Figure 2, *b*. In the deposition process, the substrate was stationary and the nozzle, laser head and pyrometer were moveable, controlled by the robot. The process gas was nitrogen. The process parameters for WC/SS316L composite coatings except deposition temperature were kept constant at the optimal values: gas pressure 2.5 MPa; gas temperature 400 °C; laser traverse speed 30 mm/s; powder feeding rate 40 g/min; spray distance 30 mm.

Coating characterization. The coating specimens were cross-sectioned perpendicular to the coating surface with electric discharge wire cutting, followed by conventional metallography preparation procedures. An aqueous solution, consisting of 45 ml of HCl, 15 ml of HNO₃ and 20 ml of methanol, was used for etching. A field emission scanning electron microscopy (SIGMA HV-01-043, Carl Zeiss) and optical microscopy (Axio Scope, A1, Zeiss) were used to analyse the coating's microstructure and interface bonding. Backscatter SEM images were taken to maximize contrast between the WC particles and stainless steel matrix. The phase of the composite coatings were investigated using X-ray diffractometer (D8 Advance, Bruker) with CuK_α radiation, at 45 kV, 40 mA, scanning rate of 0.02 deg/s. Pin-on-disc wear test was conducted on the composite coatings at room temperature under a dry-lubricating condition. The pin was 4 mm diameter Si₃N₄ ceramic ball, having the hardness of HV 2200 (HRC 90). The disc was the tested specimen which was polished, cleaned in a ultrasonic bath, and finally dried. The test was performed under normal load of 500 g at rotational speed of 500 rpm of the tested specimen between the contacting surfaces; sliding duration was 60 min.

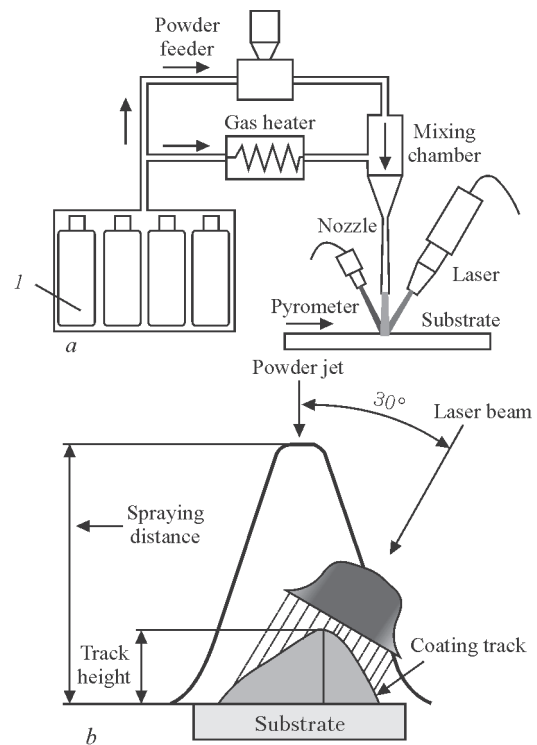


Figure 2. Schematic illustration of SLD system (*a*), laser energy and powder distribution in the SLD process (*b*)

Results and discussion. *Deposition efficiency.* The deposition efficiencies (DE) of the WC/SS316L composite coatings deposited at different deposition temperature were compared with respect to coating layer thickness. Shown in Figure 3 are the OM images of cross section of the coating specimens. As can be seen, the central peak heights of the as-deposited coatings are gradually increased with elevating the deposition temperature. The peak height of the WC/SS316L coating deposited without laser assistance is 734.04 μm while it is increased by 43 % to 1050.91 μm as $T_d = 800$ °C was employed, indicating that DE can be improved with increasing the deposition temperature.

The improvement of DE should be ascribed to the reduction of critical deposition velocity due to the softening of spraying particles by laser irradiation. One of the most important parameter in the CS process is the critical deposition velocity. For a given material, there exists a critical deposition velocity that must be achieved. Only particles, velocities of which exceed this value, can be effectively deposited, in turn producing the desired coating. Conversely, particles that have not reached this threshold velocity contribute to the erosion of the substrate. Theoretical modelling of critical deposition velocity (m/s) proposed by Assadi et al. can be expressed as [13]:

$$v_{cr} = 667 - 14\rho + 0.08T_m + 0.1\sigma_t - 0.4T_s, \quad (1)$$

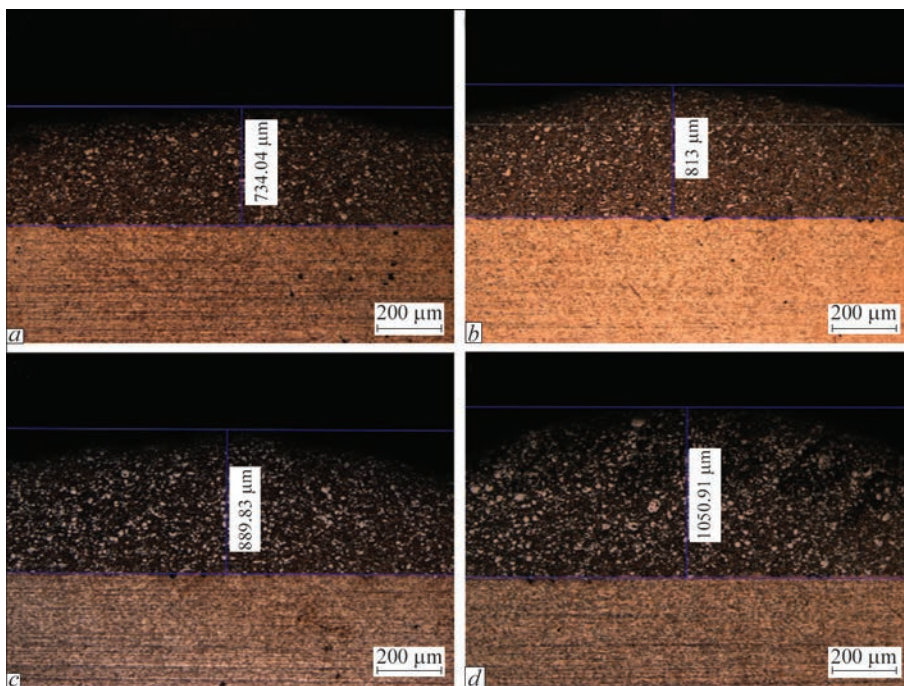


Figure 3. Coating thickness prepared at different deposition temperature: *a* — ambient temperature; *b* — $T_d = 400$; *c* — 600; *d* — 800 °C

where ρ is the density of the material, g/cm^3 ; T_m is the melting temperature, °C; σ_t is the ultimate strength, MPa; T_i is the initial particle temperature, °C. According to formula (1), particle preheating will decrease the critical deposition velocity because as T_i is increased, σ_t is reduced. Both the increase of T_i and the reduction of σ_t would contribute to the decrease of v_{cr} .

In this study, the spraying nozzle was perpendicular to the substrate surface and laser beam was at angle of 30° to the surface normal (see Figure 2, *b*). The powder jet and laser beam partially overlapped with each other. Although the spraying particles were travelling at high velocities and had limited time of exposure to the laser, it is expected that the particles would be significantly heated in flight by laser prior to hitting the substrate because of the high laser power density and small particle size, which could bring down the critical deposition velocity of spraying particles. As a consequence, the proportion of particles exceeding this velocity would increase, leading to the improvement in DE (see Figure 3).

Distribution and content of reinforcing particles in the composite coatings. It can be seen that WC particles are evenly distributed in all the coating specimens. Therefore, we randomly selected one area in each coating and calculated the WC area fraction in these selected areas using image analysis software to evaluate the dependence of WC content on deposition temperature. The calculated results are illustrated in Figure 4. It is shown that the area fraction of WC particles in the CS coating is about 22.55 % and it increases slightly to 24.42 % when $T_d = 400$ °C is adopted.

As the deposition temperature is further increased to 600 °C, the area fraction of WC particles increases greatly to 28.55 %. The coating deposited at 800 °C has about 29.29 % area fraction of WC particles, which is very close to the volume fraction (30 %) of WC particles in the original composite powder. This indicates that laser heating benefits the effective deposition of WC particles in the composite coatings.

Cold-sprayed MMC coatings generally consist of pure metallic matrix and ceramic reinforcing particles, such as Al/AlN, Ni/Al₂O₃, Cu/Al₂O₃ etc. During the CS process, the reinforcing particles cannot deform due to high hardness and they need to be embedded in the deformable metallic matrix to form composite coating. Therefore, the plastic deformation ability of metallic matrix plays a decisive role in the formation of MMC coatings. In this study, without laser assistance or with less laser heating, the SS316L powder wasn't softened enough to accommodate the hard particles, resulting in relatively low WC content. In the case of more laser heating, the SS316L powder easily deformed to take in WC particles owing to sufficient softening, resulting in higher WC particle concentration (see Figure 4).

Coating density. According to the previous results, it can be found that the composite coating deposited at 800 °C has relatively high DE and WC content. Therefore, the following comparative studies mainly focus on this sample and CS sample. Shown in Figure 5 is the comparison of coating density between these two samples. It can be seen from Figure 5, *a* that there are lots of gaps and pores in the CS coating,

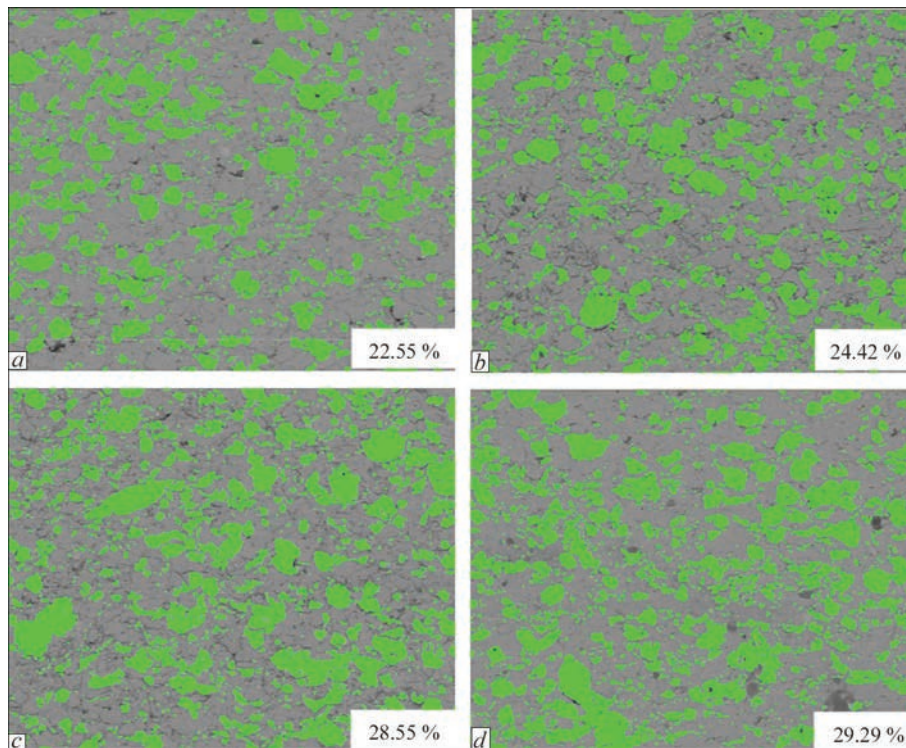


Figure 4. WC distribution and content in as-deposited coatings at different deposition temperatures: *a* — ambient temperature; *b* — $T_d = 400$; *c* — 600; *d* — 800 °C

which indicates poor bonding strength between powder particles and low density of this coating. Moreover, evident holes can also be clearly observed in the CS coating (see Figure 5, *a*). The appearance of these holes arises from the debonding of the fractured WC particles. With the assistance of laser heating, improved coating density can be obtained for the as-deposited coating. Gaps and pores are hardly observed in the SLD coating, along with the disappearance of the holes. These results imply that laser irradiation has beneficial effects on the coating density. Bray et al. [4] compared the porosity of titanium coating prepared by CS, high-velocity oxygen fuel spray (HVOF) and SLD respectively. Their results revealed that the porosity level of the CS and HVOF coatings were 3.1 and 5.4 % respectively, while that of the SLD coating was only about 0.5 %, suggesting that the coating density of SLD coating is superior to that of CS and HVOF ones.

The poor density of CS coating are mainly attributed to the limited plastic deformation of the spraying particles. In the SLD process, the synchronous laser irradiation can effectively soften the spraying particles which would in turn result in sufficient deformation of spraying particles. The sufficiently deformed particles would interlock with each other to form intimate contact, thus showing high coating density. Furthermore, due to the softening of the metallic matrix, hard WC particles wouldn't fracture and spall off from the composite coating as embedding into the

metallic matrix, which ensures no holes formed in the SLD coating.

Phase analysis. The influence of laser heating on phases of the WC/SS316L composite coatings was analysed using XRD. The XRD results for the composite CS and SLD coatings are presented in Figure 6. It is found that the coating specimens with and

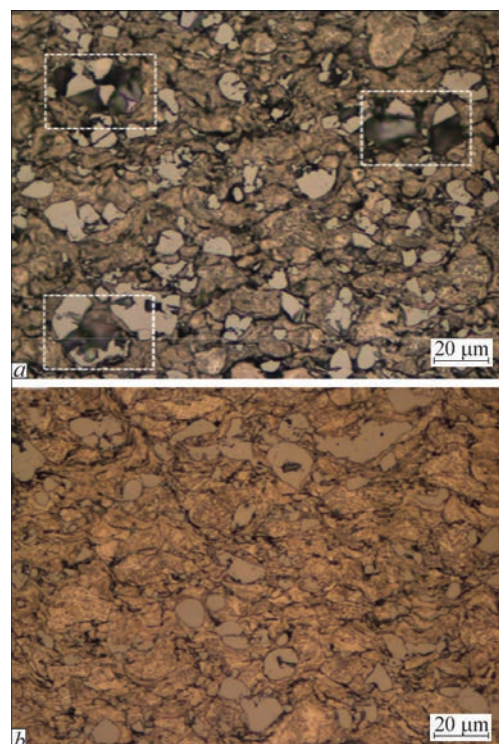


Figure 5. Density of coating prepared by CS (*a*) and SLD (*b*)

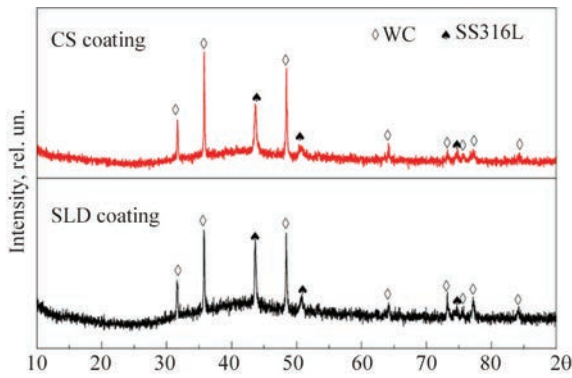


Figure 6. XRD patterns of the CS and SLD composite coatings without laser irradiation have identical phases that are composed of SS316L and WC, implying that SLD still remains solid state deposition mechanism as CS does although laser heating is introduced in this process. In SLD process, the laser power is elaborately controlled to only soften both the spraying particles and the substrate, not melting them. The particles remained solid during flight and deposition and were subject to laser irradiation for only a limited period of time. Thus, the chemical composition and phases did not transform in the SLD coatings as compared to the CS coating, even for the low melting temperature materials such as copper and aluminum. It was found in our previous study [9] that the oxidation of SLD-Cu coating was trivial and can be neglected with comparison to the CS-Cu coating. The relatively low temperature deposition feature of SLD can effectively avoid high thermal stress, oxidation, phase transformation and grain growth in the as-deposited coatings, making it a superior coating technology over thermal spray and laser cladding.

Wear-resistant performance. The evolution of friction coefficient of the test samples were recorded during the wear processes, and the variations of friction coefficient with sliding time are plotted in Figure 7. It is shown that the friction coefficient of the SLD sample is smaller and more stable than that of the CS sample. The average friction coefficient of the

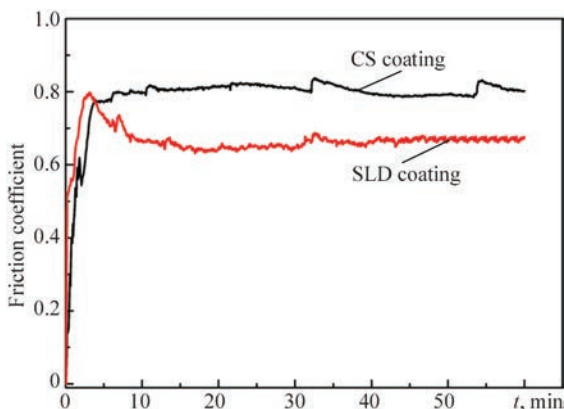


Figure 7. Variations of friction coefficient with sliding time of WC/SS316L composite coatings prepared by CS and SLD

EDS results of worn surfaces of the WC/SS316L composite coatings prepared by CS and SLD

Area number	O	Si	Cr	Fe	Ni	W
1	11.68	1.49	12.95	57.05	7.76	9.07
2	39.38	8.76	5.87	24.55	3.53	17.91
3	7.32	3.63	3.71	12.8	2.50	70.04
4	36.36	10.65	5.44	23.42	4.27	19.86

SLD sample is around 0.65 after 60 min sliding, while that of the CS specimen is about 0.8 at the same time.

To further investigate the wear-resistant performance of the WC/SS316L composite coatings, the worn surfaces of the tested samples were examined using SEM, the results are shown in Figure 8. It can be seen that in both the worn surfaces, there are two distinct areas, dark and light. The dark area is more extensive in the CS coating than in the SLD coating. The Table are the EDS results of the dark and light areas in the wear track of CS and SLD coatings. It is shown that the dark areas (2 and 4) contain a high content of oxygen; in contrast, a lower oxygen content is detected in the light areas (1 and 3). This suggests that oxidation had occurred in the worn track when the coating samples were under the sliding wear tests, and the dark areas were oxidation scales formed during the wear tests. The more oxidation scales in the worn surface of the CS coating indicate, more friction heat was generated in its surface during wear, which

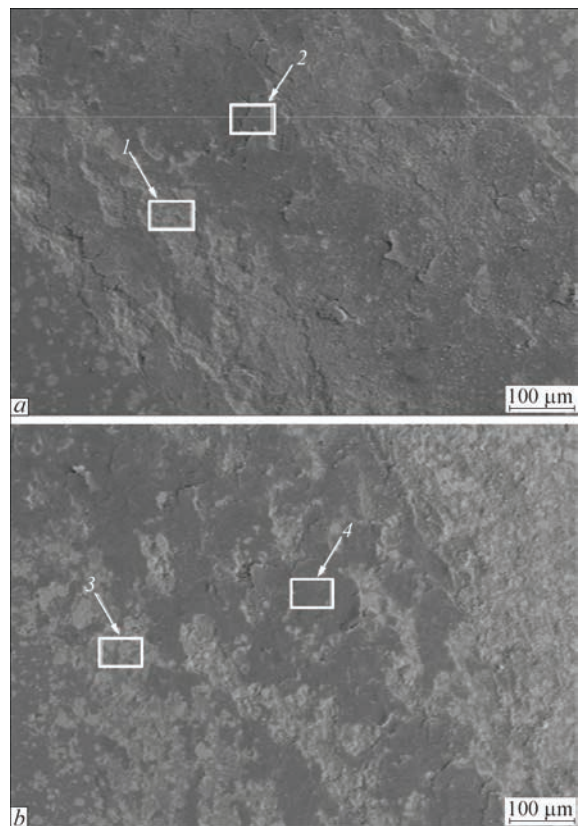


Figure 8. SEM images of worn surfaces of the WC/SS316L composite coatings prepared by CS (a) and SLD (b)

should be ascribed to the relatively high friction coefficient (see Figure 7).

It can be summarized from the wear test results that the WC/SS316L composite coating produced by SLD has better wear-resistant performance than the CS coating. It is believed that the friction between the contact surfaces was reduced due to the abrasion resistance of hard irregular WC particles. The better wear-resistant properties of the WC/SS316L coating produced by SLD are resulted from the relatively high content of WC particles in the composite coating and the strong interfacial bonding between the WC particles and SS316L matrix due to the beneficial effects of laser irradiation.

Conclusion

The WC/SS316L composite coatings on carbon steel are successfully prepared in a range of deposition temperatures with the SLD technique, which combines cold spray with laser irradiation. The deposition efficiencies of the SLD coatings are increased with elevating the deposition temperature due to the reduction of critical deposition velocity which results from the softening of spraying particles by laser heating. The WC content and interfacial bonding strength of the coatings are also improved with increasing the deposition temperature, which would in turn significantly improve the wear-resistant performance of the SLD coating. The introduction of laser irradiation into CS doesn't induce phase transformation in the SLD process due to the relatively low temperature deposition feature.

Acknowledgements. *The authors would like to appreciate financial supports from the National Natural Science Foundation of China (51475429), the Zhejiang Provincial Commonweal Technology Applied*

Research Project (2014C31122) and the Postdoctoral Scientific Research Project of Zhejiang Province (Z42102002).

1. Papyrin, A., Kosarev, V., Klinkov, S. et al. (2007) *Cold spray technology*, 1–32. Elsevier.
2. Champagne, V.K. (2007) *The cold spray materials deposition process. Fundamentals and applications*, 11–41. Woodhead Publ.
3. Maev, R.G., Leshchynsky, V. (2008) *Introduction to low pressure gas dynamic spray*, 1–10. Wiley-VCH.
4. Bray, M., Cockburn, A., O'Neill, W. (2011) The laser-assisted cold spray process and deposit characterization. *Surface and Coating Techn.*, **203**, 2851–2857.
5. Lupoi, R., Sparkes, M., Cockburn, A. et al. (2011) High speed titanium coating by supersonic laser deposition. *Materials Letter*, **65**, 3205–3207.
6. Jones, M., Cockburn, A., Lupoi, R. et al. (2014) Solid-state manufacturing of tungsten deposits onto molybdenum substrates with supersonic laser deposition. *Ibid.*, **134**, 295–297.
7. Olakanmi, E.O., Doyoyo, M. (2014) Laser assisted cold-spray corrosion- and wear-resistant coatings: A review. *J. Thermal Spray Techn.*, **23**, 765–785.
8. Tlotleng, M., Akinlabi, E., Shukla, M. et al. (2015) Microstructural and mechanical evaluation of laser-assisted cold sprayed bio-ceramic coatings: Potential use for biomedical applications. *Ibid.*, **24**, 423–435.
9. Li, B., Yang, L.J., Li, Z.H. et al. (2015) Beneficial effects of synchronous laser irradiation on the characteristics of cold-sprayed copper coatings. *Ibid.*, **24**, 836–847.
10. Yao, J.H., Yang, L.J., Li, B. et al. (2015) Beneficial effects of laser irradiation on the deposition process of diamond/Ni60 composite coating with cold spray. *Appl. Surface Sci.*, **330**, 300–308.
11. Luo, F., Cockburn, A., Cai, D.B. et al. (2015) Simulation analysis of Stellite 6 particle impact on steel substrate in supersonic laser deposition process. *J. Thermal Spray Techn.*, **24**, 378–393.
12. Luo, F., Cockburn, A., Lupoi, R. et al. (2012) Performance comparison of Stellite 6 deposited on steel using supersonic laser deposition and laser cladding. *Surface and Coatings Techn.*, **212**, 119–127.
13. Assadi, H., Gartner, F., Stoltenhoff, H. et al. (2004) Bonding mechanism in cold gas spray. *Acta Materialia*, **51**, 4379–4394.

Received 06.12.2015

ELECTROSLAG WELDING OF LARGE-SIZED PRESS FRAME

K.P. SHAPOVALOV¹, V.A. BELINSKY¹, A.E. MERZLYAKOV¹, S.N. KOSINOV¹,
K.A. YUSHCHENKO², I.I. LYCHKO² and S.M. KOZULIN²

¹Company «Novo-Kramatorsk Machine-Building Works»

5 Ordzhonikidze Str., 847305, Kramatorsk, Ukraine. E-mail: ztm@nkmz.donetsk.ua

²E.O. Paton Electric Welding Institute, NASU

11 Kazimir Malevich Str., 03680, Kiev, Ukraine. E-mail: office@paton.kiev.ua

The first in the world practice experience of production of the welded-forged structure of the lower frame of 70/90 MN forging press with thickness of welded butts in the range of 3000–3800 mm was described. The total weight of the structure amounted to 160–200 t. During manufacture the technology of electroslag welding using consumable nozzle was used. The role of the fixture belonged to the closed box-like shape of the welded billets themselves with stiffeners. The welded billet was subjected to normalizing with tempering and ultrasonic testing. The gained experience in producing welds of super-large cross sections can be used in development of methods for calculation of expected deformations and technical procedures of their control. 8 Ref., 4 Figures.

Keywords: *electroslag welding, press-forging equipment, welded-forged structure, press lower frames, super-large cross sections, specifics of production*

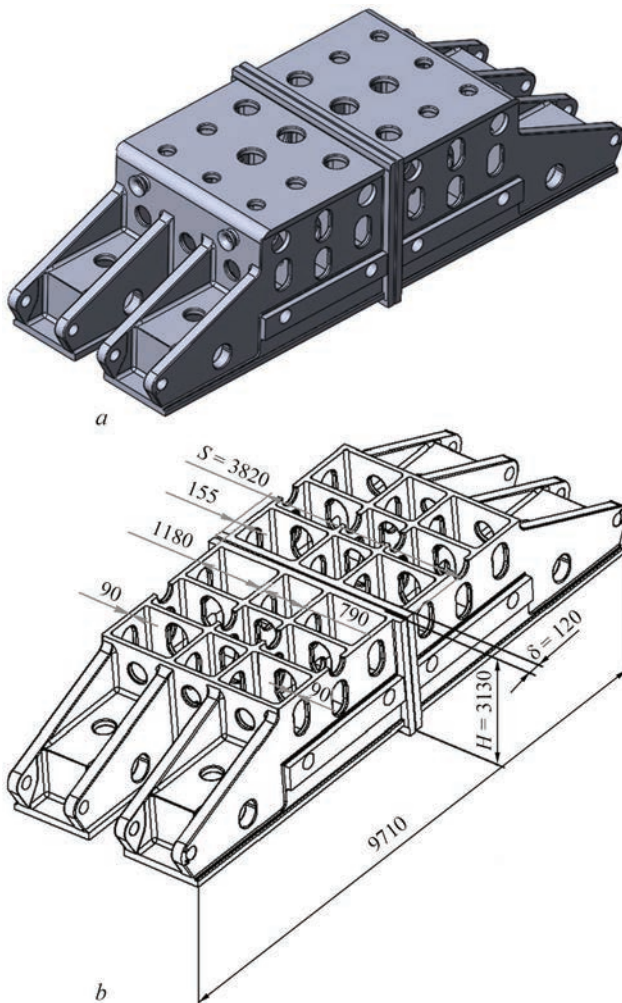


Figure 1. General view (a) and schematic diagram (b) of middle part of frame of forging hydraulic press with force of 70/90 MN

Over more than 60 years the Novo-Kramatorsk Machine-Building Works (NKMZ Company) produces different press-forging equipment, where almost all the load-carrying elements are produced in welded-cast or welded-forged variants applying electroslag welding (ESW). During that period more than 300 units of powerful press-forging machines were manufactured and delivered, which today are successfully operated in more than 20 countries around the world. At present the production of forging hydraulic presses with the force of more than 30 MN is an important challenging direction of the heavy engineering.

One of the basic elements of such presses is a lower frame, the middle beam of which (Figure 1, a) is manufactured of steel 30L in the welded-cast variant (total weight is 160–200 t, thickness of butts being welded is within the ranges of $S = 3000\text{--}3800$ mm). Thus, for example, the middle beam of the lower frame of the forging press with force of 70/90 MN represents a three-dimensional box-type structure of 200 t consisting of two cast billets, joined using electroslag welding with consumable nozzle (ESW CN). The cross section of the welded butt ($S \times H$) has dimensions of 3820×3130 mm (Figure 1, b).

It should be noted that until now in the world practice of welding production the examples of welding of steel billets of such a cross section of the weld were not known. Furthermore, the structure of the middle beam differs from the typically widespread massive billets with a large thickness of the weld so

that the wall thickness of edges being welded is only $\delta = 120$ mm (see Figure 1, *b*).

For ESW CN of rigid billets (the width of welded elements δ is not smaller than the weld thickness S), the value and character of the expected displacements of the edges being welded along the length of the weld H and the change in value of welding gap above the slag pool can be predicted with a fair degree of accuracy [1, 2]. The conditions of ESW CN of flexible plates, where the ratio of weld thickness to width of the plate is larger than one ($S/\delta > 1$), were almost not investigated. Therefore, it is rather difficult to determine the conditions of fixing (assembly) of parts being welded, which provide the expected value, and the nature of welding deformations within the permissible limits as well as the gap value throughout the whole welding process.

The analysis of temperature-time conditions of heat energy spreading and weld formation in ESW of large-thickness metal [3, 4] shows that during welding of relatively thin plates it is impossible to determine the nature of displacement of edges being welded in the course of producing weld beforehand. Here either the excessive decrease in the gap is possible which may cause a short-circuiting between the edges and consumable nozzles, or, vice versa, the increase in the gap value at which the edges can come out beyond the limits of forming devices. The both are inadmissible as far as it will result in interruption of the welding process. The nature of influence of mode parameters

and methods of external influence on welded edges, which could provide the gap value and geometrical parameters of flexible plates within the acceptable limits, are also unknown. To limit the movement of edges being welded in arc welding all kinds of devices (jigs, cramps, etc.) are often used. Because of large dimensions of billets, significant masses and volumes of the simultaneously crystallized weld metal as well as small width of welded edges, it is practically impossible to use these methods in the case of ESW.

In ESW CN of the middle beam of the lower frame the role of the jig (fixture) belonged to a closed box-like shape of the welded billets themselves, where the stiffeners located perpendicularly to the plane of the welded edges (see Figure 1, *b*) prevent change in the gap size if it is higher than the permissible limits over the butt height. Regarding the shape of the gap across the weld thickness in the intervals between the stiffeners, at the level of maximum penetration some buckling of welded edges can be expected. However their value should be negligible due to a relatively slow heating of edges metal across the whole thickness to 500–600 °C (thermoplastic state) and due to the effect of crystallizing weld, moving behind the zone of maximum heating of edges at distance of 15–30 mm at the speed of welding.

The technology and methods for assembly of massive billets of large dimensions and thickness of edges being welded, typically applied at the plant for ESW CN, include the following operations: assembly of

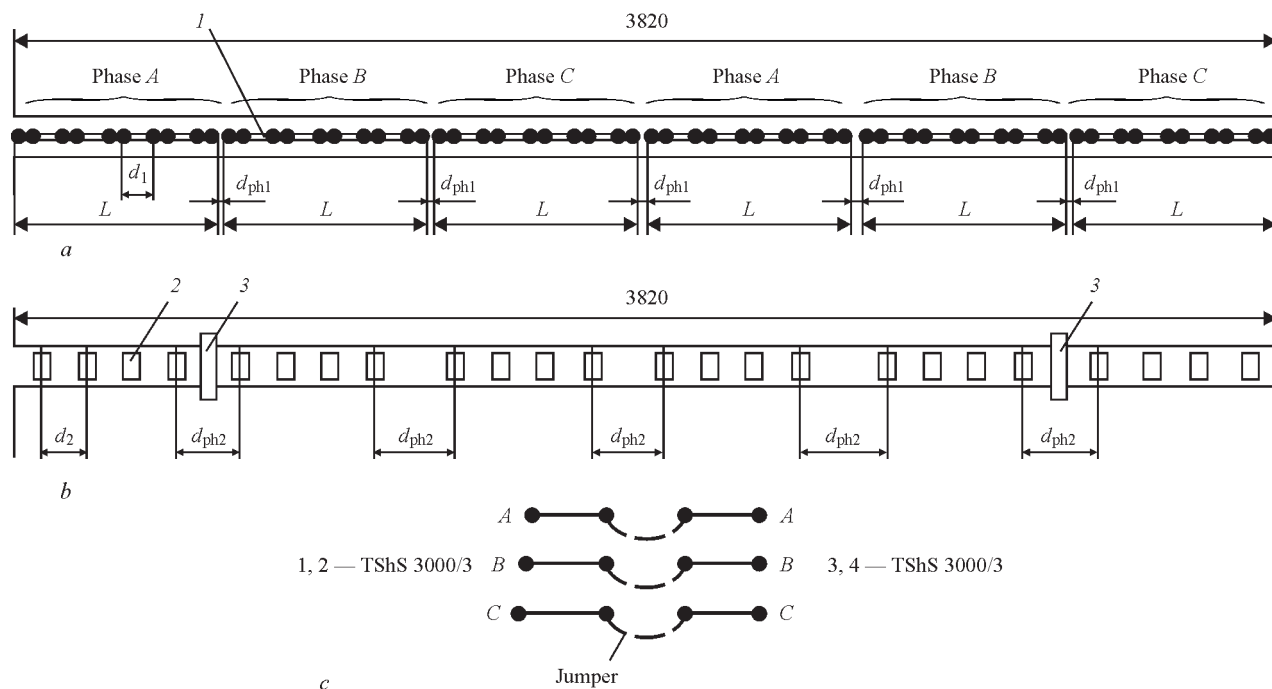


Figure 2. Schemes of mounting the nozzle plates in gap (*a*), cramps for mounting the consumable nozzles (*b*) and joining the phases for four power sources (*c*): 1 — section of consumable nozzle; 2 — cramps for sections fastening; 3 — cramp-jumper; L — width of one section (phase) of consumable nozzle; d_1 — distance between the axes of channels guiding; d_{ph1} — distance (interphase) between the consumable nozzles; d_2 — distance between the cramps for sections fastening; d_{ph2} — interphase distance for cramps



Figure 3. ESW of middle part of the frame (*a*) and heating of run-out straps in a few minutes before termination of welding process (*b*): 1 — billet; 2, 3 — heating of back side of the edges at places corresponding to groups of nozzles and interphase gaps; 4 — consumable nozzles

welded billets between each other at a definite assembly gap, which is fixed by assembly straps [5]; placing the installation for ESW with a consumable nozzle, assembled for welding billet, to the pit-type stand [6]; running of the installation on the assembled part; wheeling out of the trolley with welding machines to the extreme position; placing of consumable nozzles attached in the clamps of machine ASh-110 into the gap one after another. Further the preparatory works

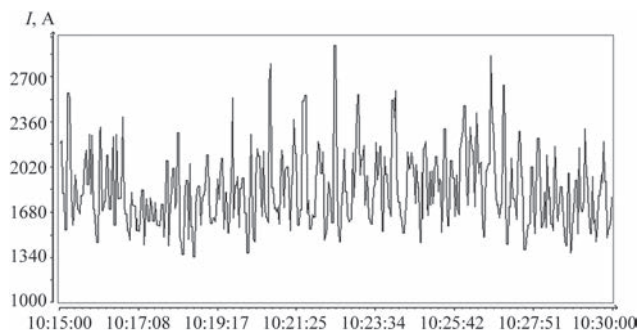


Figure 4. Oscillogram of welding current (process duration of 15 min, phase A, transformers 1, 2 (see Figure 2, c)

are carried out: alignment of nozzles in the gap, running of wire in the tubes of nozzles, etc.

Due to the large dimensions of the structure of the middle beam of the lower frame the technology of its assembly differed from the standard one. Initially one half of the beam was placed to the pit stand. The cramps are welded-on to the initial straps of the billet and the plate of rolled steel is placed on them, forming the «bottom of the pocket». Then, the installation runs over the fixed billet and the consumable nozzles are fastened to the clamps of the welding machines ASh-110: 24 plates of consumable nozzles, divided into 6 groups of 4 plates each (Figure 2). After mounting of all the nozzles, their position was fixed relatively to the billet by means of welded-on cramps for sections fastening (Figure 2, *b*, pos. 2) and then the plates were released from clamps of welding machines. To setting the second half of the middle beam of the lower frame the installation is moved to the extreme position. The assembly gap is formed as follows: 36 mm at the bottom and 40 mm at the top of the butt. After assembly of the parts to be welded with the specified gap, the «bottom of the pocket» is tightly pressed to the initial straps of the assembled part by means of jacks. Then the installation runs over the assembled billet and the consumable nozzles are fastened again in the clamps of welding machines, and the fixing cramps are cut off.

The weld on both sides was formed by means of shoes (Figure 3, *a*). The assembly gap at the level of run-out straps is fixed with two cramps — jumpers (see Figure 2, *b*, pos. 3) welded-on to the running out straps using electric arc welding. The cramps-jumpers are positioned between the first, the second, and between the fifth and the sixth groups of nozzles (see Figure 2, *b*). The electroslag process started with the «liquid start». During welding the monitoring of basic parameters of welding mode was carried out [7, 8] (Figure 4). In addition, in the course of welding the required depth of the slag pool on both sides of the weld was regularly controlled and maintained, and also the heating of the back side of welded edges was monitored. It should be noted that the heating temperature of the back side of edges from the moment when the weld came beyond the input pocket (in the gaps between the stiffeners) was 550–650 °C, and it increased to 900–1100 °C only when the slag pool approached the distance of 250–300 mm before the output pocket (see Figure 3, *b*).

The slight increase in the gap between the edges above the mirror of the slag pool was fixed at the level of 1200 mm of the weld, i.e. 42–43 mm. The increase in the gap became more pronounced after welding of half of the weld (the detachment of both cramps-jumpers occurred (see Figure 2, *b*, pos. 3), the gap on the

running out straps amounted to 50 mm. During approach of the slag pool to the level of 2500 mm from the beginning, the opening of the gap near the shoes reached the value of 55 mm and did not change any more. The short circuits between the nozzles and the edges during welding were not recorded. The whole welding process was carried out without violation of the preset parameters of the mode and the methods of weld production. Then the welded billet of the middle beam was subjected to normalizing with tempering and after ultrasonic testing it was sent to the further mechanical treatment.

Thus, for the first time in the world practice of welding ESW CN production the weld of super-large cross section of $11.96 \cdot 10^3 \text{ mm}^2$ ($S = 3820 \text{ mm}$ at $\delta = 120 \text{ mm}$) was produced.

The experience of producing welds of super-large cross sections produced using electroslag welding with consumable nozzle for joining the flexible plates should be used in the development of scientifically grounded methods for calculation of the expected deformations and technical procedures of their control.

In the recent years the enterprise manufactured and delivered six hydraulic forging presses with capacity of 60–100 MN to South Korea, China, Japan and India. The basic load-carrying elements of those presses were produced with applying the ESW CN technologies described above.

1. (1980) *Electroslag welding and surfacing*. Ed. by B.E. Paton. Moscow: Mashinostroenie.
2. Sushchuk-Slyusarenko, I.I. (1969) *Method of obtaining of accurate sizes in electroslag welding*. Kiev: UkrNIINTI.
3. Vinokurov, V.A. (1968) *Welding strains and stresses*. Moscow: Mashinostroenie.
4. Makhnenko, V.I. (1976) *Computational methods for investigation of kinetics of welding stresses and strains*. Kiev: Naukova Dumka.
5. Sushchuk-Slyusarenko, I.I., Lychko, I.I. (1974) *Procedure of performance of electroslag welding*. Kiev: Naukova Dumka.
6. Nevidomsky, V.A., Krasilnikov, S.G., Panin, A.D. et al. (2002) New machine for electroslag welding of large parts at JSC «NKMBF». *The Paton Welding J.*, **2**, 49–51.
7. Voloshin, A.I., Shapovalov, K.P., Belinsky, V.A. et al. (2012) Method for manufacture of large-sized forged-cast billets using electroslag welding. *Ibid.*, **5**, 43–45.
8. Litvinenko, S.N., Shapovalov, K.P., Kosinov, S.N. et al. (2013) Systems of process control and monitoring of conditions — the important factors of quality assurance in electroslag welding of thick metal. *Ibid.*, **12**, 39–41.

Received 03.03.2016

IMPROVEMENT OF WELDING POWER SOURCES IN ORDER TO INCREASE BURNING STABILITY OF ALTERNATING CURRENT ARC

N.M. MAKHLIN

SE Research Engineering Center of Welding and Control in Power Engineering
of E.O. Paton Electric Welding Institute, NASU
11 Kazimir Malevich Str., 03680, Kiev, Ukraine. E-mail:electro@paton.kiev.ua

The work studies the problems of increase of stability of alternating current arc in arc and plasma welding by means of improvement of welding power sources. It is noted that pulse increase of power source output voltage at arc polarity change, application of inductive-capacitive converters, using the power sources providing close to rectangular current waveform acquired the widest distribution among the well-known methods. It is shown that development of alternating current welding power sources, combining two or several methods and having in its design the circuits or devices providing the possibility to function in a mode of initial arc ignition (striking) as well as in a mode of its burning stabilizing, is the most efficient method. It can be achieved, in particular, by means of building of these circuits or devices in form of generators of high or increased voltage pulses with two independent forming circuits. Several variants of circuit solutions of the improved power sources for alternating current arc welding are given and described. 37 Ref., 7 Figures.

Keywords: arc and plasma welding, alternating current, power sources, initial and repeated arc ignition, phase regulation, arc stability, electromagnetic compatibility, inductive-capacitive converters

AC arc and plasma welding in comparison with DC welding has a series of such technological advantages as absence of magnetic blow, possibility of weld formation with favorable geometry parameters and penetration profile as well as producing of more fine-grain structure of weld metal and HAZ, including using more efficient modes than in DC welding. AC welding is significantly cost-effective than DC welding. The AC welding power sources differ by simple design and structure and, in the most cases, their efficiency and safety indices are higher than in DC power sources and expenses for their operation and servicing are perceptibly lower [1–6]. In this connection AC is widely used in many branches of industry for manual metal arc welding (MMAW), submerged arc welding (SAW), manual and mechanized consumable electrode inert gas welding (TIG-AC) and other methods of arc and plasma welding.

AC welding in parallel with known advantages has some disadvantages, main of which lies in low stability of arcing process, which is particularly typical for sine wave welding currents of industrial frequencies. It can be related with its periodic extinctions due to deionizing of interelectrode gap, appearing at each change of arc current polarity, i.e. close to its zero values. Therefore, researchers and specialists of welding engineering in course of number of years and up to now try to find the methods and means to increase the

stability of AC arcs [1, 2, 4, 5, 7–26] among which problem of improvement of welding power sources takes an important place.

Aim of the present work is to study and describe the separate developments, mainly of PWI, directed on increase of stability of AC arc by means of improvement of design and operating algorithms of power part of the welding power sources.

Peculiarities and examples of design of improved alternating current welding power sources. The issues of increase of arc stability in welding current polarity change by means of improvement of welding power sources are reflected in multiple monographs, papers and patents. Significantly substantial theoretical investigations were carried out in this direction, extensive experimental works were performed, different methods for improvement of power sources and engineering solutions, providing realizing of these methods [1–5, 7–21] were developed and tested.

Carried investigations determined that one of the mandatory conditions for providing arc re-ignition at its current polarity change is fulfillment of $U_2 > U_{str}$ requirement, where U_2 is the voltage, applied in a gap between electrode and part being welded during time intervals corresponding to arc current zero; U_{str} is the value of amplitude of arc striking voltage in each semi-period of welding current, called striking peak [1, 2, 4, 5, 15]. It should be noted that fulfillment of this condition by means of increase of open-circuit

voltage U_{op-c} of power source is complicated due to safety requirements, according to which U_{op-c} effective value of power sources should not exceed 80 V, and that of amplitude value 113 V. It is also determined that duration of dead time at current polarity change is determined by content of gas in the interelectrode gap and potential of its ionization as well as rate of arc current change dI_A/dt , which should be more than 10 kA/s in order to provide stable arcing. The more dI_A/dt is, the shorter duration of dead time, the more the de-ionizing time and lower U_{str} value [1, 4, 5, 8] are. dI_A/dt value with sufficient for practice value can be determined as

$$dI_A/dt \approx \Delta I_A/dt = I_{A0}\omega,$$

where I_{A0} is the amplitude value of arc current; ω is its angular frequency.

The following methods have got the most widespread distribution among the known methods of increase of stability of AC arc:

- pulse increase of output voltage of power source at arc polarity change, including with the help of application of special pulse voltage booster — stabilizers of arcing;
- application of inductive-capacitive converters (ICC);
- application of power sources providing arc current waveform close to rectangular one;
- combination of several indicated methods.

Pulse increase of output voltage of power source at polarity change is used, in particular, for improvement of power sources, based on single-phase welding transformer with mechanical or electrical regulation and designed for application mainly of 50 (60) Hz commercial frequency at MMAW. Regardless the fact that production and use of such power sources is gradually decreasing, a stock of welding transformers being in operation is sufficiently large and only in CIS countries makes hundred thousand of pieces. Therefore, the problem of expansion of their technological capabilities is still relevant [27].

All existing engineering solutions for realizing the method of pulse increase of output voltage of welding transformers assumes application of additional blocks and circuits, providing formation of pulses of voltage which is summed at change of polarity of arc current with voltage of welding transformer secondary winding. At that, these additional blocks or circuits necessarily include auxiliary transformer of limited capacity or additional winding on welding transformer core [1, 2, 4, 5, 9, 15]. Arc re-ignition at arc current polarity change are provided as a result of pulse increase of output voltage U_2 of power source to $U_2 > U_{str}$ value. The disadvantages of known devices, which realize the method of pulse increase of output voltage of

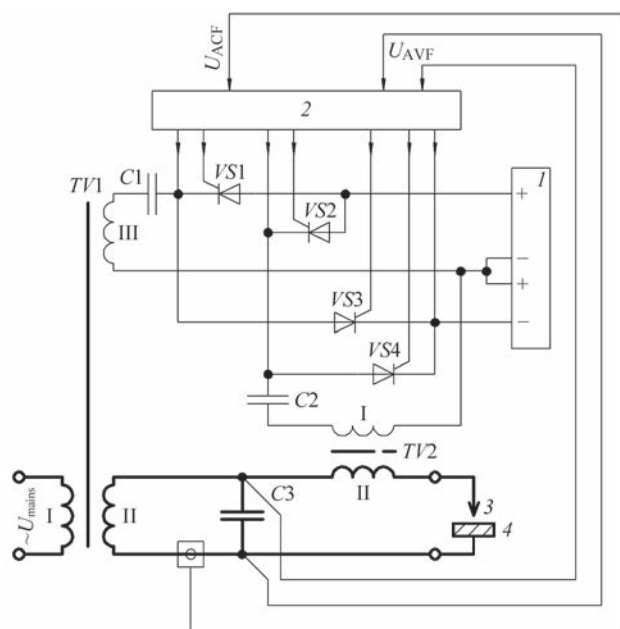


Figure 1. Structure-functional scheme of improved AC power source based on welding transformer with amplitude mechanical or electromechanical regulation (see designations in the text)

power source, are the necessity of somewhat complication and rise of design price of such power sources, absence of possibility of contact-free initial striking of arc, dependence of values of power source output voltage on fluctuations of supply mains voltage.

Figure 1 shows a structural-functional scheme of one of the variants of design of improved power source with pulse increase of output voltage [28].

The power source for AC welding includes regulated (mainly mechanically or electromechanically) single-phase welding transformer $TV1$ with power primary I and secondary II windings and additional winding III as well as striker-stabilizer.

It consists of bi-polar DC source I , control block (CB) 2, circuit of pulse stabilizing, including capacitor $C1$, winding III of welding transformer $TV1$ and key on thyristors $VS1$ and $VS3$ as well as circuit for high-voltage pulse generation, formed by capacitor $C2$, primary winding I of step-up pulse transformer $TV2$, primary winding II of which has series connection to welding circuit, and key on thyristors $VS2$ and $VS4$. Capacitor $C3$ is designed for protection of welding transformer $TV1$ from effect of high-voltage pulses.

Initial ignition of the arc in positive or negative supply voltage half-wave of welding transformer $TV1$ by the signals from CB 2, at the moments when open-circuit voltage $U_{op-c tr}$ of transformer $TV1$ is close to reach the amplitude value, promotes for switch of thyristor $VS2$ or $VS4$, respectively. This causes oscillatory charge or recharge of capacitor $C2$ via winding I of step-up transformer $TV2$. Thyristors $VS2$ or $VS4$ automatically switch off at the end of capacitor $C2$ charge or recharge. Charge or recharge of capacitor $C2$ on

winding II of transformer *TV2* forms the high-voltage pulse, being injected through protective capacitor *C3* in a gap between electrode 3 and part being welded 4. This provides for impact ionizing of this interelectrode gap, its breakdown and appearance in it of a spark discharge coming into arc one, at which arc current from winding II of welding transformer *TV1* starts flowing through the interelectrode gap. Feed of CB 2 signals about switch on of thyristor *VS2* or *VS4* is terminated after appearance in the interelectrode gap of the stable arc discharge on arc current feedback signal (U_{ACF}). Simultaneously, CB 1 starts to generate signals of thyristor *VS1* or *VS3* switch on at the moments determined by arc voltage feedback signals (U_{AVF}) and close to the moments of arc voltage polarity change. Switch on of thyristor *VS1* or *VS3* provokes charge or recharge of capacitor *C1* via winding III of welding transformer *TV1*. Because of this, the increased-voltage pulse, which is injected in the interelectrode gap and stabilizes arcing, is formed on its winding II. Thyristor *VS1* or *VS3* is automatically switched off after charging or recharging of capacitor *C1*.

Among the advantages of this device are efficiency and relative simplicity of circuit and design, amplitude regulation of welding current and stability of coefficient of its form in the whole range of regulation, possibility of application of welding transformer with reduced open-circuit voltage. The disadvantages of this device are impossibility of programming (setting) the welding cycle parameters and performance of modulated current welding modes, loss of some part of power of stabilizing pulses due to shunting effect of protective capacitor *C3*, necessity in special welding transformer *TV1* and specific complication of CB 2, caused by the requirement of separate regulation of thyristors *VS1*–*VS4*, impossibility to design the striker-stabilizer as a self-contained unit. Nevertheless, described device has found application in versatile units for MMAW and TIG-AC welding, for example, single-phase welding apparatuses I-025 U3.1 and oth-

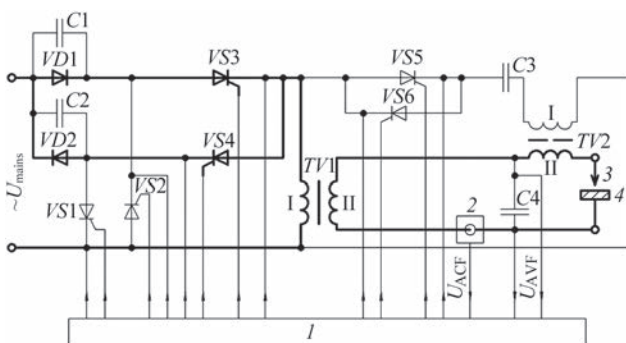


Figure 2. Simplified schematic circuit diagram of power part of improved power source based on TT with phase regulator in the primary circuit: 1 — CB; 2 — arc current probe (for rest designations see the text)

er power sources for AC arc welding, designed based on welding transformers with mechanical or electromechanical regulation of welding current.

The power sources, designed using welding transformers with electric regulation, have better weight-dimension indices and wider engineering capabilities in comparison with the AC power sources, designed based on welding transformers with mechanical or electromechanical regulation of arc current. These are so-called thyristor transformers (TT), action of which is based on the method of phase regulation of arc current [2, 4, 5, 29]. TT phase regulator consists, as a rule, of two back-to-back connected thyristors and system of their regulation. All known TT can be classified on two main characteristics, i.e. way of providing arc current stability and place of phase regulator location, namely in the primary or secondary circuit of the transformer. In turn, according to the first of these characteristics the TT are divided on two groups. The first includes the transformers with intermittent arc current, i.e. with presence of dead time in each semi-period of this current; the second contains the TT providing continuity of current flow through the interelectrode gap during the whole process of welding (except for short intervals of time at change of arc current polarity).

Figure 2 shows the simplified electrical schematic diagram of power part of improved power source. The scheme is designed according to [30] based on TT containing in its primary circuit a phase regulator on *VD1*, *VD2* diodes and *VS3*, *VS4* thyristors, components of voltage booster assembly (capacitors *C1*, *C2* and thyristors *VS1*, *VS2*) and a circuit, having series connection to primary winding I of welding transformer *TV1* with developed magnetic dissipation, for formation of the high-voltage pulses (thyristors *VS5* and *VS6*, capacitor *C3* and primary winding I of pulse transformer *TV2*).

Contact-free initial ignition of arc is carried out with the help of high-voltage pulses, injected into the interelectrode gap (gap between electrode 3 and part being welded 4) via protective capacitor *C4*. After initiation of the spark discharge in the interelectrode gap and its transfer in a stable arc discharge, thyristors *VS5* and *VS6* are switched on and generation of the high-voltage pulses is stopped and welding process is supported due to AC current pulses, passing at supply mains frequency. At that, secondary arc strikes are provided by the fact that voltage, being equal sum of instantaneous value of supply mains and value of voltage set on preliminary charged capacitors *C1* or *C2* via thyristors *VS2* or *VS1*, respectively, is applied to primary winding I of welding transformer *TV1* at the moments of switch of thyristors *VS3* and *VS4*. This

causes pulse increase of voltage in the interelectrode gap to the value exceeding striking peak U_{str} , at the moments of start of each arc current pulse. Regulation of current flowing through the interelectrode gap is carried out by means of change of thyristors VS3 and VS4 switching angle.

The following advantages can be referred to the power sources, designed in accordance with scheme given in Figure 2, namely their capability to provide contact-free initial arc striking as well as its re-ignition during welding, possibility of reduction of weight-dimension characteristics of power sources due to relatively small size of phase generator set into the primary circuit and using welding transformers with fixed positioning of their primary and secondary winding and reduced to 45–48 V open-circuit voltage. At the same time, except for disadvantages including typically low indices of electromagnetic compatibility (EMC), which are fundamental characteristic to all TT with intermittent arc current and phase regulator in the primary winding [2, 4, 5]. The described power source is characterized by pronounced dependence of coefficient of welding current waveform on its relative pulse duration in each semi-period and relatively narrow range of this current regulation. Necessity of application of somewhat increased number of thyristors for designing of such a power source results in complication of its regulation system. Based on this, similar power sources are good to be used in SAW, manual welding using large diameter coated electrodes (from 5 mm) and can have limited application in TIG-AC welding at current more than 350 A.

Investigations and experience of application of the devices with arc current phase regulation show that the wider engineering capabilities and higher EMC indices are typical for TT, in which phase regulator is located in the secondary circuit of the welding transformer, and continuity of current flow via the interelectrode gap is achieved with the help of special circuit, being called an infeed circuit and providing filling of dead times in the idle interval of the phase regulator thyristors.

Figure 3 gives insignificantly simplified electrical schematic circuit of power part of the improved power source of this type. The main components of this power source are non-regulated welding transformer TV1, phase regulator based on thyristors VS1 and VS2, CB 1, welding current probe 2 and supplied by mains voltage striker-stabilizer, containing storage capacitor C1 and C2, pulse transformer TV2 with two separate primary windings I and II and output secondary winding III as well as keys with two-side conductance on thyristors VS3–VS6. Welding transformer TV1 is made with one primary winding I and two series and

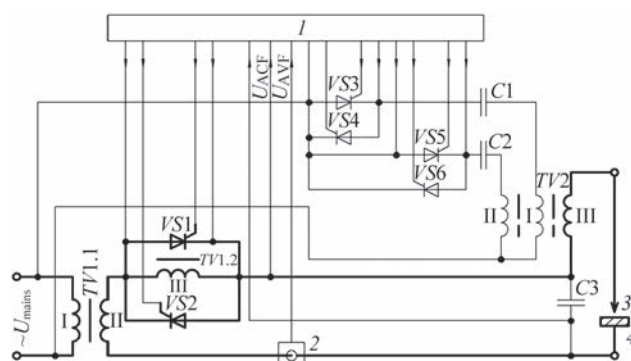


Figure 3. Simplified schematic circuit diagram of power part of improved power source based on TT with phase regulator in the secondary circuit and infeed circuit (designations see in the text)

additive secondary windings II and III. At that, winding II has normal magnetic dissipation, and winding III is of increased one. Welding current regulation and keeping stable its set value under effect of external disturbances and formation of external volt-ampere characteristics (VAC) of the power source are carried out with the help of phase regulator on thyristors VS1, VS2 and U_{ACF} , U_{AVF} . Feed circuit (current of which makes from 10 to 15 A) is formed by secondary windings of welding transformer TV1. Moreover, winding III has parallel connection to phase regulator on thyristors VS1, VS2 due to what VAC of the power source have a form shown in Figure 4.

The peculiarities of design of the infeed circuit lies in the fact that voltage applied to the interelectrode gap at current zero reaches the $U_{op-c tr}$ value being equal the sum of open-circuit voltages at windings II and III of welding transformer TV1 (see Figure 3).

Formation at initial arc ignition of the high-voltage pulses in a generator of voltage pulses of the striker-stabilizer is provided with the help of circuit containing key on thyristors VS3, VS4, storage capacitor C1 and winding I of pulse transformer TV2. In order to form the increased voltage pulses in a mode of arc

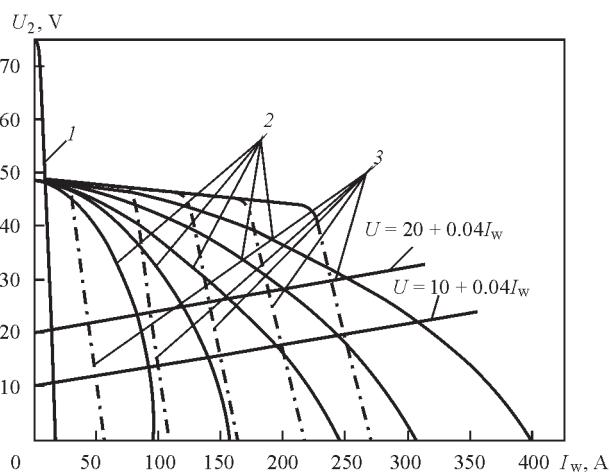


Figure 4. Examples of VAC of improved power source based on TT with phase regulator in the secondary winding and infeed circuit: 1 — infeed circuit; 2 — in MMAW; 3 — in TIG-AC welding mode

stabilizing a circuit is used consisting of key on thyristors $VS5$, $VS6$, storage capacitor $C2$ and winding II of pulse transformer $TV2$. From secondary winding III its the high-voltage pulses and increased voltage pulses are injected into the gap between welding electrode 3 and part being welded 4 via protective capacitor $C3$. Switch of the striker-stabilizer from the mode of initial arc ignition to the mode of arcing stabilizing, and vice versa, is carried out automatically with the help of CB 1 thanks to using coming in it U_{ACF} and U_{AVF} signals applying the same algorithm as for striker-stabilizer of power source (see Figure 1).

In comparison with TT, designed according to scheme given in Figure 2, the advantages of power sources, scheme of which corresponds to Figure 3, is possibility to provide significantly wider range of welding current regulation (the lowest value of which can equal the infeed current), lower values of coefficient of current waveform and less effect of this coefficient on welding process stability and other welding properties of power source, possibility of application with TIG-AC welding (including part from aluminum and its alloys) starting from a range of «small» welding currents.

The main disadvantage of the power sources, scheme of which is given in Figure 3, is caused by low rate of variation of infeed current at its polarity change, not exceeding 4 kA/s. This results in reduction of time of deionization of the interelectrode gap, and, respectively, in necessity to build-up energy and amplitudes of increased voltage pulses, generated by the striker-stabilizer, and experimental determination of the moments of start of these pulses generation.

Another disadvantage lies in limitation of welding current regulation depth, increase of which is inevitably related with rise of its form coefficient. The latter has negative effect on durability of coating of stick and wear resistance of non-consumable electrodes [2]. However, regardless the indicated disadvantages, described device has found application in versatile units for MMAW and TIG-AC welding, for example, single-phase welding units I-190 U3.1 and other power sources for AC arc welding, designed based on TT with infeed circuit and pulse stabilization of arcing process.

In addition to power sources, schemes of power blocks of which are given in Figures 1–3, there are AC power sources, containing regulated welding transformer and device for pulse stabilization of arcing (DPSA), which are used in welding engineering for MMAW, SAW and (in limited amount) TIG-AC welding. A series of works is dedicated to the peculiarities, circuit-design solutions, methods of calculation, technological properties and characteristics of industrial specimens of such power sources and DPSA. Works [4, 5] outline these issues in more de-

tails.. The general disadvantage of all such power sources with DPSA lies in the fact that their design fundamentally eliminates possibility of contact-free initial arc ignition. Besides, such power sources are designed for application of sine-wave mains voltage of only commercial frequency 50 (60) Hz, due to the fact that rate of variation of welding current close to its zero values remains relatively low, that has negative effect on conditions affecting reliability of arc re-ignition.

Analysis of current tendencies of welding equipment development shows that one of the perspective directions of improvement of AC power sources for MMAW, SAW and TIG-AC welding is application of ICC [14, 27] as power modules of these power sources. The ICC with series connection of inductance and capacity gained the widest application in welding power sources. Effect of increase of welding arc stability when using such power sources is caused by the fact that voltage U_c on ICC capacity at welding current zero achieves the largest value, which is Q times (Q is the welding circuit Q -factor) exceeds EMF value of power secondary winding of welding transformer (being equal arc voltage U_a). Due to this the sum voltage U_c and U_a and rate of arc current variation dI_A/dt in the vicinity of current zero point significantly rises [31]. One of the important peculiarities of power sources with ICC is absence in welding current of direct component, that has positive effect on working mode of welding transformer and its weight-dimension indices as well as stability of process of TIG-AC welding of aluminum and its alloys.

Another peculiarity of such power sources lies in the fact that the power sources with ICC among all known welding power sources have the best EMF indices. Theoretical and experimental researches on investigation and determination of welding-technological properties of power sources with ICC, analysis of electromagnetic processes in such power sources and procedure of their design, different aspects of selection and application of element base (in particular, capacitors) in ICC are described in number of works, for example [31–35]. However, fundamental work [14] gives the most complete and detailed consideration of these issues as well as series of original engineering solutions.

Figure 5 shows the structure-functional scheme of improved alternating current power source designed based on ICC (Makhlin, N.M., Korotynsky, O.E., Skopyuk, M.I. *Power source for alternating current arc welding*. Appl. 10697 a2015 UA. Pat. 03.11.2015). This power source consists of non-regulated welding transformer $TV1$ with primary winding I and secondary winding II with normal magnetic dissipation and winding III with developed magnetic

phase regulator thyristors as well as much more higher rate of infeed current variation at change of its polarity. This provides for significantly higher arc stability for welding current regulation extended in area of low current range, and, respectively, wider process capabilities. External VACs of the improved power source with ICC are qualitatively close to shown in Figure 4. Tests of pilot specimens of power source, structure of which corresponds to one given in Figure 5, showed that such power source is capable to provide stability of AC arc and stability of its arcing in welding using stick electrodes virtually with any type of the coating and in SAW using consumable electrode, significantly increase the quality of TIG-welded joints due to increase of resistance of non-consumable electrode and reduction of possibility of defect formation caused by its erosion, obtain satisfactory results in TIG-AC welding of aluminum and its alloys.

At the same time, it is determined that in a series of important cases the rate of infeed current variation at change of its polarity, which is reached in the improved power source with ICC designed for application of mains voltage of industrial frequency, is not enough for realizing high level of stability of TIG-AC welding of aluminum and its alloys. However, this disadvantage can be eliminated by means of 8–10 times increase of frequency of voltage power supply or increase of lev-

el of energy of stabilizing pulses of increased voltage. Another significant drawback of the improved power source with ICC is caused by the problems typical for ICC of large capacity and related with safety of their capacity reactors. However, effect of these problems can be kept at acceptable level using the methods, means and recommendations, given in work [14].

In whole, carried extensive theoretical and experimental investigations, experience of practical application of different models of sources with ICC, success in current capacitor design, in particular development and mastering of commercial production (based on nanotechnology application) of condensers of super large capacity as well as progress of the recent years in development of new ferromagnetic materials with high saturation induction give ground for assuming that in future welding power sources built based on ICC will seriously compete with inverter type welding power sources and in some cases will push put the latter out.

Together with fulfillment of $U_2 > U_{str}$ requirement, another revolutionary measure of increase of AC arc stability, particularly in TIG-AC welding of aluminum and its alloys, is increase of dI_A/dt to 500–800 kA/s and more close to the arc current zero point by means of providing rectangular or close to it waveform of this current. In a course of series of decades such a waveform was achieved by means of application of power converters with normal magnetic dissipation in a set with saturation chokes, operating in a mode of forced magnetization (for example, versatile power source TIR-300D) or the same converters, containing bridge phase regulator in their secondary winding, diagonal of direct current of which includes a power choke of large capacity (for example, pulse versatile power source ISVU-315-1 [2, 36]).

Commercial production of such sources was stopped in the 1970–1980s due to high consumption of materials and low power indices, however some amount of them is still in operation. Currently TIG-AC welding sufficiently widely applies versatile power sources of inverter type, in which virtually rectangular waveform of welding current of 100–400 Hz frequency can be achieved with the help of output power transistor bridge (Figure 6, a) or using double-pole high-frequency rectifiers and two transistor keys with different type of conductivity (Figure 6, b).

Typical for such power sources dI_A/dt values in combination with pulse increase of voltage at the interelectrode gap at arc current polarity change provide for high stability of AC arc burning (including at TIG-AC welding of aluminum and its alloys) in all technologically grounded ranges of arc length and welding current regulation. However, this can provoke some reduction of wear resistance of non-consumable elec-

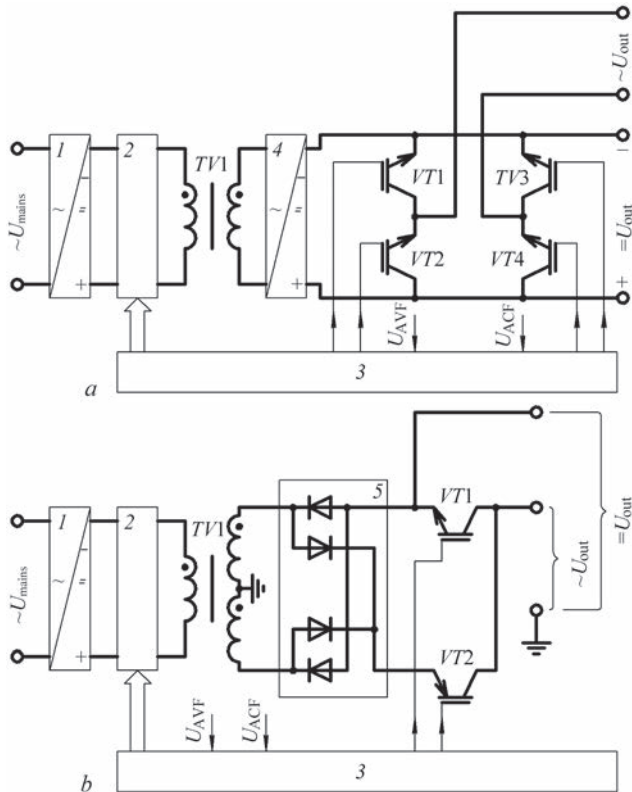


Figure 6. Simplified structure-functional scheme of inverter type power sources with virtually rectangular waveform of alternating welding current (description see in the text): 1 — input (mains) rectifier; 2 — HF converter; 3 — CB; 4 — output HF rectifier; 5 — double-pole output rectifier (with average point)

trode that, apparently, is explained by impact electro-dynamics loads, which at rectangular waveform of welding current effect the non-consumable electrode at each arc current polarity change. Besides, construction of given in Figure 6 power sources for formation of arc alternating current requires mandatory application of auxiliary power transistor keys, each of which should allow passing of current making not less than 60 % of value of the largest arc current, that complicates power part of the source, increase its cost and reduce efficiency. At the same time, it is known fact that if arc alternating current achieves 5–6 A value at MMAW or 3–5 A at TIG welding, then arc discharge in the interelectrode gap can be considered set [1, 4, 5].

It follows from mentioned above that an alternative for the inverter power sources with high rate of arc current variation at its polarity change can be the power sources, in which at arc current zero the high values of dI_A/dt are provided only in $\pm(4-6)$ A range. An example of such an alternating power source can be AC power source (for example TT) with infeed circuit, forming rectangular waveform alternating current. Structural-functional scheme of such a power source, built according to [37], is shown in Figure 7, *a*. This power source includes welding transformer I , welding current phase regulator on power regulated semi-conductor keys (for example, back-to-back connected thyristors $VS1$ and $VS2$), protective capacitor $C1$, power transistor keys 2 and 3, auxiliary unregulated DC power sources 4 and 5 of relative small power (up to 0.45 kW each) and with steep VAC, CB 6, welding current probe 7, asynchronous striker-stabilizer 8 with output pulse transformer, secondary winding of which is in series with welding circuit.

At the initial stage of welding the algorithms of operation and processes in the power source are similar to the algorithms and processes, taking place in the power sources, schemes of which are shown in Figures 3 and 5. From the moment of setting the arc discharge in the interelectrode gap between welding electrode 9 and part being welded 10, the corresponding control inputs of welding current phase regulator, transistor key 2 (in positive voltage half-wave) or 3 (in negative voltage half-wave) and striker-stabilizer 8 start receiving pulse signals from CB 6, which gets the welding current feedback signals from welding current probe 7 and arc voltage feedback signals from protective capacitor $C1$. At that, striker-stabilizer 8 automatically switches from the mode of high-voltage pulse generation for initial arc ignition into the mode of generation of stabilizing increased voltage pulses. Switch on of phase regulator thyristors promotes passing through the interelectrode gap of welding current, representing itself current alternating pulses, amplitude and duration of which is determined by thyristor switch angle (phase).

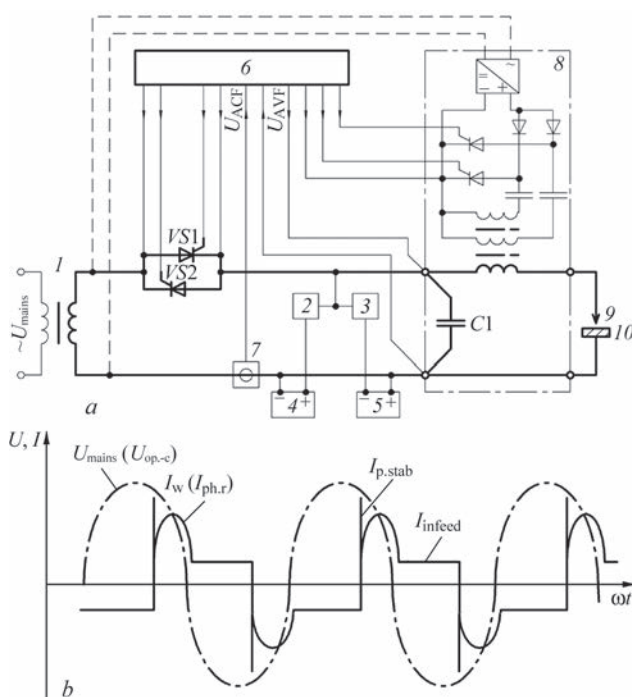


Figure 7. Improved power source with phase regulator and infeed circuit with current of virtually rectangular waveform: *a* — simplified structure-functional scheme; *b* — diagrams of welding current

The dead time between these pulses is filled with infeed current, being supplied depending on its polarity with the help of DC source 4 and key 2 or DC source 5 and key 3. Quick switching of thyristor keys 2 and 3 takes place only at change of welding current polarity and entering in the interelectrode gap of increased voltage stabilizing pulses is realized virtually simultaneous with these switches. Thus, change of infeed current polarity allows achieving its almost rectangular waveform and, respectively, high rate of its change, that in combination with pulse increase of voltage in the interelectrode gap provides for reliable re-ignitions of arc (including at TIG-AC welding of aluminum and its alloys).

Figure 7, *b* shows typical for this case diagrams of welding current. Regardless some complication of the power part of described power source with rectangular waveform of infeed current, in comparison with other known traditional AC power sources, among its advantages are possibility of reliable functioning at U_{mains} frequency voltage being equal 50–500 Hz as well as possibility of application with significant complications of the same approach to infeed circuit architecture in designing TT with phase regulator in the primary circuit or power sources based on ICC. The main structural-schematic solutions, given in Figure 7, *a*, were used in construction of UDG-301M1UKhL4 unit, apparatus N-155 and other units and AC power sources for arc, plasma and microplasma welding.

Conclusions

1. Expansion of technological capabilities and increase of stability of AC welding arc can be achieved by means of application of improved power sources, equipped with striker-stabilizers (mainly of asynchronous type with double-circuit generator of voltage pulses and series connection to welding circuit), including infeed circuits with rectangular waveform current and providing $dI_A/dt \geq 100$ kA/s at change of arc current polarity.

2. Control systems of the improved power sources should contain in its content arc current and voltage feedback circuits.

3. The most perspective for further improvement of technological and weight-dimension characteristics are TT with rectangular waveform of infeed current, power sources based on ICC and welding power sources of inverter type.

The author expresses thanks to Prof. A.E. Korotynsky and Engs V.Yu. Burayk and D.S. Oliyanenko for help in preparation of this work.

1. Leskov, G.I. (1970) *Electric welding arc*. Moscow: Mashinostroenie.
2. Belinsky, S.M., Garbul, A.F., Gusakovskiy, V.G. et al. (1986) *Equipment for arc welding*: Refer. Book. Ed. by V.V. Smirnov. Leningrad: Energoatomizdat.
3. (1974) *Technology of electric fusion welding of metals and alloys*. Ed. by B.E. Paton. Moscow: Mashinostroenie.
4. Dymenko, V.V. (1985) *Increase of process stability and extension of technological capabilities of consumable electrode alternating current welding*: Syn. of Thesis for Cand. of Techn. Sci. Degree. Kiev: PWI.
5. Paton, B.E., Zaruba, I.I., Dymenko, V.V. et al. (2007) *Welding power sources with pulsed stabilizing of arcing*. Kiev: Ekotekhnologiya.
6. Shmakov, E.I., Makhlin, N.M., Fedotenkov, V.G. et al. (1978) Application of alternating current for welding of low-alloy and alloy steels, aluminium and its alloys. *Montazh. i Spets. Raboty v Stroitelstve*, **4**, 20–22.
7. Paton, B.E., Zavadsky, V.A. (1956) Pulsed arc ignition in gas and manual arc welding. *Avtomatch. Svarka*, **3**, 26–35.
8. Lauzhadis, A.I. (1967) Influence of current frequency on arc stability and process of manual arc welding. *Ibid.*, **9**, 29–32.
9. Pentegov, I.V. (1977) Examination of sinusoidal current arc burning conditions with mathematical model of dynamic arc. *Ibid.*, **3**, 8–11.
10. Troitsky, V.A. (1975) Influence of electric circuit parameters on re-ignition of alternating current arc. *Ibid.*, **11**, 6–10.
11. Lugin, V.P. (1975) Comparative evaluation of arcing stability in stick electrode alternating current welding. *Svarochn. Proizvodstvo*, **1**, 39–40.
12. Pokhodnya, I.K., Gorpenyuk, V.N., Marchenko, A.E. et al. (1979) Procedure of determination of alternating current arc stability. *Avtomatch. Svarka*, **12**, 16–18.
13. Farson, D., Courardy, C., Talkington, J. et al. (1998) Arc initiation in gas metal arc welding. *Welding J.*, **8**, 315–321.
14. Korotynsky, O.E. (2007) *High-efficient power sources for arc welding based on inductive-capacitive converters*: Syn. of Thesis for Dr. of Techn. Sci. Degree. Kiev.
15. Paton, B.E., Lebedev, V.K. (1966) *Electric equipment for arc and slag welding*. Moscow: Mashinostroenie.
16. Pokhodnya, I.K. (1967) *Melting of electrode and interconnection of metals with gases in arc welding*: Syn. of Thesis for Dr. of Techn. Sci. Degree. Kiev.
17. Aldenhoff, B.J. *Alternating current arc power source*. Pat. 3328637A1, USA. Publ. June 1967.
18. Novikov, O.Ya. (1978) *Stability of electric arc*. Leningrad: Energiya.
19. Pentegov, I.V., Dymenko, V.V., Rymar, S.V. (1995) Selection of open-circuit voltage in sources for alternating current manual arc welding. *Avtomatch. Svarka*, **5**, 35–40.
20. Andrianov, A.A., Sidorets, V.N. (2009) Optimization of stabilizing parameters of alternating current arc welding. *Elektrotekh. i Elektromekhanika*, **2**, 5–8.
21. Makhlin, N.M. (2015) Peculiarities of contactless ignition of alternating current arc. *The Paton Welding J.*, **10**, 29–35.
22. Temkin, B.Ya. (1981) *Theory and calculation of welding arc exciters*: Syn. of Thesis for Cand. of Techn. Sci. Degree. Leningrad.
23. Lenivkin, V.A., Klenov, G.G., Sagirov, Kh.N. et al. (1986) Arc ignition in consumable electrode welding. *Avtomatch. Svarka*, **2**, 30–34.
24. Makhlin, N.M., Korotynsky, A.E. (2014) Analysis and procedure of calculation of series connection electronic devices for contactless arc excitation. *The Paton Welding J.*, **1**, 30–40.
25. Makhlin, N.M., Korotynsky, A.E. (2015) Asynchronous exciters and stabilizers of welding arc. Analysis and design procedure. Pt 1. *Ibid.*, **3/4**, 24–35.
26. Makhlin, N.M., Korotynsky, A.E. (2015) Asynchronous exciters and stabilizers of arc. Analysis and calculation procedure. Pt 2. *Ibid.*, **7**, 26–37.
27. Lebedev, V.K. (1995) Tendencies of development of power sources for arc welding. *Avtomatch. Svarka*, **5**, 3–6.
28. Fedotenkov, V.G., Makhlin, N.M., Ivanov, V.Ya. *Device for alternating current welding*. USSR author's cert. 1668068 A1. Int. Cl. B23 K 9/06. Publ. 07.08.1991.
29. Ivanov, G.P., Rozhansky, Z.E., Serdyuk, N.A. (1973) Thyristor current controllers of welding transformers. *Avtomatch. Svarka*, **11**, 65–69.
30. Dudko, D.A., Fedotenkov, V.G., Makhlin, N.M. et al. *Device for alternating current welding*. USSR author's cert. 935225. Int. Cl. B23 K 9/06, B23 K 9/00. Publ. 15.06.1982.
31. Arlauskas, V.Yu., Narushkyavichus, I.R., Dubashinsky, V.N. et al. (1974) Study of elasticity of welding arc supplied from source with induction and capacity. *Svarochn. Proizvodstvo*, **10**, 14–16.
32. Lebedev, V.K., Narushkyavichus, I.R. (1971) Stability of alternating current arcing in circuit with condenser. *Avtomatch. Svarka*, **4**, 3–5.
33. Narushkyavichus, I.R., Narkyavichus, I.M., Vishnyak, I.S. (1981) Study of multioperator welding source with induction and capacity for welding of alloy steels. In: *Abstr. of All-Union Sci.-Techn. Conf. on Development, Study and Implementation of New Power Sources of Welding Arc* (21–22 May 1981), Pt 2, 9–14.
34. Troitsky, V.A. (1981) Method of smooth control of power sources containing longitudinal-capacitive compensation. *Avtomatch. Svarka*, **5**, 8–12.
35. Lebedev, V.K., Korotynsky, A.E. (1994) Alternating current arc in circuit with series induction and capacity. *Ibid.*, **12**, 47–48.
36. Goloshubov, V.I. (2005) *Welding power sources*: Manual. Kiev: Aristej.
37. Fedotenkov, V.G., Makhlin, N.M., Yashunsky, A.Ya. et al. *Device for alternating current arc welding*. USSR author's cert. 1299725 A1. Int. Cl. B23 K 9/00, 9/06. Publ. 30.03.1987.

Received 28.12.2016

CALCULATION OF TWO-LAYER BILLET OF SPHERICAL BOTTOMS FOR HIGH-PRESSURE VESSELS

A.S. PROKOFIEV¹, R.S. GUBATYUK¹, A.F. MUZHICHENKO¹ and V.N. BARANOVSKY²

¹E.O. Paton Electric Welding Institute, NASU

11 Kazimir Malevich Str., 03680, Kiev, Ukraine. E-mail: office@paton.kiev.ua

²Ternopol Ivan Puluji National Technical University, Ministry of Education and Science of Ukraine

56 Russkaya Str., 46001, Ternopol, Ukraine

The article presents the materials of calculations of circumferential stresses and radial displacements in the wall of two-layer spherical bottom. Three models of bottoms were considered, where different combinations of materials for manufacture of shell layers are used. The rational layer thicknesses, circumferential stresses and radial displacements were determined, which formed in them in the ranges of elastic deformations at different combinations of materials of shell layers. The determination of circumferential stresses was carried out by calculation method according to the analytical dependences and by the method of computer simulation. The application of material with higher strength properties in manufacture of the outer shell leads to the effective loading of their common wall, reduction in its thickness and, correspondingly, increase in its inner stresses and, eventually, in the rational loading. 10 Ref., 4 Tables, 3 Figures.

Keywords: welded structure, two-layer shell, spherical bottom, calculation model, stresses, deformations, welded vessels

The application of two-layer and, in perspective, multilayer materials for manufacture of shell welded structure allows obtaining the certain advantages in most cases. These advantages are increase in such indicators as wear resistance, corrosion resistance, increased resistance to cyclic loads as well as the ability to create a high resistance to fatigue fracture. The safe operation of such welded shell structure consists in the achievement of rational distribution of stresses in its walls during application of the operational load. The preliminary stressed structures are also used.

For two-layer cylindrical shell structures the joints with tension are applied that allows reducing the thickness of the common wall and obtaining the rational distribution of stresses, which are formed in the common wall during application of the operation load. Also the application of the material, resistant to cyclic loads in a two-layer shell structure, allows redistributing the basic cyclic load, applied to the entire welded structure, to the layer where the given material is applied and, thus, unloading the layers, which have a reduced resistance to cyclic loading, but have other operational or technological properties (for example, corrosion resistance).

To meet the requirements to corrosion resistance in welded structures of the type of containers, vessels, cylinders, the application of protective coatings on the inner surface or manufacture of a two-layer body is possible, where the material of the inner layer is manufactured of metal having increased corrosion resis-

tance. It is known that two-layer sheet bimetallic materials can be produced using the method of explosion welding [1, 2]. Also, the double-layer sheet bimetallic materials can be produced using the method of induction press braze-welding [3–5].

The two-layer cylindrical bodies can be also produced by coaxial fitting-up of the heated outer shell on the inner one, which provides tightness. In this way the double-layer cylindrical bodies can be also produced by the method of thermal shrinkage of the outer shell to the inner one, carrying out induction heating by a gradual movement of the coaxially assembled inner and outer shells. The given technology has a number of advantages, consisting in the fact that the induction heating is significantly cheaper, it does not influence the surface of heating, as compared to gas heating, and it can be realized in any, including protective atmosphere.

In work [6] three models of cylindrical bodies of the same type were considered, operating under pressure, where the wall of the cylindrical body represents a two-layer shell (Figure 1). The thickness of the inner thin-walled shell (ratio of diameter to the wall thickness is 10 and more) for all three models is constant. In the calculation models the outer shell is fitted to the inner shell with a minimum tightness, close to zero, while its inner diameter matches the outer diameter of the shell, and its outer diameter is calculated basing on the strength properties for the each applied material. For all three models of two-layer cylindrical

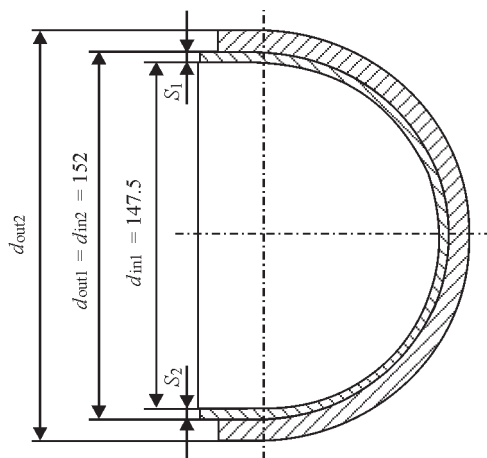


Figure 1. Design of spherical bottom [6]

bodies of vessels, the calculated values of wall thicknesses of the outer shell and the common wall and the stresses formed in the shells and in the common wall, were presented in work [6]. This article presents calculations of models of three similar-type two-layer welded structures of spherical bottoms for welded vessels, operating under pressure, moreover, in all the models the inner thin-walled shell of spherical bottom has the same geometric dimensions, which coincide with abutting dimensions for all three models of the inner thin-walled shell of the cylindrical body.

To determine the stresses, formed in the shell wall, the welded structure of the vessel was considered, operating under pressure, where the cylindrical wall of the body and the spherical bottoms were manufactured of the two-layer material. Three similar-type welded structures of vessels (Table 1) are calculation models, where for the purpose of choosing the optimal parameters the combination of different grades of steels for the inner and outer layer is used. Accordingly, the strength characteristics of the steel grades, used for the each layer of the shell, were laid to the calculation models. The subject of the investigation was the stresses formed in the layers of the two-layer spherical bottom and in the common two-layer wall, as well as the determination of the amount of deformation during application of operating pressure for three models.

The thicknesses of the walls of outer shells of the spherical bottoms S_2 and the cylindrical bodies S_{2b} , and, relatively, the thicknesses of the common walls of the bottom S and the cylindrical bodies S_b in all three models may not coincide. However, it allows producing the circumferential weld, joining the cylindrical body with the

spherical bottom. At the same time, the wall thicknesses and matched diameters of the inner shells for all three models are provided and the presence of some different thicknesses of walls of the outer shells (up to 15–20 % of the common thickness of the outer shell wall) is observed. It allows, as a result, designing and forming three similar-type models of welded structures: of a welded vessel with a double-layered cylindrical body and a two-layer spherical bottom on the basis of the obtained calculation data. Moreover, in each model the materials of the steel grades of the body and bottom layers coincide, and between the models of cylinders there is no matching in the materials of the two-layer shells. The calculations on the choice of geometric parameters of the similar-type two-layer structures of the spherical bottoms for the vessels, operating under pressure, were carried out according to the known methods [7–9]. The combination of different steel grades for the inner and outer shells in three models of spherical bottom was selected in accordance with work [6] for three models of a two-layer cylindrical body of the welded vessel. At the same time, the following conditions were observed:

- calculations were carried out taking into account the same inner operating pressure $P_{op} = 20$ MPa and the same geometrical dimensions of the inner shell wall of the bottom ($d_{in1} = 47.5$ mm; $d_{out1} = 152$ mm; wall thickness of the inner shell of the spherical bottom is constant $S_1 = 2.25$ mm) for all three models of welded vessels;
- inner diameter of the spherical outer shell corresponds to the outer diameter of the wall of the inner spherical shell for all three types of welded vessels and is constant ($d_{out1} = d_{in2} = 152$ mm);
- dimensions of the wall of the spherical outer shell (d_{out} , S_2) were calculated basing on the stresses formed in it (the outer shell) and the strength characteristics of the used steel grade;
- in the structure of spherical bottom from the calculated thicknesses of the common wall of the bottom S its minimum value was taken;
- stresses in the separate shells of the spherical bottom σ_1 , σ_2 , as well as the total stresses in the common wall of the bottom σ were determined without taking the tightness into account;
- calculation was carried out according to the acting standard documents and provisions of work [7], moreover, the operating operational pressure of the model of the welded vessel was calculated (at safety

Table 1. Combination of material and ratio of thicknesses of shell walls of spherical bottom for the models

Model number	Materials of inner S_1 and outer shell S_2 , respectively	$S_1/(S_2 + C)$
1	Steel 08kp + high-strength steel	$2.25/(1.61 + 0.077) = 1.333$
2	Steel 20 + steel 20	$2.25/(4.49 + 0.21) = 0.478$
3	Steel 08kp + steel 08kp	$2.25/(8.42 + 0.4) = 0.255$

Table 2. Results of calculations of three models of structures of spherical bottoms

Parameter	Model 1	Model 2	Model 3
Admissible stresses in the metal of bottom wall, MPa; $[\sigma]_{op} = \sigma_{dang}/n$ ($n = 2.7$)			
Inner shell $[\sigma_1]$	74	114.3	74
Outer shell $[\sigma_2]$	370.4	114.3	74
Thickness of the wall of inner shell S_1 , mm	2.25	2.25	2.25
Inner shell			
Inner diameter d_{in1} , mm	147.5	147.5	147.5
Middle diameter d_{mid1} , mm	149.75	149.75	149.75
Outer diameter d_{out1} , mm	152	152	152
Thickness of the outer shell wall $S_2 + C$, mm	1.687	4.7	8.82
Outer shell			
Inner diameter d_{in2} , mm	152	152	152
Middle diameter d_{mid2} , mm	153.687	156.7	160.82
Outer diameter d_{out2} , mm	155.374	161.4	169.64
Thickness of the common bottom wall $S = S_1 + (S_2 + C)$, mm	3.937	6.95	11.07
Common bottom wall			
Inner diameter d_{in} , mm	147.5	147.5	147.5
Middle diameter d_{mid} , mm	151.437	154.45	158.57
Outer diameter d_{out} , mm	155.374	161.4	169.64
Ratio d_{out}/S	39.465	23.22	15.324
Ratio $(S_2 + C)/S_1$	0.75	2.088	3.92

factor $n = 2.7$) according to the maximum admissible values of the stresses formed in the metal $\sigma_{op} = \sigma_{dang}/n$, where σ_{dang} is the critically dangerous stress. Depending on the grade of steel for plastic materials $\sigma_{dang} = \sigma_y$, for brittle materials $\sigma_{dang} = \sigma_t$;

- in the calculation models the strength of welds was taken as equal to the strength of the base metal (for the given calculation mathematical model taking into account the application of different grades of materials, the strength of welds is provided by increasing the total thickness of the common wall on the value of the wall thickness, which in all cases should be not less than 0.5 mm [7]).

Materials of calculations. On the basis of the carried out calculations (see Table 1) the combination of materials, geometric sizes and ratio of thicknesses S_1 , S_2 of shells of spherical bottom and of wall thickness

C is shown, where C is determined according to formula [7] for three types of models:

$$C = \frac{0.05}{1 + 0.05} S.$$

The results of calculations of three models of structures of spherical bottoms are presented in Table 2.

The values of operating stresses σ_{op1} , σ_{op2} , σ_{op} which are formed in the metal in the inner and outer shell and in the common wall of the spherical bottom from the applied operating pressure P_{op} , are given in Table 3.

The calculation of stresses, formed in the common wall of the bottom, was carried out the same as for a single-layer material of the total thickness for three types of models. Thus, the strength calculation of welded structure was performed, which in this case is the welded two-layer vessel, where a double-layer

Table 3. Comparison of calculation stresses σ_{op1} , σ_{op2} , σ_{op} at $P_{op} = 20$ MPa with admissible stresses σ_1 , σ_2 in the metal of inner and outer shells for three models

Parameter	Model 1	Model 2	Model 3
Admissible stresses σ_1 , σ_2 , MPa	$\sigma_1 = 74$; $\sigma_2 = 370.4$	$\sigma_1 = 114.3$; $\sigma_2 = 114.3$	$\sigma_1 = 74$; $\sigma_2 = 74$
Calculation stresses for inner σ_{op1} , outer σ_{op2} shells and common bottom wall σ_{op} , MPa			
Inner shell (S_1)	$\sigma_{op1} = 4.447 < \sigma_1$	$\sigma_{op1} = 6.869 < \sigma_1$	$\sigma_{op1} = 4.447 < \sigma_1$
Outer shell ($S_2 + C$)	$\sigma_{op2} = 354.2 < \sigma_2$	$\sigma_{op2} = 109.4 < \sigma_2$	$\sigma_{op2} = 70.9 < \sigma_2$
Common bottom wall ($S_1 + (S_2 + C) = S$)	$\sigma_{op} = 192.3 < \sigma_2$	$\sigma_{op} = 111.1 < \sigma_1 = \sigma_2$	$\sigma_{op} = 71.6 < \sigma_1 = \sigma_2$

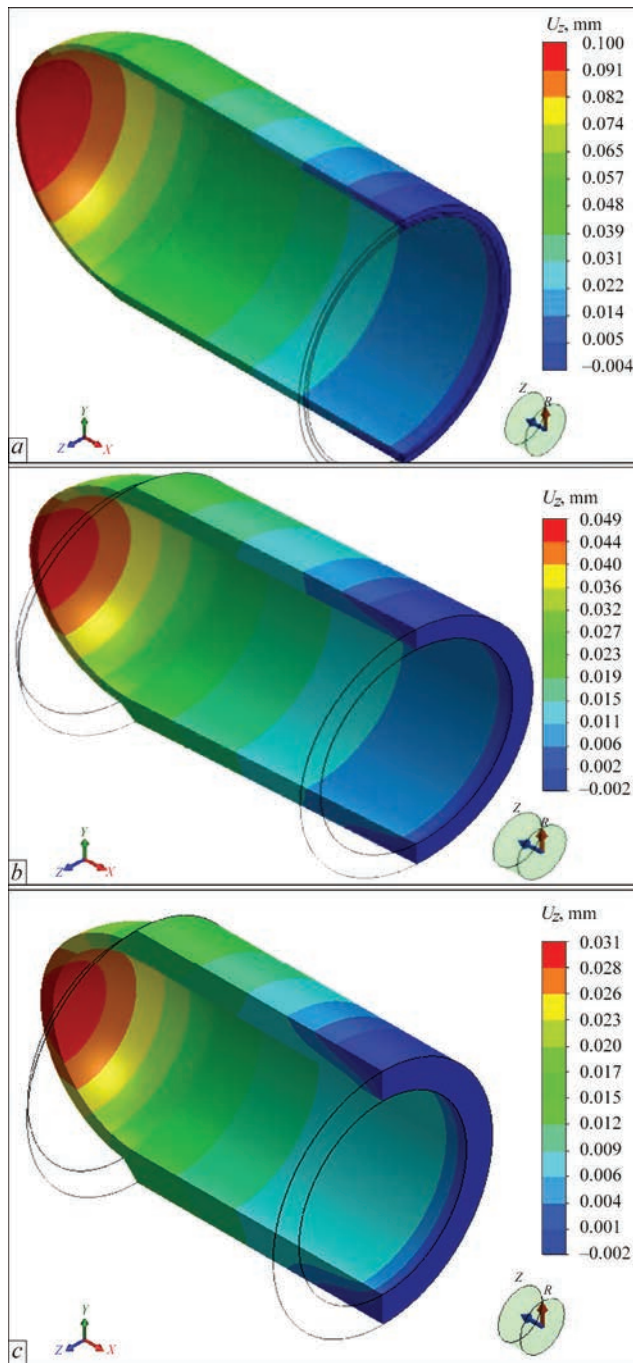


Figure 2. Fields of radial displacements in models 1 (a), 2 (b) and 3 (c) of vessels at their loading by operating pressure

cylindrical body and a spherical bottom are produced also in two-layers [10].

The circumferential stresses and radial displacements obtained as a result of computer simulation are presented in Figures 2 and 3.

The data obtained as a result of computer simulation at the loading by the inner operating pressure of three types of welded structure (welded vessel, in which the cylindrical body and spherical bottom are produced in two-layers) are presented in Table 4. The comparison of values of circumferential stresses (average in thickness), determined as a result of computer simulation, with the stresses, determined according to the analyt-

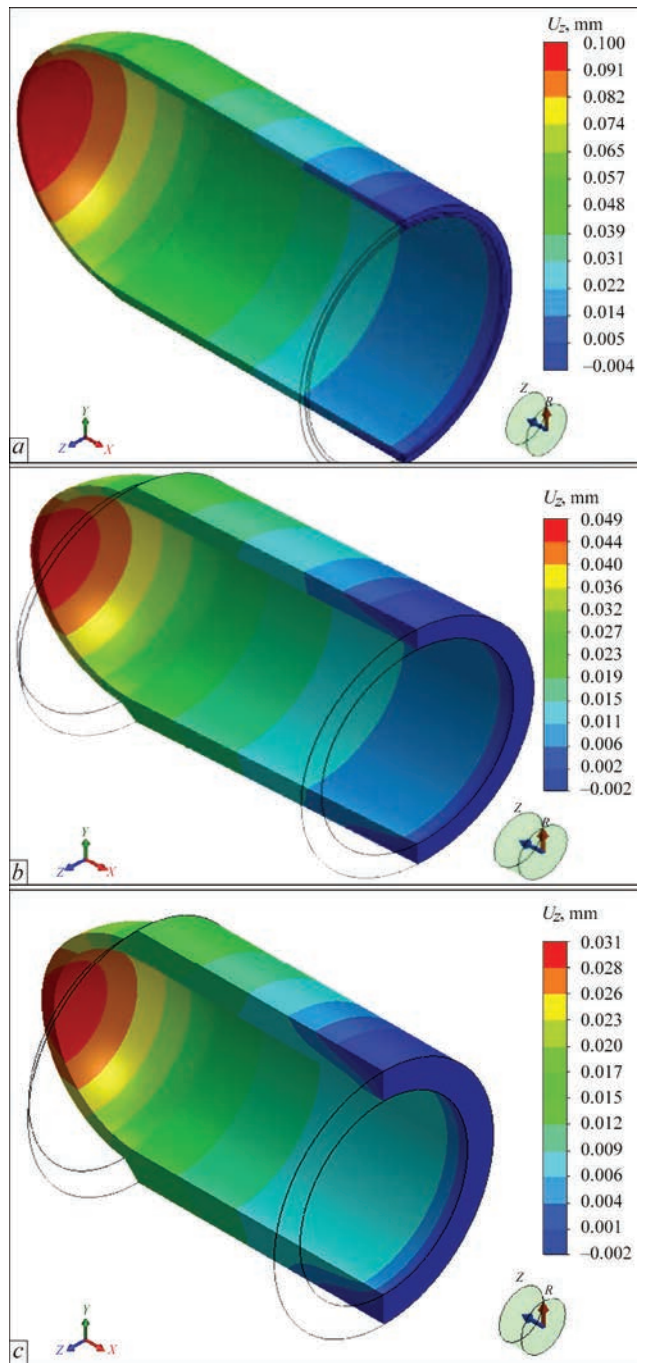


Figure 3. Distribution of circumferential stresses in models 1 (a), 2 (b) and 3 (c) of vessels at their loading by operating pressure

ical dependences using the calculation method (see Table 3) from applying the operating pressure to the common wall for three models almost coincide or have a slight discrepancy (0.54–3.02 %). The value of stresses, determined by the calculation method, appeared to be higher than the values of stresses, determined as a result of computer simulation.

According to the results of computer simulation it was found that the radial displacements in the common wall of the two-layer shell are increased proportionally to the formed circumferential stresses from model 3 to model 1 and are inversely proportional to the thickness of the common wall of the two-layer shell.

Table 4. Displacements and stresses at operating pressure loading for models used

Parameter	Model 1	Model 2	Model 4
Mean value of displacement, mm, $\Delta_m = (\Delta_{\min} + \Delta_{\max})/2$	$\Delta_m = 0.074$	$\Delta_m = 0.0255$	$\Delta_m = 0.016$
Mean value of circumferential stresses in common wall of a double-layer shell, MPa (computer modeling), $\sigma_m = (\sigma_{\min} + \sigma_{\max})/2$	$\sigma_m = 190$	$\sigma_m = 110.5$	$\sigma_m = 69.5$
Mean value of circumferential stresses in common wall of double-layer shell, MPa (determined by calculations, data of Table 3)	$\sigma_{op} = 192.3$	$\sigma_{op} = 111.1$	$\sigma_{op} = 71.6$

The largest radial displacements and highest values of circumferential stresses are in model 1, which has a minimum common thickness of the wall of the two-layer shell. In the thickest common wall of the two-layer shell, in model 3, the values of circumferential stresses are relatively the lowest and the radial displacements in the ranges of strain deformations are the minimum, which corresponds to the Hooke's law. In this case, the optimum thickness of the common wall of the two-layer shell is determined by rational combination of the circumferential stresses and radial displacements in it in the ranges of elastic deformations, basing on the values of strength of the least strength shell material and the strength of the interlayer welded joint. The values of circumferential stresses in the common wall of the two-layer shell, obtained as a result of computer simulation (at the loading by the inner operating pressure of welded structure in the model) are correlated with the circumferential stresses determined previously by the calculation method for all three models.

The values of circumferential stresses determined according to the results of computer simulation and by the calculation method for all three types of models are determined also in accordance with the requirements to the strength of welded joint of shells. In this work according to the results of computer simulation and by the calculation method for all three types of models, the thickness of spherical bottom was determined. However, in accordance with the rules of calculations and designing [7] the wall thickness of the bottom in the real welded structures should be taken as being not smaller than the calculated thickness of the wall of the cylindrical body. For such welded structures as vessels, operating under pressure at the long-term cyclic loading, the minimum radial displacements in the ranges of elastic deformations represent a certain risk. It is predetermined by the possibility of development of fatigue cracks, causing fatigue fracture, including those in the area of interlayer joint.

During designing in order to determine the optimal parameters of a two-layer structure of the bottom, the

computer simulation of the stress-strain state at applying the inner operating pressure as well as the inner limiting pressure of the structure is considered to be appropriate aimed at determination and comparison of circumferential stresses obtained during simulation with the stresses, determined by the calculation method according to the analytical dependences.

Conclusions

1. The rational geometric parameters of the welded two-layer shell were determined using the computer simulation and by the calculation method according to the analytical dependences. For the common wall of the thin-wall two-layer shell the rational combinations of the non-limiting circumferential stresses and radial displacements were specified.

2. During designing the circumferential stresses in the common wall of the shell should be taken into account, the average value of which was determined as a result of computer simulation with the stresses, determined by the calculation method according to the analytical dependences.

1. Konon, Yu.A., Pervukhin, L.B., Chudnovsky, A.D. (1987) *Explosion welding*. Moscow: Mashinostroenie.
2. Petushkov, V.G. (2005) *Application of explosion in welding technique*. Kiev: Naukova Dumka.
3. Pismenny, A.S., Novikova, D.P., Prokofiev, A.S. et al. (2004) Properties of weld metal at induction braze-welding of steel 20. *The Paton Welding J.*, **12**, 26–32.
4. Pismenny, A.S., Prokofiev, A.S., Pismenny, A.A. et al. (2010) Properties of the welded joints of tubular billets produced by pressure braze-welding with a forming device. *Ibid.*, **7**, 22–25.
5. Bakshi, O.I., Shron, R.Z. (1962) Strength in static tension of welded joints with soft interlayer. *Svarochn. Proizvodstvo*, **5**, 6–10.
6. Pismenny, A.A., Gubatyuk, R.S., Prokofiev, A.S. et al. (2014) Braze-welded tubular billets for pipelines and high-pressure vessels. *The Paton Welding J.*, **10**, 38–44.
7. Chernega, V.I. (1976) *Safe service of vapor boilers, vessels and pipelines*. 2nd ed. Kiev: Tekhnika.
8. Pisarenko, G.S., Yakovlev, A.P., Matveev, V.V. (1998) *Reference book on strength of materials*. 2nd ed. Kiev: Naukova Dumka.
9. Majzel, V.S., Navrotsky, D.I. (1973) *Welded structures*. Leningrad: Mashinostroenie.
10. Pysmenny, O.S., Savytsky, M.M., Pysmenny, O.O. et al. *High-pressure vessel with cylindrical body of shell structure*. Pat. 107847 Ukraine. Publ. 25.02.2015.

Received 22.12.2015

PATON PUBLISHING HOUSE

www.patonpublishinghouse.com

SUBSCRIPTION

The Paton
WELDING JOURNAL

«The Paton Welding Journal» is Published Monthly Since 2000 in English, ISSN 0957-798X.

**АВТОМАТИЧЕСКАЯ
СВАРКА**

«Avtomaticheskaya Svarka» Journal (Automatic Welding) is Published Monthly Since 1948 in Russian, ISSN 005-111X.

«The Paton Welding Journal» is Cover-to-Cover Translation of Avtomaticheskaya Svarka» Journal into English.

If You are interested in making subscription directly via Editorial Board, fill, please, the coupon and send application by Fax or E-mail.

The cost of annual subscription via Editorial Board is \$348 for «The Paton Welding Journal» and \$180 for «Avtomaticheskaya Svarka» Journal.

«The Paton Welding Journal» can be also subscribed worldwide from catalogues subscription agency EBSO.

SUBSCRIPTION COUPON

Address for journal delivery _____

Term of subscription since _____

20

till _____

20

Name, initials _____

Affiliation _____

Position _____

Tel., Fax, E-mail _____

We offer the subscription all issues of the Journal in pdf format, starting from 2009.

The archives for 2009–2014 are free of charge on www.patonpublishinghouse.com site.



ADVERTISEMENT

in «Avtomaticheskaya Svarka» and «The Paton Welding Journal»

External cover, fully-colored:

First page of cover (190×190 mm) — \$700
Second page of cover (200×290 mm) — \$550
Third page of cover (200×290 mm) — \$500
Fourth page of cover (200×290 mm) — \$600

Internal cover, fully-colored:

First/second/third/fourth page of cover (200×290 mm) — \$400

Internal insert:

Fully-colored (200×290 mm) — \$340

Fully-colored (double page A3) (400×290 mm) — \$500

- Article in the form of advertising is 50 % of the cost of advertising area
- When the sum of advertising contracts exceeds \$1001, a flexible system of discounts is envisaged

Size of journal after cutting is 200×290 mm

Editorial Board of Journal «Avtomaticheskaya Svarka» and «The Paton Welding Journal»

E.O. Paton Electric Welding Institute of the NAS of Ukraine

International Association «Welding»

11 Kazimir Malevich Str. (former Bozhenko Str.), 03680, Kiev, Ukraine

Tel.: (38044) 200 60 16, 200 82 77; Fax: (38044) 200 82 77, 200 81 45

E-mail: journal@paton.kiev.ua; www.patonpublishinghouse.com